Universitat Autònoma de Barcelona

ESCOLA D'ENGINYERIA

Electronic Engineering Department


# Resistive Switching Statistics in MIM structures for Non-volatile memory applications

A dissertation submitted by Xiaojuan Lian
In fulfillment of the requirements for the degree of Doctor of Philosophy
in the Electronic Engineering program

Supervised by Prof. Jordi Suñé
Bellaterra, May of 2014

Universitat Autònoma de Barcelona

**ESCOLA D’ENGINYERIA**

**Electronic Engineering Department**

Dr. Jordi Suñé, full professor of the Electronic Engineering department of the Autonomous University of Barcelona,

**Certifies**

That the dissertation ***Resistive Switching Statistics in MIM structures for Non-volatile memory applications (Estadística de commutació resistiva en estructures MIM per a aplicacions en memòries no volàtils)*** submitted by Xiaojuan Lian to the school of Engineering in fulfillment of the requirements for the degree of Doctor of Philosophy in the Electronic Engineering program has been performed under his supervision.

Dr. Jordi Suñé
Bellaterra, May of 2014

# Acknowledgements

How time flies. Three years passed in the blink of an eye and I will finish my Ph. D degree. First of all, I would like to thank my supervisor Prof. Jordi Suñé. Not only does he give me an opportunity to study in Spain, but also helps me a lot with great patience in my work during three years. Without his help, I could not finish my Ph.D degree up to time.

I also give my thanks to Dr. Shibing Long who helped me a lot at the beginning of the Ph. D degree. He made me familiar with my work better and faster. Besides, I would like to thank all members of Electronic Engineering department who let me feel comfortable and happy living in Barcelona. Especially, I send my thanks to all the coauthors of my publications.

Apart of obtaining the help from people, I feel very grateful to China Scholarship Council (CSC). I could finish my Ph. D work with this financial support.

Finally, I would like to thank my family who support me continuing to study for Ph. D degree, especially my husband Fanxuan Zeng.

Thank you very much!

Xiaojuan

# Index

**Publications related to this thesis**

**Presentation ........................................................................................1**

**1. Introduction ........................................................................................3**

1.1 Resistive switching mechanism ........................................................................4
1.2 Applications of Resistive switching devices ........................................................6
    1.2.1 Non-volatile memory ........................................................................6
    1.2.2 Reconfigurable computing architectures ........................................................7
    1.2.3 Neuromorphic circuits ........................................................................7
1.3 The research aim of the thesis ........................................................................8
1.4 Summary ........................................................................................9

**2. The Quantum Point Contact Model for RRAM ..............................11**

2.1 The QPC Model for multiple breakdown paths ..............................................11
2.2 Experimental results of QPC model in the HRS and LRS ..............................14
2.3 Multi-scale QPC model by coupling it to the results of ab-initio simulations 18
    2.3.1 First-principle simulations of $HfO_2$ ..............................................18
    2.3.2 The new multi-scale QPC model coupled to ab-initio results ..............21
2.4 Analysis of experimental results in terms of the multi-scale QPC model ......22
    2.4.1 Experimental results for nonpolar Pt/$HfO_2$/Pt devices ..........................23
    2.4.2 Experimental results for Pt/Ti/$HfO_2$/Pt devices operated under bipolar conditions ........................................................................26
    2.4.3 Experimental results for Pt/Ti/$HfO_2$/Pt devices operated under unipolar conditions ........................................................................28

**3. RESET/SET Switching Statistics of RRAM ....................................31**

3.1 The cell-based percolation model for the dielectric breakdown ......................32
3.2 Cell-based Geometrical Model of CF-based RRAM device ..........................35
3.3 Deterministic model for CF-based RRAM device..........................................36
    3.3.1 Deterministic model for the reset dynamics ........................................36
    3.3.2 Deterministic model for the set dynamics ..........................................38
3.4 Experimental results for reset and set statistics ..............................................39
    3.4.1 Experimental reset statistics..............................................................39
    3.4.2 Experimental set statistics..................................................................43
3.5 Conclusions........................................................................................44

**4. A quantum wire state for RRAM ....................................................45**

4.1 Ramp-voltage sweep reset method in Pt/$HfO_2$/Pt and Pt/Ti/$HfO_2$/Pt structures ........................................................................................................................46
4.2 Three-state resistive switching using the successive-voltage sweep reset method..........................................................................................................49
4.3 Unipolar reset of Pt/$HfO_2$/Pt structures under constant-voltage conditions ...51
4.4 Two-step reset experiments of unipolar switching in Pt/$HfO_2$/Pt structures ..54

**5. Conclusions.........................................................................................57**

**References ..........................................................................................61**

**Papers (A-E)**

# Publications related to this thesis

## Compendium of Publications included in this thesis

1. S. Long, **X. Lian**, C. Cagli, X. Cartoixa, R. Rurali, E. Miranda, D. Jiménez, L. Perniola, M. Liu and J. Suñé. "Quantum-size effects in hafnium-oxide resistive switching", Applied Physics Letters, vol.102, 183505(2013).
2. S. Long, **X. Lian**, T. Ye, C. Cagli, L. Perniola, E. Miranda, M. Liu and J. Suñé, "Cycle-to-Cycle Intrinsic RESET Statistics in $HfO_2$-Based Unipolar RRAM Devices", IEEE, Electron Device Letters, vol.34, 623- 625 (2013).
3. S. Long, **X. Lian**, C. Cagli, L. Perniola, E. Miranda, M. Liu and J. Suñé, "A Model for the Set Statistics of RRAM Inspired in the Percolation Model of Oxide Breakdown", IEEE, Electron Device Letters, vol.34, 999-1001(2013).
4. **X. Lian**, E. Miranda, S. Long, L. Perniola, M. Liu, J. Suñé, "Three-state resistive switching in HfO2-based RRAM", Solid-State Electronics, in press 2014.
5. **X. Lian**, X. Cartoixà, E. Miranda, L. Perniola, R. Rurali, S. Long, M. Liu and J. Suñé, "Multi-scale Quantum Point Contact model for filamentary conduction in RRAM devices", submitted in Nanoscale, 2014.

## Other Publications

6. S. Long, L. Perniola, C. Cagli, J. Buckley, **X. Lian**, E. Miranda, F. Pan, M. Liu and J. Suñé, "Voltage and power-controlled regimes in the progressive unipolar RESET transition of $HfO_2$-based RRAM", Scientific Reports, vol.3, 2929(2013).
7. M. A. Villena, F. Jimenez-Molinos, J. B. Roldán, J. Suñé, S. Long, **X. Lian**, F. Gámiz and M. Liu, "An in-depth simulation study of thermal reset transitions in RRAM", Journal of Applied Physics, vol.14, 144505(2013).
8. X. Saura, **X. Lian**, D. Jimenez, E. Miranda, X. Borrisé, F. Campabadal and J. Suñé, "Field-effect control of breakdown paths in $HfO_2$ based MIM structures", Microelectronics Reliability, 2013;53(9-11):1346-1350.
9. X. Yang, S. Long, K. Zhang, X. Liu, G. Wang, **X. Lian**, Q. Liu, H. Lv, M. Wang, H. Xie, H. Sun, P. Sun, J. Suñé and M. Liu, "Investigation on the RESET switching mechanism of bipolar Cu/$HfO_2$/Pt RRAM devices with a statistical methodology", Journal of Applied Physics, vol.46: 245107 (2013).

## Contributions to Conferences

10. **X. Lian**, S. Long, C. Cagli, J. Buckley, E. Miranda, M. Liu, J. Suñé, "Quantum point contact model of filamentary conduction in resistive switching memories",

2012 13th International Conference on Ultimate Integration on Silicon (ULIS 2012), 2012: 101-104.

11. **X. Lian**, E. Miranda, S. Long, L. Perniola, M. Liu, J. Suñé, "Experimental evidence for a quantum wire state in $HfO_2$-based VCM-RRAM," 2013 14th International Conference on Ultimate Integration on Silicon (ULIS 2013), 2013:161-164.
12. S. Long, **X. Lian**, C. Cagli, L. Perniola, H. Lv, Q.Liu, L. Li, Z. Huo, E. Miranda, D. Jiménez, M. Liu, J. Suñé, "Compact Analytical Models for the SET and RESET Switching Statistics of RRAM Inspired in the Cell-Based Percolation Model of Gate Dielectric Breakdown", IEEE International Reliability Physics Symposium (IRPS) 2013:5A.6.1-5A.6.8.
13. X. Saura, **X. Lian**, D. Jimenez, E. Miranda, X. Borrisé, J.M. Rafí, F. Campabadal, J. Suñé, "Exploring the field-effect control of breakdown paths in lateral $W/HfO_2/W$ structures", 2013 14th International Conference on Ultimate Integration on Silicon (ULIS 2013), 2013:177-180.
14. X. Yang, S. Long, K. Zhang, **X. Lian**, X. Liu, Q. Liu, H. Lv, J. Suñé, M. Liu, "Statistical approach to the RESET switching of the $HfO_2$-based solid electrolyte memory", 2013 14th International Conference on Ultimate Integration on Silicon (ULIS 2013), 2013:149-152.
15. J. Sune; S. Long; C. Cagli; L. Perniola; **X. Lian**; X. Cartoixa; R. Rurali; E.Miranda; D. Jimenez; M. Liu, "Electrical evidence of atomic-size effects in the conduction filament of RRAM", ICSICT 2012 - 2012 IEEE 11th International Conference on Solid-State and Integrated Circuit Technology, Proceedings. 2012.
16. S. Long, C. Cagli, J. Buchley, Q. Liu, H. Lv, **X. Lian**, E. Miranda, D. Jiménez, M. Liu, and J. Suñé. "Set voltage statistics in unipolar $HfO_2$-based RRAM", 2012 International Conference on Solid State Devices and Materials (SSDM 2012). September 25-27, 2012, Kyoto, Japan.

# Presentation

Switching properties of transition metal oxides and chalcogenide glasses in Metal-Insulator-Metal were studied in the sixties and seventies. Nowadays, these properties and materials are being studied with renewed interest because they are very promising both for logic and memory applications. Phase-change RAM memories based on crystalline/amorphous transitions induced by Joule heating are already a commercial reality. However, these memories suffer from too high programming current and power. In this regard, resistive switching (RS) in formed transition metal oxides is being intensively investigated due to their promising performance as Resistive Random Access Memories (RRAM). These structures are ideal for crossbar memory arrays that are presently considered as the most promising implementation of storage class memory. These memories might replace Flash NAND and also eventually DRAM and SRAM, thus reducing the memory hierarchy. On the other hand, formed oxides have allowed the first solid-state device implementation of the memristor, a device theoretically anticipated by Chua in 1971. This device is very promising for reconfigurable logic applications and for the implementation of neuromorphic computer architectures.

There are two important issues which presently hinder the transfer of RS results to industrial application, (i) a lack of adequate understanding of the physics of the mechanisms of RS and (ii) the statistical variation of switching parameters during cycling and from device to device, and reliability issues such as retention at high temperature. Based on these two reasons, this dissertation is divided into five parts.

Chapter 1 will be devoted to introduce the research background and the basic concepts and terminologies about RRAM devices. In Chapter 2, the quantum point contact (QPC) model and ab-initio simulations of oxygen vacancy paths will be applied to a thorough statistical study of $HfO_2$-based RRAM devices in different switching modes. In Chapter 3, the compact analytical models for the set and reset switching statistics of RRAM inspired in the cell-based percolation model of gate dielectric breakdown will also be studied in detail, which is on the base of VCM structures in both bipolar and unipolar cases. Chapter 4 is dedicated to reveal

three-state resistive switching phenomena using three different electrical methods: ramp-voltage sweep (RVS), successive-voltage sweep (SVS) and constant-voltage stress (CVS). Chapter 5 is the conclusion about the entire dissertation research results.

# Chapter 1

## Introduction

In the current digital era, there is a pressing demand to find a new kind of „universal‟ memory with high density, high speed, and low energy requirements, and data would be preserved even without a power supply. Dynamic random access memory (DRAM) and static random access memory (SRAM) are fast and provide good performance but are volatile, i.e. data is lost when the power supply is removed. Hard disk drives (HDDs) are a cheap nonvolatile memory and data is preserved in the absence of a power supply, but which are limited by relatively poor performance, speed, and reliability. Flash is another type of solid-state nonvolatile memory that, although it cannot be used as a computer‟s main memory, has found niches in solid-state hard disks, digital cameras, and cellular phones. Although it has the advantage of being nonvolatile, it has a slow write speed and can only withstand a limited number of read/write cycles[1]. Therefore, a „universal‟memory is continuing to be researched nowadays.

Resistive Random Access Memories (RRAM) based on the resistive switching (RS) effect of transition metal oxides (TMOs) is widely accepted as a promising candidate for future non-volatile memory applications due to its simple structure, good scalability, high switching speed, low operation current and power. This dissertation mainly focuses on $HfO_2$-based RRAM, which is motivated by the industry requirements of compatibility with complementary metal-oxide-semiconductor (CMOS). Although it might seem that this material is thoroughly studied, its application to RRAM is still in its infancy.

This chapter will be devoted to introduce some basic concepts and terminologies about RRAM that are necessary to understand the whole dissertation. The first part is contributed to describe about the RS mechanism and about the research background for RRAM devices. In the following parts, the applications of resistive switching

devices and the research aim of this thesis will be introduced.

## 1.1 Resistive switching mechanism

This dissertation focuses on a kind of devices which are called RRAM with intrinsic non-volatile memory (NVM) properties revealed by a change of resistance. The operating principle of RRAM is based on the reversible RS between at least two stable resistance states, the high resistance state (HRS) and the low resistance state (LRS), which occurs in transition metal oxides when subjected to electrical stimulus in simple metal-insulator-metal (MIM) or metal-insulator-semiconductor (MOS) capacitor configurations. The switching event from HRS to LRS is called the “set” process and from LRS to HRS is called the “reset” process. These devices involve both electrons and ions in their operation. Ions are responsible for the information storage, thus overcoming the difficulty of confining electrons within potential barriers in ultra-scaled devices. Usually for the fresh samples in its initial resistance state, a voltage larger than the set voltage is needed to trigger on the RS behavior for the subsequent cycles. This is called the “electroforming” or “forming” process[2, 3]. Electroformed oxides present two main types of RS which are called memory switching[4] (MS) and threshold switching[5, 6](TS), respectively. While the MS is a non-volatile phenomenon, with the two resistance states being stable at zero bias, the TS phenomenon is volatile and occurs in a limited voltage range[7, 8], as shown in the Fig. 1.1.

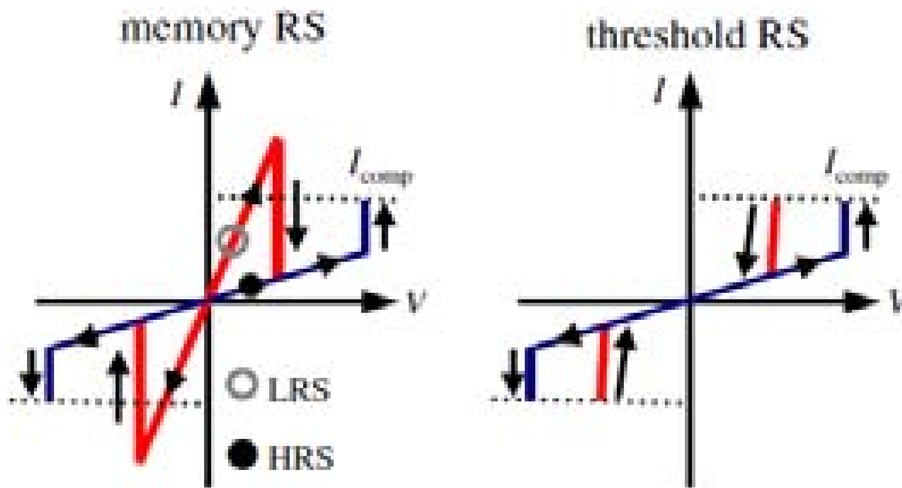


**Fig.1.1** Schematic chart of resistive switching (MS and TS) loops showing the two-branch I-V characteristics and the set and reset transitions between them, (a) MS is non-volatile phenomenon, with the two resistance states being stable at zero bias, (b) The TS phenomenon is volatile and occurs in a limited voltage range.

Depending on whether the same or opposite polarity is applied for the transition from the HRS to the LRS and vice versa, the switching modes of RRAM is referred to as unipolar or bipolar, respectively. In the unipolar case, the switching from the HRS to the LRS occurs under the same voltage polarity as the switching from the LRS to

the HRS. If the unipolar switching can symmetrically occur at both positive and negative voltages, it is also referred as a nonpolar switching mode[3]. In the case of bipolar switching, writing and erasing occur under different polarities. For each switching mode, in order to avoid a permanent dielectric breakdown, it is recommended to apply a current-limit in the set process. In the majority of cases, switching is local, taking place in a conducting filament (CF) [9] created during electroforming, in a process which is very similar to a soft-breakdown event[9]. Thus, much of the knowledge gained about oxide breakdown (BD) in the field of complementary metal-oxide-semiconductor (CMOS) reliability can now be very useful in the field of RS devices[10, 11]. The nature of the CF is different in different material systems[12-14], and so do the conduction properties and the physics of the RS transitions. In some other cases, mainly in MIM structures with a Schottky metal-insulator barrier, the insulator being a complex perovskite oxide, the RS phenomenon has been demonstrated to be uniform in the whole area of the device[15].

Research on RS dates back to the early 1960"s when TS[5, 6] and MS[4] were observed for the first time. These early studies reached a significant level of understanding[16], however, the immature status of material processing and device integration technology hindered its further development. As the physical limitations of charge-based NVM are being approached, the interest in RS applications has recently revived[17, 18]. The interest was further raised when these devices were linked to the memristor[19], the fundamental circuit element predicted in 1971 by Chua[20]. The current research on RS started in the late 1990s[21, 22], triggered by Asamitsu et al.[23], Kozicki et al.[24] and Beck et al.[25], first with complex metal oxides such as the pervoskite oxides of $SrZrO_3$ [25], $SrTiO_3$ [26], and later the binary metal oxides such as NiO [17] and $TiO_2$ [27]. Research on RS began to intensify after 2004 when Samsung demonstrated that NiO memory cells can be integrated with CMOS in a one-transistor-one-semiconductor (1T1R) device structure[3, 28].

The switching behavior is not only dependent on the transition metal oxides but also dependent on the metal electrodes and their interfacial properties. Waser[29] classified these switching and conductive mechanisms of RRAM in three different categories according to the operation mechanism: (i) the bipolar electrochemical mechanism (ECM); (ii) the valence change mechanism (VCM) [30] and (iii) the thermochemical mechanism (TCM) [31]. The ECM[32] cells, also called programmable metallization cells (PMC) or conducting bridge RAM (CBRAM), rely on a metallic CF formed from an active metal electrode such as Ag or Cu. The VCM occurs in specific transition metal oxides and is triggered by the migration of oxygen anions (usually described by the motion of the corresponding oxygen vacancies). A subsequent change of the stoichiometry leads to a redox reaction expressed by a valence change of the cation sublattice and a change in the electronic conductivity. The third class relies on a thermochemical mechanism which leads to a change of the stoichiometry due to a current-induced increase of the temperature. Traditionally, RS has been considered to occur without a phase change, thus excluding the amorphous to crystalline phase change of chalcogenide materials, which is the key element of phase-change random access memory (PCRAM) and optical disks[33, 34]. However, the

boundary between the different categories blurred as the microscopic identity of switching element is revealed. The details of the physical mechanisms of resistive switching are still not fully understood and are the subject of ongoing research.

This thesis is dedicated to study the switching properties and statistics of VCM and PMC structures in both bipolar and unipolar cases for RRAM devices.

## 1.2 Applications of Resistive switching devices

Resistive switching devices have applications which might represent real breakthroughs in at least three fields that might have a large impact in the Information and Communication Technologies market: (a) RRAM non-volatile memory (NVM), (b) memristor-based reconfigurable nanoelectronics and (c) neuromorphic computing architectures for truly intelligent self-learning systems, as shown in Fig. 1.2.

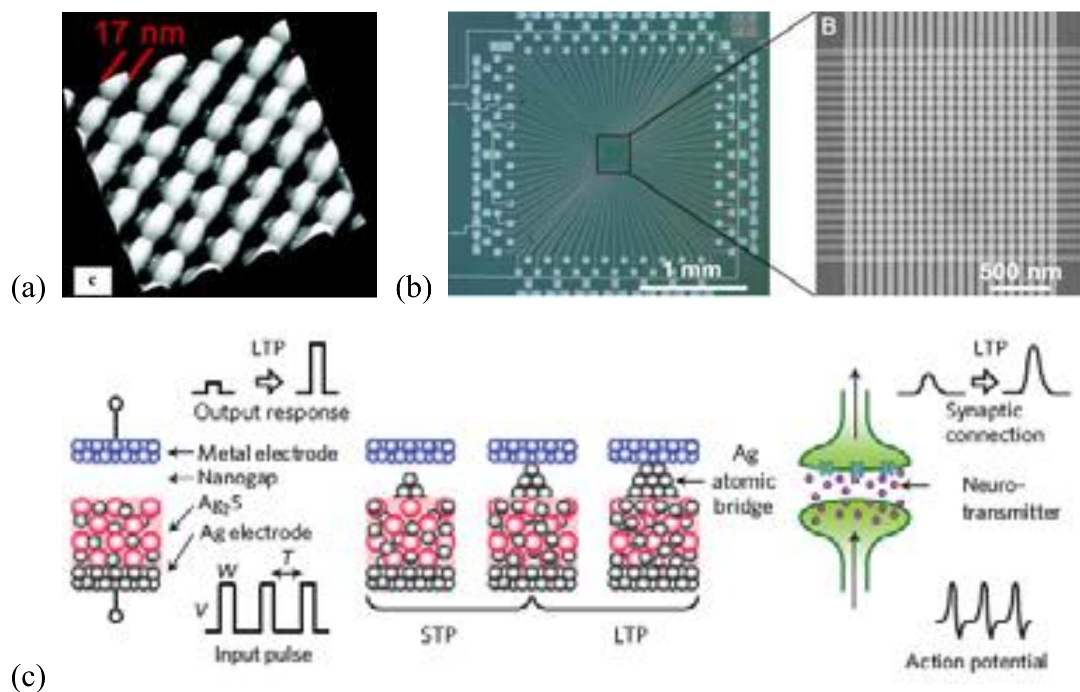


**Fig. 1.2** Applications of RS devices (a) 8×8 crossbar array of 17nm half pitch for non-volatile memory; (b) self-reconfigurable CMOS/memristor hybrid circuits. (c) Emulating synapsis in neuromorphic intelligent hardware[35].

### 1.2.1 Non-volatile memory

There is a pressing demand to find new simple, scalable, low-power solutions to replace hard disc drives (HDD) and non-volatile Flash NAND or NOR memories. Moreover, innovation in the storage memory hierarchy can bring substantial performance improvement to computing systems and data centers by reducing access time[36] and power consumption[37]. Thus, different memory technologies are considered[38-40] for the implementation of the storage-class memory concept[41]. A high interest is also on System-on-Chip (SoC) for embedded or low-power applications,

which are the main strengths of RRAM compared to other technologies. Although oxide-based RRAM memories are one of the most promising, they still face some limitations in terms of reliability, endurance and data retention at high temperature, so that further completed research about RRAM is discussed in this thesis.

### 1.2.2 Reconfigurable computing architectures

Crossbar arrays of memristive devices (a two-dimensional grid of metal lines with a RS material at each crossing point) offer many advantages for computing at the nanoscale: it is scalable down to the molecular scale[42]; it is a regular structure that can be configured by closing junctions and reconfigured to tolerate defects in the circuit[43], and due to its structural simplicity it can be fabricated inexpensively with Nanoimprint lithography[44]. Hybrid circuits combining CMOS technology with nanoscale switches in crossbars, called CMOS molecule (CMOL) [45] and field-programmable nanowire interconnects (FPNI)[46], have been proposed. These field programmable gate array (FPGA)-like architectures combine the advantages of CMOS with the reconfigurability and scalability of nanoscale crossbars, thus allowing significant reductions of total FPGA area while simultaneously increasing the clock frequency and decreasing the power consumption[45, 46]. These architectures also allow the conditional self-programming, i.e. the circuit can reconfigure itself and modify its own structure depending on the results of its own calculations[47]. Moreover, reconfigurable memristor interconnections should allow that each computing component only turns on long enough to get the job done, thus avoiding the use of energy for actually "doing nothing", thus significantly improving the energy efficiency. Last but not least, the use of memristors has also been proposed for reconfigurable analog circuits[48].

### 1.2.3 Neuromorphic circuits

The human brain outperforms computers in many computational problems like the faster and energy efficient recognition of complex images[49]. To reach the complexity of the human brain, artificial neural networks would need to contain roughly $10^{11}$ neurons and about $10^{15}$synapses. The birth of the memristor launched huge research efforts in the field because these devices are small enough, cheap enough and efficient enough for the practical implementation of these high-performance neuromorphic intelligent systems[50]. Jo et al. recently demonstrated that a hybrid system composed of CMOS neurons and nanoscale silicon-based memristors can support important synaptic functions such as spike timing dependent plasticity[51]. The recent results by Wong‟s group at Stanford University[52, 53] and Aono‟s group in Japan[54, 55], recently reported the synthesis of inorganic artificial synapses that bring viable technology for artificial neural networks closer. Both of them are also based on RS devices. Although these systems might still sound as science-fiction, challenging pilot applications are being funded such as the fabrication of intelligent cars that can drive themselves in previously unexplored environments without human intervention[50].

In this thesis, RRAM-NVMs will be studied with two general goals focused on NVMs: (i) unveiling the physics of the switching and conduction mechanisms and (ii)

exploring and modeling the switching statistics for set and reset processes.

## 1.3 The research aim of the thesis

RRAM based on the RS effect of transition metal oxides (TMOs) is widely accepted as a promising candidate for future non-volatile memory applications due to its simple structure, good scalability, high switching speed, low operation current and power, and ease of integration in the back end of the line of CMOS processing[56]. There are two key issues which presently hinder the transfer of RS results to industrial application, (i) a lack of adequate understanding of the physics of the mechanisms of RS and (ii) the statistical variation of switching parameters during cycling and from device to device, and reliability issues such as retention at high temperature. Improvement in these two directions should allow structured material design strategies for improved device engineering that would finally foster the transfer to market applications.

Understanding the physics of the mechanisms of RS [57-59] is of key importance not only to optimize the RRAM devices and programming/erasing/read algorithms but also to provide insight on the retention and endurance. RS in MIM devices is often based on the creation and partial destruction of a CF of nanoscale dimensions. Hence, understanding the conduction properties of the CF in the LRS and the HRS and linking these properties to the shape and nature of the CF is of great importance to improve the understanding of RS and to boost RRAM applications. On the other hand, the device to device and cycle to cycle variability are problems which negatively affect the application of RRAM arrays and need to be improved by processing and/or operation algorithms[60]. Therefore, the understanding of the switching mechanism and the description of the statistics of set and reset voltage, current and power correlated to the statistics of set and reset state resistances are necessary and will be explored in the following chapters. A suitable physics-based model of the switching statistics might become the core of a general framework to deal with the reliability performance tradeoffs. Among all kinds of TMOs materials, $HfO_2$ might be one of the most competitive RS functional materials for RRAM [61-63]. In this thesis, I mainly did the research for $HfO_2$-based RRAM devices.

Based on the above reason, the thesis is divided into three main parts. The first part is dedicated to reveal the nature of the CF, its conduction properties and the mechanisms which control its formation and disruption. The quantum point contact (QPC) model, originally developed for soft and hard breakdown events[64, 65] in thin-oxide MOS devices, is applied to $HfO_2$-based resistive switching structures[66]. In this thesis, the QPC model for CF conduction has been reformulated by coupling it to the results of ab-initio simulations of oxygen vacancy paths. The model provides an analytical description for CF of RRAM devices both in the LRS and the HRS. Fitting of the experimental I-V characteristics in both the LRS and the HRS provide indirect information about the microscopic structure of the CF. The new QPC model has been applied to a thorough statistical study of unipolar RS in Pt/$HfO_2$/Pt and to bipolar (and unipolar) RS in Pt/Ti/$HfO_2$/Pt devices. The obtained results have revealed significant

differences in the properties of the CF in these two types of devices. This is consistent with the expected differences in the concentration profile of oxygen vacancies due to the presence/absence of an oxygen extraction layer.

The second part is dedicated to study the statistical variation of switching parameters of RRAM devices. Departing from the cell-based percolation model of gate dielectric breakdown to propose an analytical model for set and reset statistics in RRAM devices. The model is composed of two basic elements: (i) a cell-based geometrical model to describe the dependence of the RS distribution on the defect generation in the CF, and (ii) a deterministic model for the set/reset dynamics to describe the relation of the defect generation with measurable variables such as the set/reset voltages and currents. The experimental observations in $HfO_2$-based RRAM devices can be successfully accounted for by our model for RS statistics. The model sets a framework for the consideration of performance-reliability tradeoffs in RRAM.

The third part will be focused on revealing three-state resistive switching effects for $HfO_2$-based RRAM devices using three different electrical methods: ramp-voltage sweep (RVS), successive-voltage sweep (SVS) and constant-voltage stress (CVS). We study nonpolar switching in Pt/$HfO_2$/Pt and unipolar/bipolar switching in Pt/Ti/$HfO_2$/Pt structures, respectively. However, three-state resistive switching is only confirmed in the former case by means of various reset methodologies. Between the LRS and the HRS, a rather stable intermediate state is revealed and shown to have the properties of a quantum wire (QW). This QW state is characterized by having conductance of the order of $G_0 \sim 2e^2/h$ and represents a natural boundary between two different electron transport regimes. Above the $G_0$ limit, the conduction is associated to extended quantum transport states which connect the two electrodes, while below it, a spatial gap is opened in the conducting filament (CF) and the conduction is controlled by hopping or tunneling. Using two-step reset experiments it is shown that the transition to the complete reset state occurs at higher voltages if the CF first drops to the intermediate state.

## 1.4 Summary

In this chapter, the research background and the basic concepts and terminologies about RRAM have been introduced. Resistive switching mechanism, including the operating principle of RRAM, RS process, RS model (unipolar and bipolar) and RS behavior (classified by Waser[29]) has been explained. The applications of resistive switching devices: (a) RRAM non-volatile memory (NVM), (b) memristor-based reconfigurable nanoelectronics and (c) neuromorphic computing architectures have been briefly introduced. Finally, the research aim of this thesis also has been given.

In the following chapters, the QPC model and ab-initio simulations of oxygen vacancy paths will be applied to a thorough statistical study of $HfO_2$-based RRAM devices. The QPC model is based on the idea that the BD path (or the CF in RS devices) can be modeled as a QW, and it has been successfully applied to model the conduction properties of the CF in RRAM devices both in the HRS and the LRS. Besides, the compact analytical models for the set and reset switching statistics of

RRAM inspired in the cell-based percolation model of gate dielectric breakdown will also be studied in detail, which is on the base of VCM structures in both bipolar and unipolar cases. Furthermore, three-state resistive switching phenomena will also be shown in the dissertation. According three different electrical methods, a quantum wire state is revealed by having conductance of the order of $G_0 \sim 2e^2/h$.

In the last chapter, the conclusion about my Ph.D. research will be summarized.

# Chapter 2

## The Quantum Point Contact Model for RRAM

The Quantum Point Contact (QPC) model was originally proposed for the conduction after the breakdown (BD) of gate oxides in MOS devices, and it successfully explained the properties of both hard and soft BD paths in the same framework[64, 65]. The QPC model is based on the idea that the conducting filament (CF) behaves as a quantum wire (QW) and in this thesis it is shown to adequately describe the conduction in the low resistance state (LRS) and in the high resistance state (HRS) of filamentary in RRAM devices.

In this chapter, the QPC model is applied to model the BD conduction properties of the CF in $HfO_2$-based RRAM devices both in the HRS and the LRS. The first part is devoted to describe the QPC model for multiple BD paths in MOS devices on the basis of the Landauer transmission approach to conduction along narrow microscopic constrictions. After obtaining the useful formulas for QPC model, the experimental results corresponding to $HfO_2$-based RRAM devices is analyzed to demonstrate that the QPC model which is adequate for both LRS and HRS. In the third section, the QPC model will be reformulated by coupling it to the results of ab-initio simulations of oxygen vacancy paths. Finally, fitting of the experimental I-V characteristics in both the HRS and the LRS will be shown to indirect information about the microscopic structure of the CF for Pt/Ti/$HfO_2$/Pt and Pt/$HfO_2$/Pt structures.

### 2.1 The QPC Model for multiple breakdown paths

In MOS devices with ultrathin gate oxides, two BD modes are loosely identified as soft-BD (SBD) and hard-BD (HBD). While the current-voltage (I-V) is linear after HBD, it is strongly non-linear after SBD. In spite of these differences, the QPC model

is adequate to deal with both HBD and SBD within a common framework[64, 65]. As shown in Fig. 2.1, this model assumes that the BD conduction takes place through a CF which is narrow enough to quantize the energy in the two directions perpendicular to the electron transport, thus behaving as a quasi-1D system.

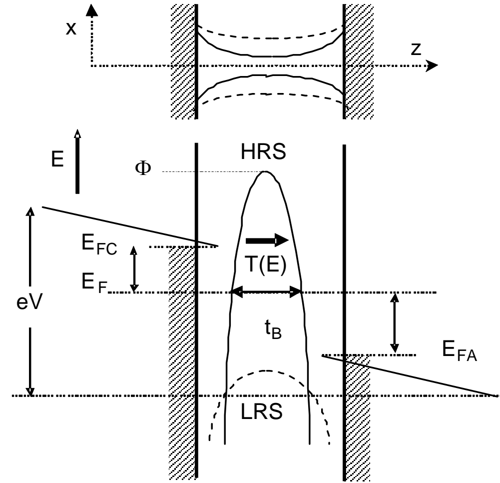


**Fig. 2.1** Schematic representation of a conducting filament with different width and the corresponding energy band diagram which includes a potential barrier with height inversely correlated to the CF constriction width. The narrower is the section of the constriction at its narrowest point, the higher is the barrier.

Many different conduction models have been proposed for the HRS including trap-assisted tunneling[66], Poole-Frenkel conduction[67], thermally activated hopping[68], space-charge limited current[69], and QPC model[64, 65], among others. The QPC model provides a smooth transition from tunneling in the HRS to Ohmic conduction in the LRS and explains the conductance quantization effects. The QPC model is based on the idea that the BD path (or the CF in RS devices) can be modeled as a QW, and it has been successfully applied to model the conduction properties of the CF in RRAM devices both in the HRS and the LRS. This model is based on the Landauer transmission approach to conduction along narrow microscopic constrictions and it assumes that the CF is a quasi-one dimensional system of electron states. The area of the most constrictive section of the CF determines the energy of the subbands available for transport along the CF. If the CF is wide, the position of this first subband is below the electrode Fermi level and the conduction is essentially linear with a conductance of the order of $G_0 = 2e^2/h$ or larger. On the contrary, if the CF is narrow, the energy of the first subband might be above the electrode Fermi level and this would introduce a potential barrier which, depending on its height and thickness, might result in a CF conductance several orders of magnitude below $G_0$ and strongly non-linear I(V). This basic modeling framework has been assumed by different groups with some small different details. Miranda[70] has considered a bundle of N of conducting single-subband CFs in the LRS and a single channel with a

parabolic barrier in the HRS. Degraeve[10] described the filament as a saddle potential energy surface and extracted the model parameters from many reset I-V curves, thus providing evidence that the dominant microscopic evolution of the CF during reset consists in the progressive narrowing of the constriction.

According to the Landauer"s approach, the current flowing through a CF with N vacancy paths can be calculated as[71]:

$$I(V) = \frac{2e}{h} N \int_{-\infty}^{\infty} T(E)\{ f(E-\beta eV) - f(E+(1-\beta)eV)\}\, dE \tag{2-1}$$

where $E$ is the energy, $T(E)$ is the transmission probability, $f$ is the Fermi-Dirac distribution function, $e$ and $h$ are the electron charge and the Planck constant, and $V$ is the applied voltage which is assumed to drop at the cathode and anode interfaces with the QPC in a fraction of $\beta$ and (1- $\beta$ ), respectively (see Fig. 2.2).

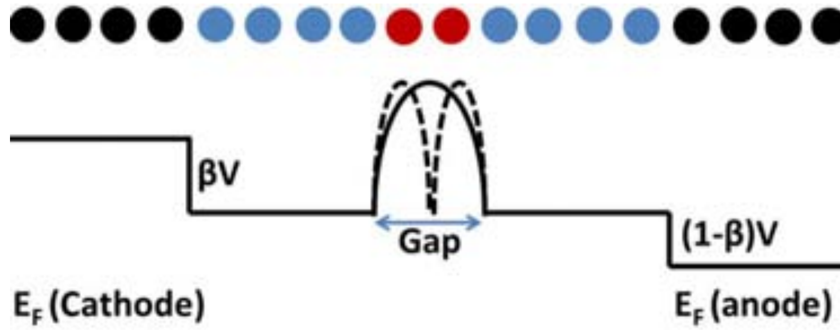


**Fig. 2.2** Schematic representation of a single vacancy path with two re-oxidized vacancies and the associated voltage profile under bias.

Assuming an inverted parabolic potential barrier allows to obtain an analytical expression for the tunneling probability[72-74], $T(E) = \{1 + exp[-\alpha(E-\Phi)]\}^{-1}$, where $\Phi$ is the barrier height and $\alpha = t_B \pi^2 h^{-1}\sqrt{2m^*/\Phi}$ is related to the inverse of potential barrier curvature, $m^*$is the effective electron mass and $t_{\mathrm{B}}$ is the barrier thickness at the equilibrium Fermi energy, assumed to be equal to $t_{\mathrm{gap}}$. Inserting the transmission coefficient into Eq (2-1):

$$I = \frac{2e}{h} N \left\{ eV + \frac{1}{\alpha} Ln\left[\frac{1+exp\{\alpha[\Phi-\beta eV]\}}{1+exp\{\alpha[\Phi+(1-\beta)eV]\}}\right]\right\} \tag{2-2}$$

This equation can be applicable to both the HRS and the LRS depending on the values of $\alpha$ and $\Phi$, which describe the potential barrier.

In the LRS, the CF is fully formed and wide enough so that the Fermi level of the injecting electrode is above the bottom of the ground subband. Thus, the I-V is linear because there is no barrier to limit the transmission, and equation (2-2) converges to:

$$I = \frac{2e^2}{h} NV = G_0 NV \tag{2-3}$$

when both the anode and cathode Fermi levels are above the top of the potential barrier. If the Fermi level at the anode were below $\Phi$, then the conductance would be reduced to $N\beta G_0$. On the other hand, when the CF is narrow enough (i.e. after the RESET cycle)

it presents a finite potential barrier to transmission that causes the conduction to be strongly non-linear. This barrier is related to the fact that the bottom of the ground quantized subband is above the Fermi level of the cathode. These two conduction regimes and the smooth transition between them appear naturally in the QPC model. Moreover, the quantum of conductance， $G_0 = 2e^2/h$ appears as a natural boundary between a fully formed CF with metallic properties and linear I-V and a partially formed filament with strongly non-linear conduction properties.

In the HRS, if there is a gap with a potential barrier, the equation (2-2) is found to converge to:

$$I \approx \frac{2e^2}{h} Nexp(-\alpha\Phi)\left[V + \frac{\alpha\beta}{2}V^2\right] \tag{2-4}$$

at low voltages and for high enough barriers. The first factors of equation (2-4) determine the current and conductance at low voltages, so that the equivalent transmission probability is $T = \exp(-\alpha\Phi)$. The second factor is the departure from linearity.

The QPC model provides an analytical description for both the LRS and HRS in RRAM devices. In the second section, experimental results corresponding to $HfO_2$-based RRAM devices further demonstrate that our QPC model is adequate for both LRS and HRS. In the third section, the QPC model will be reformulated by coupling it to the results of ab-initio simulations of oxygen vacancy paths. Fitting of the experimental I-V characteristics in both the LRS and the HRS provides indirect information about the microscopic structure of the CF.

## 2.2 Experimental results of QPC model in the HRS and LRS

The QPC model is applied to experimental results corresponding to $Pt/HfO_2/Pt$ structure with an area of 2.5 $\mu m^2$ and a thickness of 10nm $HfO_2$, which was deposited by atomic layer deposition (ALD) at 350 °C on the Pt bottom electrode (BE) prepared by physical vapor deposition (PVD), followed by the fabrication and pattering of the Pt top electrode (TE) using PVD and etching. The $Pt/HfO_2/Pt$ structure shows a nonpolar behavior, which means that both the set and the reset transitions can be produced by positive or negative bias.

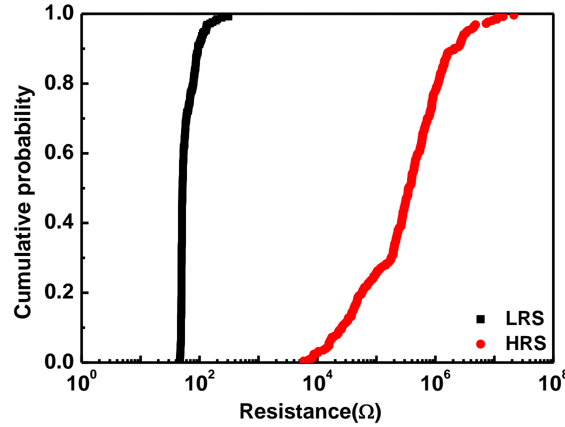


**Fig. 2.3** Statistical distribution of resistances in the HRS and LRS during 250 switching cycles measured in $Pt/HfO_2/Pt$ samples. Resistances measured at low voltage.

As shown in Fig. 2.3, the statistical variation of resistance in HRS is larger than the LRS in the case of ramp voltage switching (RVS). As a consequence, in order to check the applicability of the QPC model to the HRS, we need to consider I-V curves with different values of initial conductance. After selecting a significant number of I-V curves covering the whole range of initial conductance, a least square-estimation (LSE) method has been used to extract the three parameters of the model (α, β and $\Phi$), considering that a single CF dominates the conduction ($N = 1$) when the overall low-voltage conductance is below $G_0$. For higher values of conductance (i.e. the CF in the LRS), the I-V is found to be linear as expected from the model and we can safely assume that there is no potential barrier limiting the transport so that the data is fit to equation (3). Fig. 2.4 shows the experimental fitting results using the QPC model in the HRS of $Pt/HfO_2/Pt$ structures. The obtained fitting results are excellent in a conductance range spanning six orders of magnitude. From the log-log plot, we can see that the I-V is linear at low voltages and becomes non-linear above 1V until the set voltage. This type of behavior has been widely reported in the literature, where it has been attributed to a space-charge limited current mechanism. These results demonstrate that this is not the single possible interpretation since tunneling through a potential barrier also yields a linear dependence at low enough bias and a transition towards non-linearity at higher voltages. These fitting results demonstrate that the QPC model is adequate to deal with the conduction properties of the HRS.

Fig. 2.5 shows the correlation between the values of $\Phi$ and α extracted by LSE from the experimental data. Each point corresponds to a different I-V curve in the HRS (measured after different RESET cycles). The conductance of the CF has been classified in four ranges roughly represented by the values shown in the legend. There is a clear correlation between the conductance of the CF and the product αΦ. Fig. 2.6 shows the dependence of $\alpha\Phi$ and αβ on the initial conductance of CF. No clear trend is found for αβ although a certain decrease is observed as a function of the CF conductance. Assuming that the voltage drop assymetry (i.e.) does not change, the slight decrease of αβ can be attributed to a reduction of the barrier thickness

(reduction of the CF gap) for higher CF conductance. However, the dispersion of $\alpha\beta$ is large enough to impede any sound conclusion about how the CF geometry evolves during RESET. On the contrary, the perfect straight line describing the dependence of $\alpha\Phi$ on initial conductance indicates that the CF initial conductance is fully determined by the barrier transmission. These results show that the QPC model is consistent with the experimental CF conduction properties in the HRS. The extrapolation of this straight line to $\alpha\Phi = 0$ (transmission probability equal to 1) converges to an initial CF conductance equal to $G_0$ (yellow circle) which is the boundary between the HRS and the LRS.

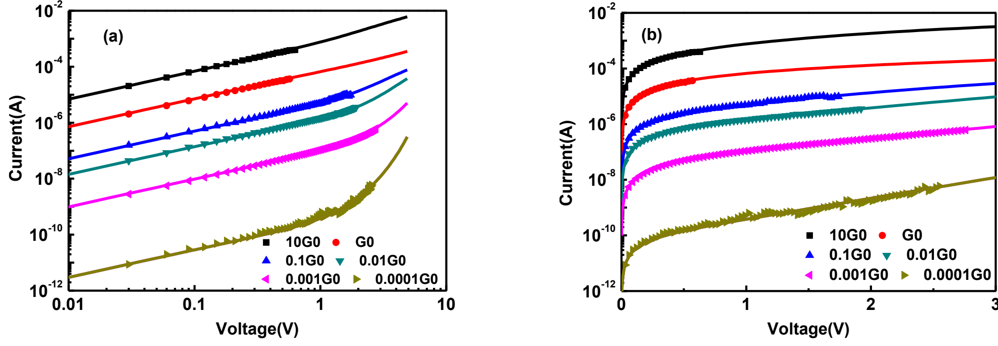


**Fig. 2.4** Fitting of the experimental I-V curves in the HRS and LRS of Pt/$HfO_2$/Pt structures to the QPC model. (a) log-log IV plots. (b) log-linear IV plots. The conductance of the CF is classified in six ranges spanning six orders of magnitude.

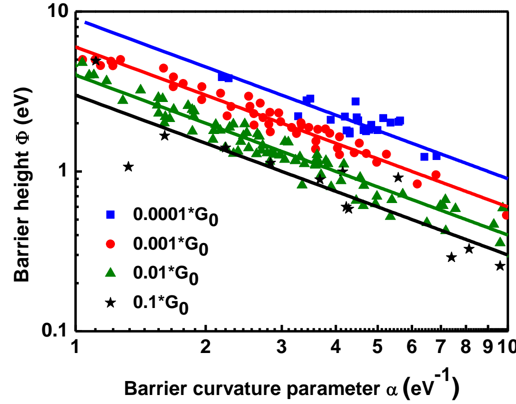


**Fig. 2.5** Correlation between the values of $\Phi$ and $\alpha$ extracted by LSE from the experimental data. Each point corresponds to a different I-V curve of the CF in the HRS (measured after different RESET cycles). The conductance of the CF has been classified in four ranges roughly represented by the values shown in the legend. The four lines correspond to $\alpha\Phi$=constant.

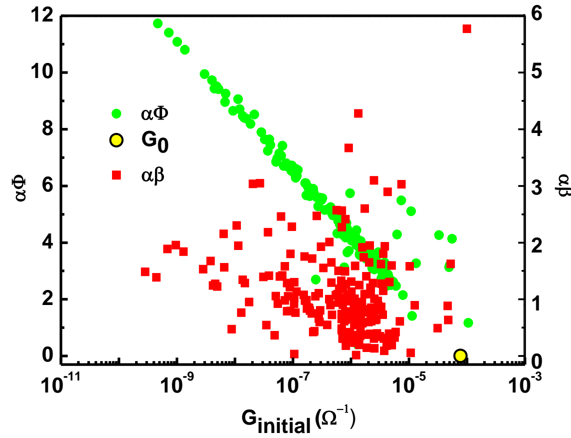


**Fig. 2.6** The QPC model parameters versus initial conductance of the CF. These results show that the product $\alpha\Phi$ determines the initial conductance of the CF. The product $\alpha\beta$ has also some influence on conductance but it is more related to the actual shape of the constriction and determines the details of the voltage non-linearity.

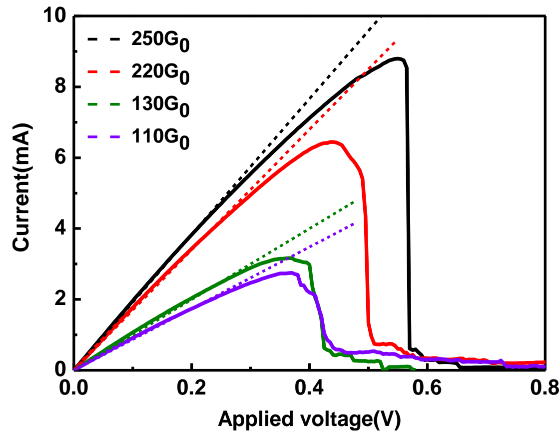


**Fig. 2.7** Current-voltage plot showing four different RESET cycles induced by a voltage ramp. The dashed lines fit the low-voltage region with LRS conductance of $110G_0$, $130G_0$, $220G_0$, and $250G_0$, respectively. The sublinearity of the experimental data is interpreted as being due to metallic temperature dependence.

As discussed in the first section, the conduction in the LRS is linear, as shown in Fig. 2.7. The initial conductance of the CF in reset experiments is much larger than the quantum of conductance. This indicates that in this particular experiment, the current compliance limit during set is large enough to create very strong (i.e. very wide) CFs which behave as classical metallic conductors. Although the linear conduction is consistent with the QPC model, these large values of conductance indicate that the conductance filament is so wide that the transversal energy quantization is negligible. A certain reduction of the conductance with voltage is observed which can be attributed to the typical temperature dependence of a metallic CF[31]. The distribution of CF conductance in the LRS spans from $100G_0$ to $250G_0$.

In conclusion, the conduction properties of resistive switching filaments have been studied in Pt/$HfO_2$/Pt structures operated in the unipolar switching mode. Both the HRS and the LRS have been shown to be consistent with the QPC model, i.e. with the assumption that the CF behaves as a quantum wire. In the HRS the conduction is strongly non-linear but a linear behavior is found at very low voltages. In the LRS, the conduction is linear and the high values of conductance suggest that the CF is composed by a number of smaller nano-filaments.

In section 2.3, the QPC model for CF conduction will be reformulated by coupling it to the results of first-principle simulations of electron transport along paths of oxygen vacancies in $HfO_2$. According to fit the experimental I-V characteristics in both the LRS and the HRS, some indirect information about the microscopic structure of the CF in two different RRAM devices can be provided.

## 2.3 Multi-scale QPC model by coupling it to the results of ab-initio simulations

In this section, we depart from first-principle simulations of electron transport along paths of oxygen vacancies in $HfO_2$ to reformulate the QPC model in terms of a bundle of such vacancy paths. By doing this, the number of model parameters is reduced and a much clearer link between the microscopic structure of the CF and its electrical properties can be provided. The new QPC model is applied to two different $HfO_2$-based devices operated in the unipolar and bipolar RS modes. Extraction of the QPC model parameters from a statistically significant number of CFs allows revealing significant structural differences in the CF of these two types of devices and RS modes.

### 2.3.1 First-principle simulations of $HfO_2$[1]

A first-principle is a basic proposition or assumption that cannot be deduced from any other proposition or assumption. In physics, a calculation is said to be from first principles, or ab-initio, if it starts directly at the level of established laws of physics and does not make assumptions such as empirical model and fitting parameters. For example, calculation of electronic structure using Schrödinger's equation within a set of approximations that do not include fitting the model to experimental data is an ab-initio approach.

In order to obtain the electronic structure of oxygen vacancy filaments in a crystalline $HfO_2$ host, the first-principle calculations is carried out on the basis of density functional theory (DFT), as implemented in the SIESTA package[75]. The exchange correlation energy is calculated within the generalized gradient approximation (GGA) in the parameterization of Perdew-Burke-Ernzerhof[76]. In order to minimize the coupling between the filament instances, which we take to be along the **c** axis for the crystalline material (see Ref. 77 for the definition of the axes), we

[1] Prof. X. Cartoixà is acknowledged for the calculations reported in this section

use a 3×3 supercell of the monoclinic unit cell ( the stable phase up to 1720℃) in the **ab** directions, sampling them in the Brillouin zone with a grid of 2×2 of **k**-points within the Monkhorst-Pack algorithm[78]. All the structures discussed have been relaxed until all the forces on the atoms were lower than 0.04 eV/Å.

The removal of a single O atom in a monoclinic-$HfO_2$ (m-$HfO_2$) matrix introduces a filled impurity state in the gap, similarly to $TiO_2$ [79], but farther from the band edges [see Fig 2.8(a)]. The extent of the impurity wavefunction determines the state overlap between two neighboring vacancies and thus relates to the transition from hopping to band transport. Fig. 2.8 (a) to (d) shows the band structure of m-$HfO_2$ with a chain of oxygen vacancies that are increasingly close together. It can be seen that, as overlap between the impurity wavefunctions increases, the impurity band width increases as well. This can be well described with a single band, second-neighbor one-dimensional (1D) tight-binding Hamiltonian, which is well known to have the dispersion relation:

$$\mathrm{E}(k_x) = E_0 - 2t_1\cos\left(k_x\frac{a}{2}\right) - 2t_2\cos(k_x a) \tag{2-5}$$

where $E_0$ is the isolated impurity energy, $t_1$ and $t_2$ are the first and second neighbor hopping parameters, closely related to the amount of overlap between the wavefunctions of neighboring impurities, and $a_0$ is the length of the **c**-axis vector for the m-$HfO_2$ primitive cell (5.296 Å). Fig. 2.8(e) shows the behavior of $t_1$ as the vacancy-vacancy distance varies, showing the expected exponential decay from which a localization parameter $\chi = 0.36a_0$ can be extracted. From the Mott criterion for metal-to-insulator transitions[80], we can find that the critical vacancy concentration is ~$1.5\times10^{21}$cm$^{-3}$, i.e. a local composition $HfO_{2-x}$ with x=0.05 will be enough to enable the band transport mechanism.

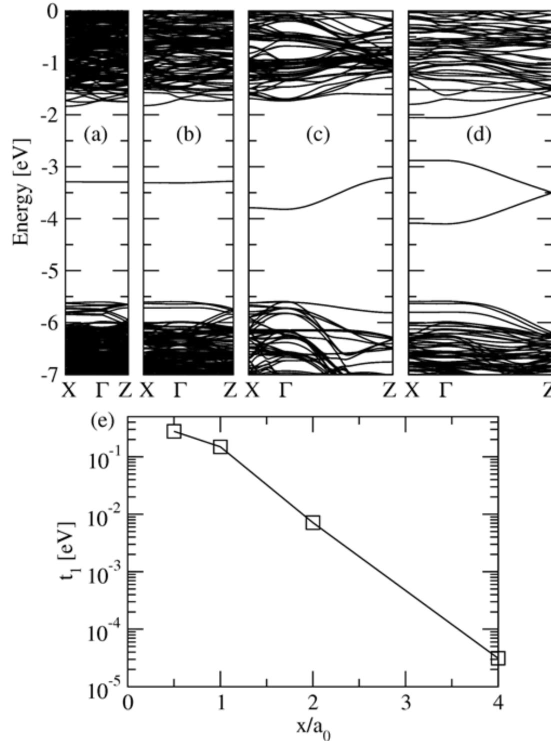


**Fig. 2.8** Band structure for crystalline m-$HfO_2$ with O vacancies separated by (a) $4a_0$, (b) $2a_0$, (c) $a_0$ and (d) $a_0/2$. (e) Hopping parameter as a function of vacancy-vacancy separation.

The ab-initio calculations of the transport properties of metal/$HfO_2$/metal structures with paths of oxygen vacancies in hafnium oxide (Fig. 2.9(a)) have demonstrated the appearance of extended bands in the gap of $HfO_2$ (Fig. 2.9(b)).Using a Green�'s function formalism coupled with a density functional theory code, the conductance of vacancy filaments of different width was calculated, showing that even the narrowest filament (one vacancy path) can sustain a conductive channel, with conductance of the order of $G_0$[81]. On the other hand, as shown in Fig. 2.9(c), each time that a vacancy is removed from the single-vacancy filament, the conductance is reduced by a factor of ~10. Taking into account that the separation between vacancies is ~0.26nm, the re-oxidation of a vacancy introduces a spatial gap in the filament which acts as a tunneling potential barrier of about this thickness. As a consequence, the conductance of the vacancy path (i.e. its barrier transmission coefficient) exponentially decreases with the gap thickness, $G = G_0 exp\left(-t_{gap}/t_0\right)$ with $t_0 = 0.12nm$, as shown in the Fig. 2.9(d).

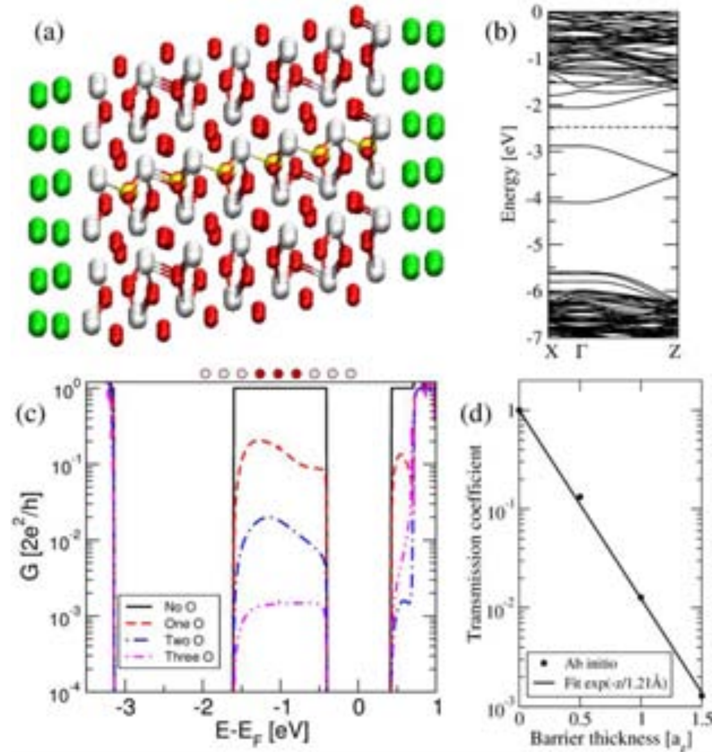


**Fig. 2.9** (a) Schematic representation of a single vacancy path (yellow balls) in monoclinic $HfO_2$, with green/red/white balls indicating metal/oxygen/hafnium atoms, respectively. (b) Band structure for the configuration of Fig. 2.9(a), without the metallic contacts, showing that the vacancy path introduces an extended band in the $HfO_2$. (c) Conductance associated to the extended band in the gap. When the vacancy filament is complete, conductance is $G_0$ and it is strongly suppressed when 1, 2, or 3 vacancies are removed (substituted by an oxygen atom). (d) The transmission coefficient as a function of the barrier thickness ($a_z$ is 0.52 nm, thus the separation between vacancies is ~0.26 nm) is reduced by a factor of ~10 when each vacancy is removed from the CF. Fitting line corresponds to $T = \exp(-t_{gap}/t_0)$ with $t_0 = 0.12\ nm$.

Given these ab-initio results, the concept of CF narrowing is only meaningful when there are N>1 vacancy paths. Further narrowing of the CF is not possible and the description of CF states with $G \ll G_0$ requires the existence of a spatial gap in the CF, i.e. at least one vacancy re-oxidized, which poses a potential barrier to electron transmission. Thus, the HRS will be described as a tunneling process through the CF gap, a process which if fully equivalent to that considered in Ref. 66.

Removing one to three oxygen columns (see inset of Fig. 2.10); we can observe that conductance increases stepwise for certain energy ranges, with each transmitting channel contributing a quantum of conductance $G_0$. When there are two oxygen vacancy paths, the conductance of CF is around $2G_0$, if three oxygen vacancy paths are in CF, the conductance is approximately $3G_0$, as shown in Fig. 2.10.

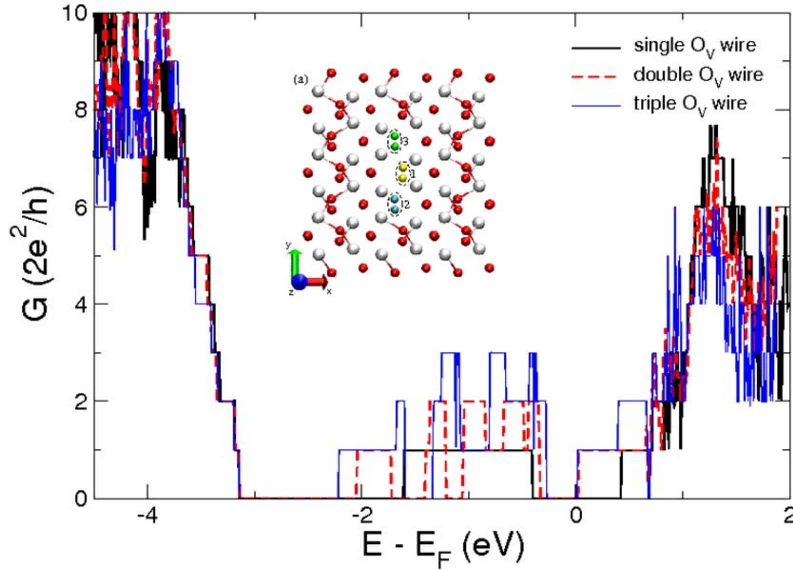


**Fig. 2.10** shows how atomic-sized changes in the CF diameter bring out significant increases in the conductance. Specifically, we show the intrinsic conductance (i.e. without the effects of the metallic electrodes) for increasingly wider CFs.

### 2.3.2 The new multi-scale QPC model coupled to ab-initio results

The HRS is described as a tunnelling process through the CF gap, as discussed in Section 2.1 to 2.3. Linking the equivalent transmission probability $T = \exp(-\alpha\Phi)$ to the thickness dependence obtained from the ab-initio results $T = \exp(-\, t_{gap}/t_0)$, we can obtain that $t_{gap} = t_0\alpha\Phi$ and $\Phi = 2\hbar^2/m^*\pi^2 t_0^2$. Assuming that $m^* \sim m_0$ (our ab-initio calculations give $m^* = 1.08\, m_0$ at the bottom of the one-vacancy electron band) results in a barrier height $\Phi \sim 1.16$ eV, which is a perfectly consistent value, given the large gap of $HfO_2$. In any case, other values of $m^*$ down to $\sim 0.5\, m_0$ would give reasonable values of $\Phi$ below 2.5 eV and will not significantly affect the quality of the fit of the experimental I-V characteristics nor the extracted information about the microscopic structure of the CF.

After reformulating the QPC model by coupling it to the results of ab-initio simulations of oxygen vacancy paths, only three free fitting parameters remain: the

number of vacancy paths *N* (i.e. the lateral size of the CF) with the constraint $N \geq 1$, the average $t_{gap}$ in these paths (for simplicity all the paths are assumed to be identical) and the average value of the asymmetry parameter $\beta$, with the constraint $0 < \beta < 1$. However, in order to simplify the fitting process, we will usually assume a fixed value of $\beta$ and extract only *N* and $t_{gap}$ from the experimental data using LSE method.

In the next section, experimental results are fit to the new QPC model and the statistics of model parameters is reported. Fixing $\Phi = 1.16\,\text{eV}$ and $\beta = 0.5$ (symmetry) or $\beta = 1$(asymmetry), we use the formula (2-2) to fit the experimental I-V curves in HRS and LRS for $HfO_2$-based RRAM devices to get the values of *N* and α ($t_{gap}$). Finally, some indirect information about the microscopic structure of the CF will be discussed using the extracted QPC parameters and their evolution during set and reset transitions.

## 2.4 Analysis of experimental results in terms of the multi-scale QPC model

Cycling experiments consisting of 1250 consecutive set/reset operations have been performed using the RVS method in two different $HfO_2$-based RRAM structures, as shown in Fig. 2.11(a). In particular, we have studied RS in Pt/$HfO_2$/Pt operated in the unipolar mode (same polarity for set and reset) and Pt/Ti/$HfO_2$/Pt structures operated under unipolar and bipolar switching modes. The considered structures are 2.5 µ$m^2$ MIM capacitors fabricated in a mesa structure on top of a tungsten plug[2]. The insulator is a 10-nm-thick $HfO_2$ layer deposited by atomic layer deposition (ALD) at 350 °C on top of the Pt bottom electrode (BE), followed by Pt (or Pt/Ti) top electrode (TE) deposition and patterning. BE and TE were deposited by physical vapor deposition (PVD). Electrical stress and measurements have been performed at the wafer level with a Keithley 4200SCS Semiconductor Characterization System. To initiate the RS behavior, an electroforming process is required to generate the CF. In all the cases, electroforming has been achieved by application of a voltage ramp with a current compliance of 1 mA (imposed by the measuring apparatus) so as to avoid the occurrence of Hard BD, which would cause the device failure and impede any ulterior observation of RS. This compliance limit is also kept during each set cycle. During the reset voltage ramp, the current is allowed to flow without external limit and the voltage is swept up to a maximum of 1 V.

[2] Dr. Barbara de Salvo is acknowledged for providing the samples which more fabricated at CET-LETI, Grenoble, France.

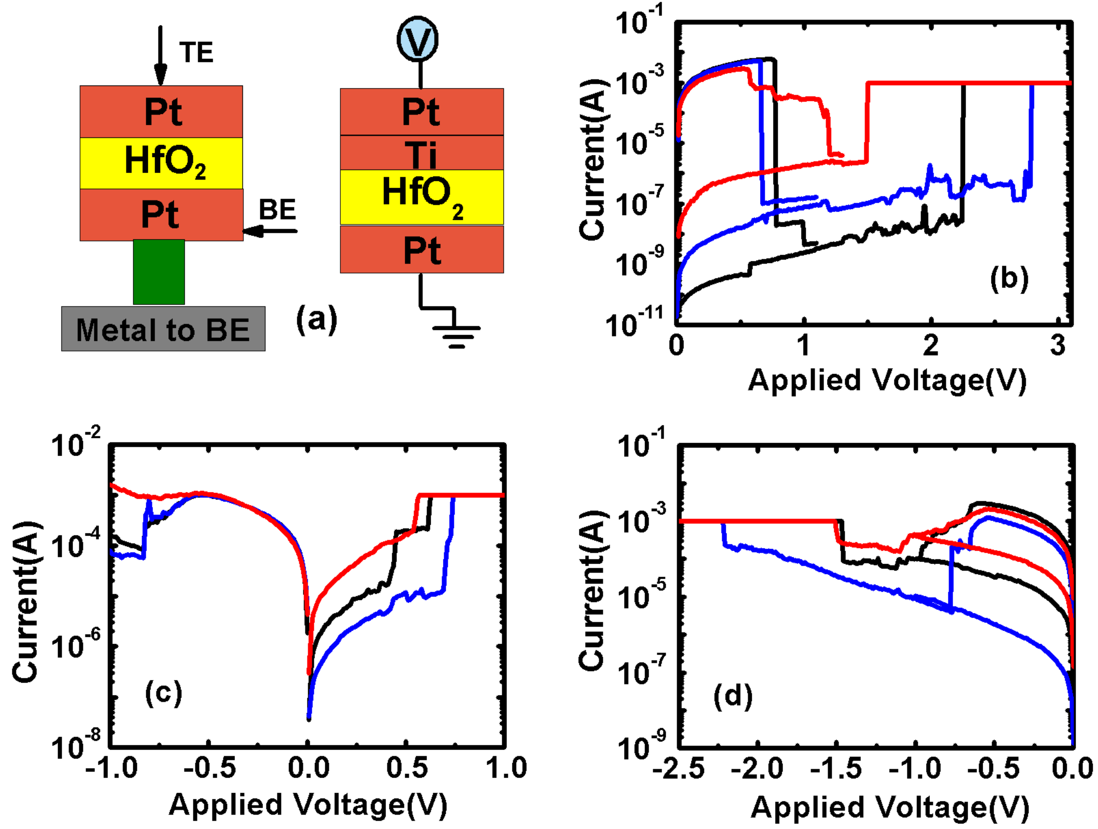


**Fig. 2.11** (a) Schematic structure of the fabricated Pt/$HfO_2$/Pt and Pt/Ti/$HfO_2$/Pt devices. (b) Typical set/reset I-V curves measured in Pt/$HfO_2$/Pt structures operated under the unipolar switching mode. Typical set/reset I-V curves measured in Pt/Ti/$HfO_2$/Pt structures operated under bipolar (c) and unipolar (d) switching modes. A current compliance of 1mA was always imposed during set to avoid destructive breakdown.

### 2.4.1 Experimental results for nonpolar Pt/$HfO_2$/Pt devices

The Pt/$HfO_2$/Pt devices are symmetric structures which show nonpolar RS, this means that Pt/$HfO_2$/Pt devices can be set or reset by any combination of voltage bias (positive/positive; negative/ negative, positive/negative and vice versa). In all these operating modes, the RS phenomenology is very similar but the results considered in this letter correspond to unipolar RS mode, i.e. a positive bias voltage ramp is applied both for set and for reset (some typical unipolar set/reset cycles are represented in Fig. 2.11(b)). After each reset cycle and after each set cycle, the new QPC model parameters are extracted by the least-square fitting of the I-V so as to have statistical information about the CF in the HRS and in the LRS. Notice that we focus on cycle-to-cycle variations of the CF and not on sample-to-sample variations. The CF conductance at low voltage is calculated as $R_{CF} = I/V$ at $V = 0.1\,V$ and a histogram of its distribution is shown in Fig. 2.12(a). In the LRS, the CF conductance peak is located at ~$100G_0$, while after reset two peaks of CF conductance are found: one narrow peak located between $G_0$ and $5G_0$ and a wide peak spanning from $10^{-5}G_0$ to $10^{-1}G_0$. In the LRS, the I-V curves are roughly linear with a small deviation from linearity at high currents, probably due to temperature dependent

conductivity[82]. The QPC model can also be applied to the LRS ($I \approx N\beta G_0 V$ in this limit) although the CF conductance is so large that the CF behaves essentially as a classical metallic wire. In this limit, the extracted number of conducting channels can be interpreted as being proportional to the area of the CF constriction.

The analysis of the properties of the CF in the HRS provides more useful information. As shown in Fig. 2.12(a) and Fig. 2.12(b), the HRS includes values of CF conductance spanning from slightly above $G_0$ down to $10^{-5}G_0$. A perfect I-V fitting is obtained in more than 5 orders of magnitude of conductance. When the CF conductance is of the order of $G_0$ or higher, the I-V is found to be linear, consistent with the idea that one or several oxygen vacancy paths connect the two electrodes through extended quasi-one dimensional electron subbands. For less conducting CFs, the I-V is found to be non-linear as the bias voltage increases. In general, the non-linearity increases with decreasing CF conductance and this corresponds to the tunneling regime. Fig. 2.12 (c) and Fig. 2.12 (d) show the extracted QPC model parameters which are only $N$ and $t_{gap}$ because $\beta = 0.5$ has been assumed for this structure and switching mode. This choice improves the quality of the I-V fitting and it is consistent with the symmetry of this RRAM structure. As shown in Fig. 2.12(c), for CF conductance below $G_0$, the best fit is obtained for $N = 1$, while for $G > G_0$ the number of conducting channels perfectly correlates with the CF conductance. On the other hand, Fig. 2.12(d) shows that there is no potential barrier for $G > G_0$ (i.e. $t_{gap} = 0$), and the thickness of the gap shows a perfect exponential correlation with the CF conductance below $G_0$, as expected for tunneling through a potential barrier. Thus, we conclude that below $G_0$, the CF has a very narrow constriction (likely one single oxygen vacancy path wide) with a spatial gap that ranges from 0 to 1.4 nm. This thickness range indicates that the gap can be estimated to be of up to ~6 re-oxidized vacancies in the least conductive CFs. Given that the CF conductance in the LRS is of the order of $10^2 G_0$, the conductance ratio of LRS to HRS can be as large as $10^7$. This large change is achieved by combining the narrowing of the CF from ~267 vacancy paths to one single path followed by the opening of a gap. Although the change of conductance is very large, it is concluded that the gap thickness (<1.4 nm) is only a small portion of the total CF length (10 nm). The long CF stumps that remain after each reset cycle explain why the spatial location of the CF likely remains the same along the very large number of set/reset cycles. This is because the probability of generating new CFs in different locations is much less favorable than the CF rejuvenation during the successive set cycles. According to the previous results, the evolution of the geometry of the CF from the LRS to the HRS is schematically depicted in Fig. 2.12 (e). Starting from a very wide CF in the LRS, the first stage of the reset process consists in the reduction of the width of the CF in its most constrictive part to a limit in which only one or few oxygen vacancy paths connect the electrodes. This stage is followed by the opening of a gap, i.e. re-oxidation of one or several vacancies in all the paths. Once a gap is opened, the finding of $N = 1$ for $G < G_0$ means that the most conductive path controls the HRS I-V. In this regime (HRS), the thickness of the gap of the most conductive single vacancy path determines the CF conductance in the HRS. In Fig. 2.12(e) we have

assumed that the gap is in the center of the CF because the reset of these structures is likely due to thermal-enhanced dissolution and the center is likely the point of maximum temperature[83].

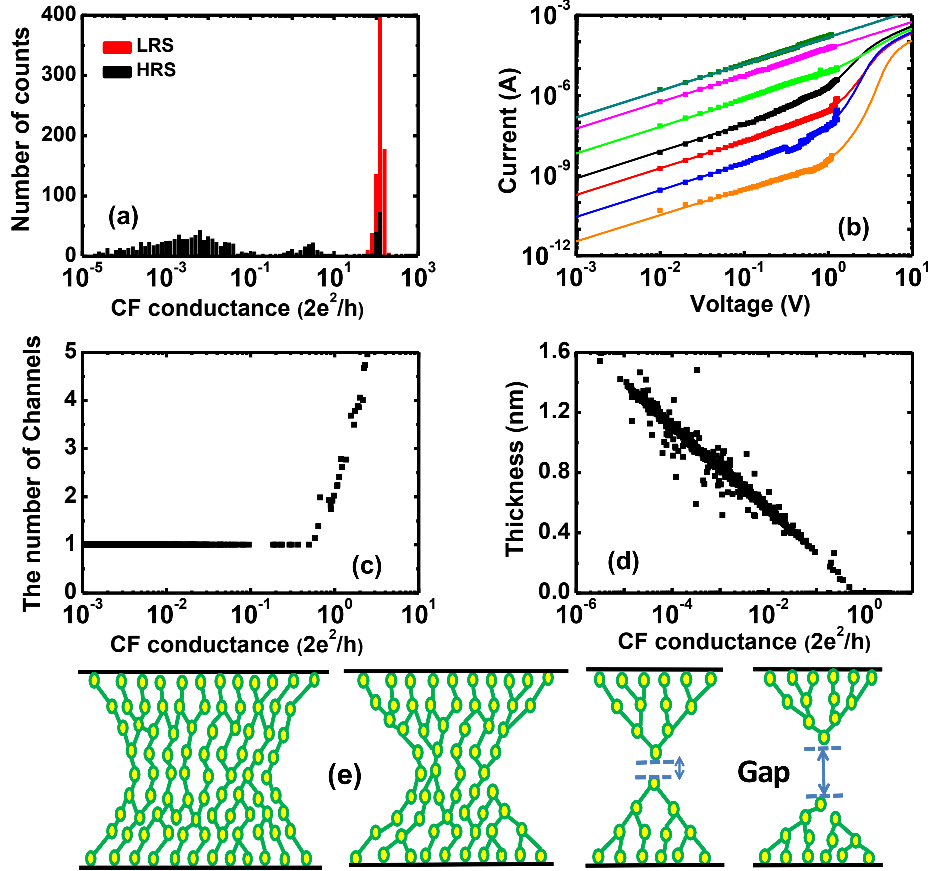


**Fig. 2.12** Nonpolar switching in Pt/$HfO_2$ /Pt structures. **(a)** Histogram of conductance @0.1V after set (red) and reset (black) cycles for 1250 successive set/reset cycles. **(b)** Examples of fitting of the I-V characteristics in the HRS. The CF conductance ranges from $G = 3.9e^{-5}G_0$ to $G{\sim}2G_0$. Extracted QPC model parameters**:** **(c)** number of conducting channels, i.e. number of single vacancy paths ($N$) versus CF conductance; and **(d)** thickness of the gap ($t_{gap}$) versus CF conductance. **(e)** Schematic representation of the CF structure evolution from the LRS to the HRS.

In the next two sections, the conductive properties of the CF in Pt/Ti/$HfO_2$ /Pt devices will be analyzed. The structures include a thin Ti layer between the top Pt electrode and the $HfO_2$ layer. The Ti film is believed to act as an oxygen extraction layer and to introduce a high density of oxygen vacancies in the $HfO_2$. The vacancy profile is thought to be rather asymmetric with a much higher concentration near the top interface. As a consequence, when a CF is created during forming, its shape is expected to be highly asymmetric, with the narrowest constriction near the bottom interface. In fact, due to this asymmetry, these structures only show reliable RS operation when negative bias is applied to the top electrode for reset. In other words, in agreement with previous works, RS is only possible by re-oxidation of the tip of the CF, i.e. when the bottom electrode is the reset anode[84]. Thus, these devices can be

operated under two different RS modes: unipolar (negative set/negative reset) and bipolar (positive set/negative reset), provided that reset is achieved under negative polarity. Therefore, the properties of the CF in Pt/Ti/$HfO_2$ /Pt devices, both under bipolar and unipolar RS operating are analyzed in the following sections.

### 2.4.2 Experimental results for Pt/Ti/$HfO_2$/Pt devices operated under bipolar conditions

Fig. 2.11(c) shows some typical examples of bipolar set/reset cycles and Fig. 2.13(a) shows the histograms of CF conductance in the LRS and the HRS. In the case of Pt/$HfO_2$/Pt structures, the I-V in the LRS is essentially linear with a high voltage sub-linear behavior likely related to temperature-dependent conductivity. However, in this bipolar switching experiment, the CF conductance in the LRS is smaller ($\sim 30G_0$) although the compliance current during forming and set was kept at the same value (1mA). In the HRS, the CF conductance is found to be in the range between $5e^{-2}G_0$ and $2G_0$, i.e. the bipolar reset is much less effective than the unipolar one in the Pt/$HfO_2$/Pt structures, and hence, the resistance ratio of the HRS and the LRS is much degraded, as usually found for bipolar RS. Other significant differences are that, as shown in Fig. 2.13(b), all the I-V curves after reset are significantly nonlinear in spite of the CF conductance being close to $G_0$. On the other hand, the non-linearity is roughly independent of the CF conductance (the curves appear as almost parallel in the log-log plot). The fitting of the I-V curves to the QPC model is excellent but in this case, the linear fit is not possible when $G > G_0$ nor it is possible to assume $N = 1$ for $G < G_0$, as explicitly shown in Fig. 2.13(c). In this particular case the extraction of the QPC parameters ($N$ and $t_{gap}$) was done under the assumption that $\beta = 1$. This value gives the best fitting results and is consistent with the strong asymmetry of the CF shape in structures which contain an oxygen extraction layer.

Fig. 2.13(d) shows the extracted gap thickness versus CF conductance in the HRS and the LRS, we can see the average gap thickness is 0.59nm in the HRS and 0.25nm in the LRS; this is to say, there are about two or three re-oxidized vacancies in the HRS and one re-oxidized vacancy in the LRS. As shown in Fig. 2.13(e), the average gap thickness per conducting mode is found to converge to zero for $G/N \sim G_0$, as required by the QPC model. The number of CF paths versus conductance is shown in Fig. 2.13(f), which is different from what was found in the case of Pt/$HfO_2$/Pt structures, many conduction paths are found to be active in the HRS but they show a gap with an average thickness corresponding to two or three vacancies. The average number of channels in the HRS is 134 and 192 in the LRS. According to the results of our analysis of properties by means of the reformulated QPC model, we can describe the evolution of the CF from the LRS to the HRS as shown in Fig. 2.13(g). Due to the asymmetry of the Pt/Ti/$HfO_2$/Pt structure, the CF is deduced to be conical with the tip contacting the bottom electrode being the active region during switching. In the LRS, the CF area is rather large (though smaller than in Pt/$HfO_2$/Pt structures) and there is one re-oxidized vacancy gap. In the HRS, and after a stabilization period of about 100 initial cycles, there is an average gap with the thickness of two or three vacancies and the CF conductance is modulated mainly by the area of the active CF tip.

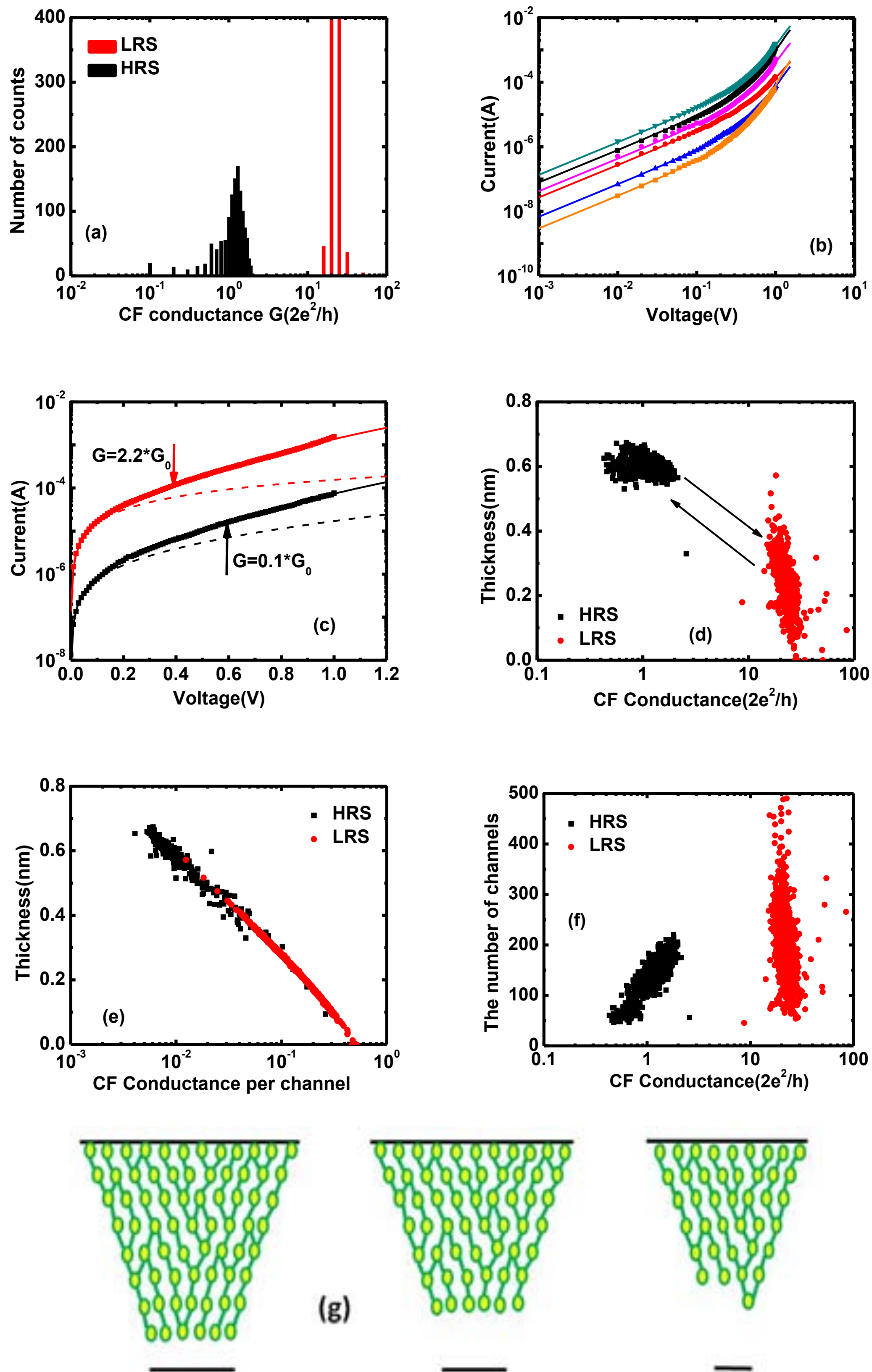


**Fig. 2.13** Application of the QPC model to Pt/Ti/$HfO_2$/Pt structures operated under bipolar RS conditions. **(a)** Distribution of CF conductance measured @0.1V in the HRS (black) and LRS (red) during bipolar cycling experiment. **(b)** Fitting of I(V) to the QPC model in the HRS. **(c)**

Demonstration that fitting with $N = 1$ (dashed black line) is not possible for low conductance CFs ($0.1G_0$) in the HRS nor it is possible to fit the I(V) assuming linear conduction for $G > G_0$ (red dashed line) in the LRS. **(d)** Statistics of extracted QPC model parameters extracted from the fitting of 1250 I-V curves after the reset RVS in bipolar RS modes: thickness of the gap versus CF conductance; and **(e)** gap thickness versus conductance per channel. **(f)** The number of conducting channels versus CF conductance. **(g)** Schematic representation of CF structure in bipolar experiments.

### 2.4.3 Experimental results for Pt/Ti/$HfO_2$/Pt devices operated under unipolar conditions

The experimental results of Pt/Ti/$HfO_2$/Pt devices in unipolar RS mode are different from bipolar RS mode. Fig. 2.11(d) shows the typical set/reset I-V curves in unipolar mode. Although the extraction of the QPC parameters ($N$ and $t_{gap}$) was done under the assumption that $\beta = 1$ and $\Phi = 1.16$ eV. The CF conductance in the LRS ($\sim 30G_0$) is similar to bipolar RS mode while in the HRS, the CF conductance is smaller than bipolar RS mode, which is found to be in the range between $10^{-2}G_0$ and $4G_0$, as shown in Fig. 2.14(a). That is to say, the unipolar RS mode is more effective than bipolar RS mode for Pt/Ti/$HfO_2$/Pt devices, but it is much less effective than Pt /$HfO_2$/Pt devices. Fig. 2.14(b) shows the excellent I-V fitting in the HRS using least square-estimation method. When the CF conductance is of the order of $G_0$ or higher, the I-V tends to be linear, consistent with the idea that one or several oxygen vacancy paths connect the two electrodes through extended quasi-one dimensional electron subbands. Fig. 2.14(c) to Fig. 2.14(e) shows the extracted QPC parameters versus CF conductance. The average gap thickness is about 0.09nm in the LRS and 0.356nm in the HRS and the average gap thickness per conducting mode is found to converge to zero for $G/N \sim G_0$, as required by the QPC model. The average number of paths is about 130 in the LRS and 5 in the HRS. Therefore, the number of conductance channels decreases and open a gap that is about two re-oxidized vacancies from the LRS to the HRS. Finally, Fig. 2.14(f) schematically shows the evolution of the microscopic structure of the CF in Pt/Ti/$HfO_2$/Pt devices when the evolution from the LRS to the HRS during unipolar RS mode. In the LRS, there are many conductive filaments and very small thickness gap between two electrodes. Then the CF is narrowing and opening about two re-oxidized vacancies gap in the HRS.

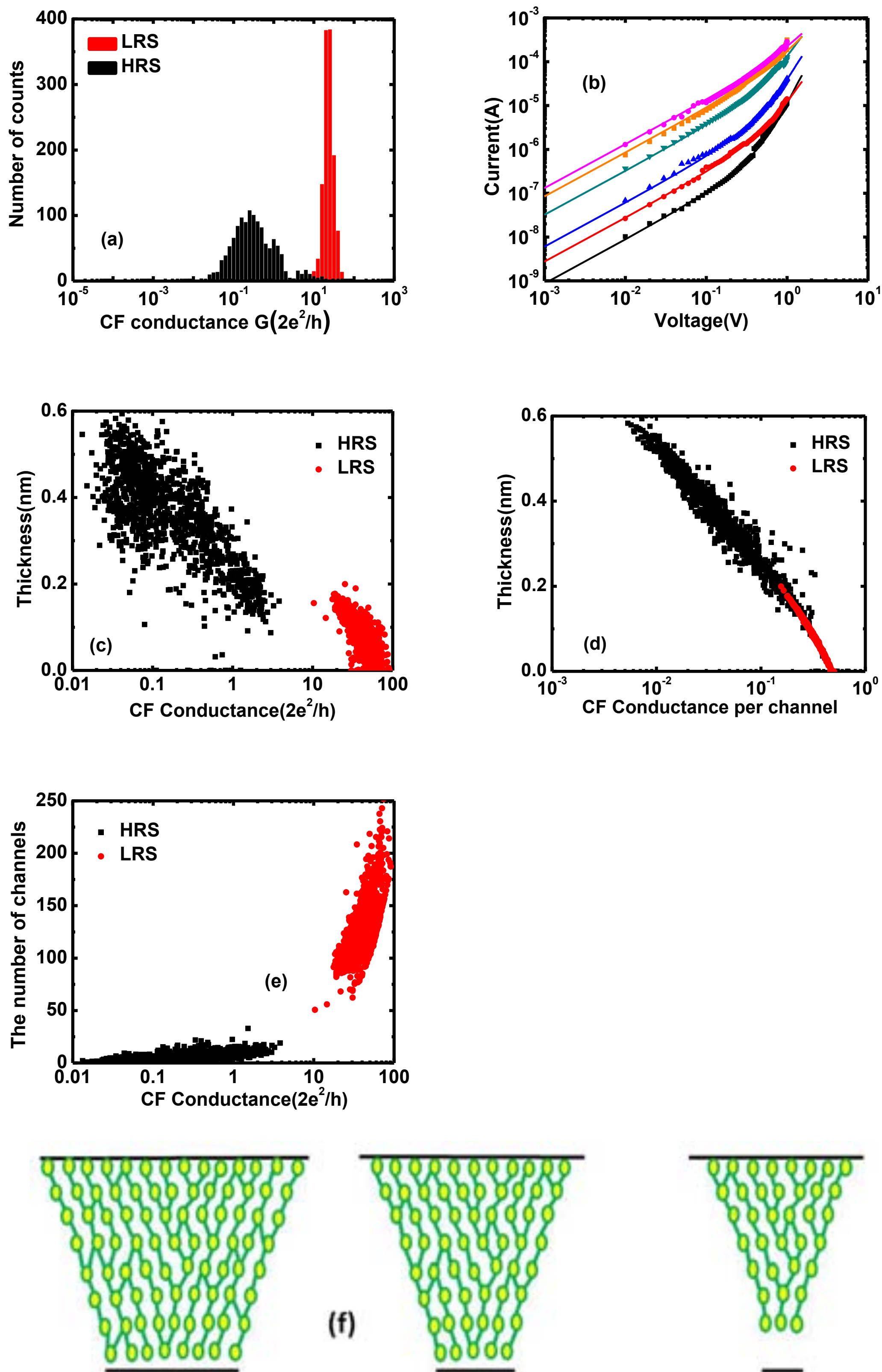


**Fig. 2.14** Application of the QPC model to Pt/Ti/$HfO_2$ /Pt structures operated under unipolar RS conditions**.** **(a)** Distribution of CF conductance measured @ 0.1V in the HRS (black) and LRS (red) during unipolar cycling experiment; **(b)** fitting of I (V) to the QPC model in the HRS; Statistics of extracted QPC model parameters extracted from the fitting of 1250 I-V curves after

the reset RVS in unipolar RS modes: **(c)** thickness of the gap versus CF conductance; and **(d)** gap thickness versus conductance per channel. **(e)** The number of conducting channels versus CF conductance; **(f)** the evolution of CF structure in unipolar experiments.

In this chapter, the QPC model has been applied to a thorough statistical study of resistance switching in RRAM devices. The fitting of I-V characteristic is excellent in both HRS and the LRS for two different structures in three RS modes. After reformulating the QPC model for CF conduction by coupling it to the results of ab-initio simulations of oxygen vacancy paths, we can obtain indirect information about the microscopic structure of the CF in both Pt/$HfO_2$/Pt and Pt/Ti/$HfO_2$/Pt devices. For Pt/$HfO_2$/Pt devices, the CF is symmetry where the most constrictive part is in the center of the CF. Starting from a very wide CF in the LRS, the width of the CF in its narrowest part reduces to a limit where only one or few oxygen vacancy paths connect the electrodes. This stage is followed by the opening of a gap that the thickness of the most conductive single vacancy path determines the CF conductance in the HRS. For Pt/Ti/$HfO_2$/Pt devices, the CF is highly asymmetry, with the narrowest constrictive part near the bottom of interface. The CF is deduced to be conical with the tip contacting the bottom electrode being the active region during switching. The Ti film is believed to act as an oxygen extraction layer and to introduce a high density of oxygen vacancies in the $HfO_2$. In the LRS, the CF area is rather large and there is one re-oxidized vacancy gap for bipolar RS mode, then the gap increases to two or three vacancies and the CF is narrower than the LRS. For unipolar RS mode, the number of paths in the HRS is much less than bipolar RS mode, this is to say, the unipolar RS mode is more effective than bipolar RS mode. The obtained results have revealed significant differences in the properties of the CF in these two types of devices. This is consistent with the expected differences in the concentration profile of oxygen vacancies due to the presence/absence of an oxygen extraction layer.

# Chapter 3

## RESET/SET Switching Statistics of RRAM

The device-to-device and cycle-to-cycle variability are problems which negatively affect the application of RRAM arrays and need to be improved by processing and/or operation algorithms [60]. The statistics of switching parameters of RRAM devices are considered as one of the critical factors to obtain low variability and high reliability for RRAM practical application. However, a detailed analysis of the RS distribution of the metal CF-type RRAM devices have not been given yet. The main goal of this chapter is the proposal of the general statistical approach and of physics-based analytical models to model the reset/set distributions in RRAM devices.

Departing from the cell-based percolation model of gate dielectric breakdown we propose an analytical model for the set and reset statistics which are based on the formation and disconnection of a conducting filament (CF) in RRAM devices. This model is composed of two basic elements: (i) a cell-based geometrical model to describe the dependence of the RS distribution on the defect generation in the CF, and (ii) a deterministic model for the set/reset dynamics to describe the relation of the defect generation with measurable variables such as the set/reset voltages and currents.

The first part of this chapter is dedicated to the cell-based percolation model for the dielectric breakdown. Afterwards, an analytical model for SET and RESET statistics in RRAM will be discussed in detail in second part, including two basic elements which are cell-based geometrical model and a deterministic model for the set/reset statistics. In the following parts of this chapter, the set and reset switching statistics experimental results for $HfO_2$-based RRAM devices are also shown. Moreover, the comparison of experimental results with theoretical models demonstrates feasibility of these models.

## 3.1 The cell-based percolation model for the dielectric breakdown

The dielectric breakdown (BD) refers to a rapid reduction in the resistance of an electrical insulator when the voltage applied across it exceeds the breakdown voltage, which corresponds to the loss of the dielectric properties of gate oxide. The BD has been studied in MOS devices since more than six decades and, in spite of this, there is no complete agreement about its physical origin. However, it is widely accepted that the oxide breakdown is the consequence of the degradation of its microstructure, which is related to the generation of defects during electrical stress or operation[85]. When the density of defects in the oxide reaches a critical value, a connection is established between the electrodes through a defect related conduction path, which leads to a sudden increase of the current[86-88]: this is the onset of the BD. Traditionally, in thick oxides, the generation of defects is evidenced by an increased electron and/or hole trapping which modifies the conduction during stress. In thinner films trapping is more difficult due to tunneling, and the generation of defects is revealed by their involvement in trap-assisted charge transport mechanisms which increase the current at low electric fields giving rise to the so-called stress-induced leakage current (SILC)[89]. The study of SILC can be used to evaluate the degradation of the oxide.

Gate oxides thinner than about 5nm show two different types of breakdowns which have been named as soft breakdown (SBD) and hard breakdown (HBD), respectively[90]. Both mechanisms correspond to an extremely local failure which is detected as a significant increase of the leakage current through the oxide[91-93]. The current after SBD is orders of magnitude smaller than that measured after HDB. Finally, gate oxides thinner than 2.5nm show a progressive increment of the current through the oxide until the HBD can be observed: the Progressive Breakdown (PBD), which corresponds to the same phenomenon of SBD and HBD, but at different time scales[94-96].

Fig. 3.1 represents the generation of defects in the oxide and the relation with the percolation model[97-99]. A vertical path of oxide has n=$T_{OX}/a_0$ cells, with $T_{OX}$ being the oxide thickness and $a_0$ being one cell thickness. During the electrical stress, defects are generated at random in the oxide bulk and a cell is defective if one or more defects have been generated in its volume. When all the cells in a vertical path are defective, this is called a percolation path and it is considered to trigger the breakdown of oxide. In this chapter, only straight vertical paths are considered. Although non-vertical paths have also been explicitly considered in the literature[100], it can be demonstrated that inclusion of these types of paths is fully equivalent to a change of the cell area σ. Therefore, the vertical path model is complete and does not involve any extra approximation to the general percolation approach. If the density of defects per unit of volume $N_t$ can been experimentally monitored, the average number of defects per cell can be calculated by $n_{DEF}=\sigma a_0 N_t$. Provided that the generation of defects is uniform across the oxide area and that there is no spatial or time correlation in the generation of successive defects, the Poisson model is adequate to describe their distribution. The probability of a cell being defective is then $\lambda = 1 - \exp(-n_{DEF})$ and the probability

of one particular column being a percolation path is $\lambda^n$.

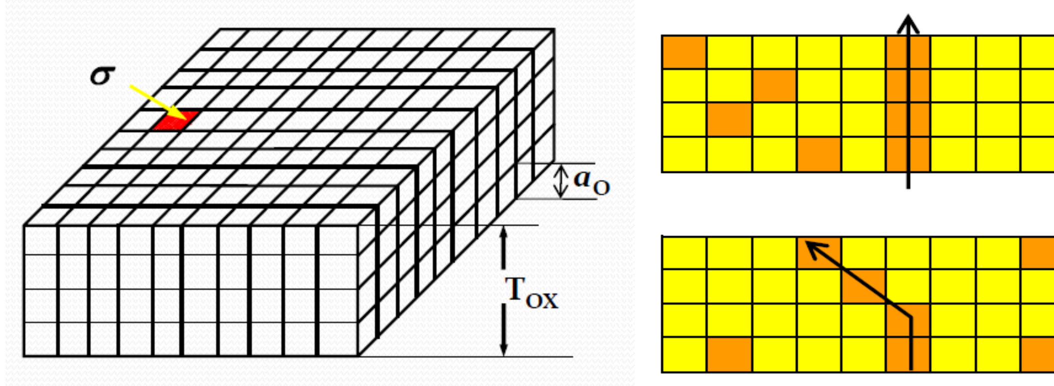


**Fig. 3.1** (Ref. 89) Schematic pictures show the oxide bulk and the generation of defects and breakdown triggering condition in cell-based percolation model.

Since the breakdown of oxide has a weakest-link character, the device failure cumulative distribution is given by

$$F_{BD} = 1 - (1 - \lambda^n)^N \quad (3\text{-}1)$$

And the so-called weibit is

$$W_{BD} \equiv \mathrm{Ln}\big(-\mathrm{Ln}(1 - F_{BD})\big)$$
$$= \mathrm{Ln}(-\mathrm{NLn}(1 - \lambda^n)) \quad (3\text{-}2)$$

Where $N$ is the number of vertical paths, $N = A_{ox}/\sigma$, with $A_{ox}$ being the oxide area. The equation (3-2) can be further simplified using $Ln(1 - \lambda^n) \approx -\lambda^n$ when the density of defects per cell at BD is very small $n_{DEF} \ll 1$, it follows that $\lambda \approx n_{DEF}$, $\lambda \ll 1$. Under this assumption, the Weibit becomes

$$W_{BD} = Ln(N) + nLn(n_{DEF}) \quad (3\text{-}3)$$

The Weibull distribution is defined as

$$F(x) = 1 - \exp\big[-(x/x_{63\%})^{\beta}\big], \quad (3\text{-}4)$$

or

$$W(x) = \beta \mathrm{Ln}(x/x_{63\%}). \quad (3\text{-}5)$$

and it is described by two parameters, the scale factor $x_{63\%}$, which is the value of the statistical variable at $F \approx 0.63$, and the shape factor or Weibull slope $\beta$, which measures the statistical dispersion. Thus, the BD distribution is a Weibull distribution with shape factor equals to the number of cells in a defective vertical path (the number of defects per column, n). Eq. (3-1) and Eq. (3-3) establish a direct link between defect generation and the BD statistics. However, if we want to compare with the experimental results, we still need to relate the density of defects to measurable breakdown variables appropriate to the type of stress used in the experiments.

The time to breakdown ($t_{BD}$) and the charge injected to breakdown ($q_{BD}$) are the natural variables for the constant voltage stress (CVS) or constant current stress (CCS). In the case of ramped voltage stress (RVS), the breakdown voltage ($v_{BD}$) is the measurable variable. To establish the relation between the density of defects $n_{DEF}$ and the BD measurable variable, we need a deterministic model for the dynamics of defect generation, which requires a lot of experimental characterization and a

physics-based picture for the defect generation process. This deterministic model provides the time evolution of the density of defects during stress as a function of the relevant stress parameters (oxide voltage or oxide field, stress temperature, ramp rate in the case of RVS, etc.).

In the case of CVS, there is experimental evidence showing that the time evolution of the density of defects follows a power law of the type:

$$n_{\mathrm{DEF}} = \left(\frac{t}{\tau_{\mathrm{TBD}}}\right)^{\alpha_{\mathrm{BD}}} \quad (3\text{-}6)$$

with the exponent $\alpha_{\mathrm{BD}}$ being essentially a constant and the scale factor $\tau_{\mathrm{TBD}}$ being strongly dependent on the stress voltage [101] and temperature[102]. This relation is valid for CVS. Combination Eq. (3-3) and Eq. (3-6) provides a complete analytical model for the breakdown statistics,

$$W_{\mathrm{BD}} = \mathrm{Ln}\left(\frac{A_{\mathrm{OX}}}{\sigma}\right) + \alpha_{\mathrm{BD}}\frac{T_{\mathrm{OX}}}{a_0}\mathrm{Ln}\left(\frac{t}{\tau_{\mathrm{TBD}}}\right) \quad (3\text{-}7)$$

Which has two geometrical parameters (σ and $a_0$) and two parameters related to the deterministic model of defect generation ($\alpha_{\mathrm{BD}}$ and $\tau_{\mathrm{TBD}}$). Other types of stresses would require other particular equations for the evolution of $n_{DEF}$ during stress. Recently, the RVS was considered to deal with the BD statistics of nanolaminated dielectrics and a relation between CVS and RVS was established[103].

Fig. 3.2 shows the experimental results using this cell-based percolation model to obtain the relationship between oxide thickness and the Weibull slope[104, 105].

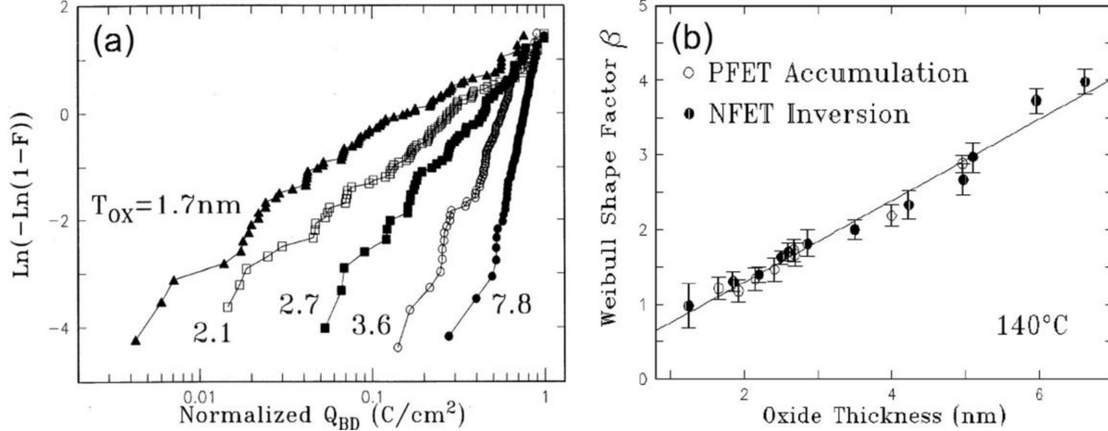


**Fig. 3.2** (a) Cumulative distribution of charge to breakdown as a function of oxide thickness showing the widening of the distributions for thin oxides (Ref. 104). (b) Linear scaling of the Weibull slope as a function of oxide thickness (Ref. 105).

The cell-based percolation model for the oxide dielectric breakdown statistics has been introduced in this section. The BD depends on the oxide area according to its weakest-link property, while CF-based RS is usually found to be area-independent, due to the RS behavior usually occurring at a single CF. In the next section, a single CF is assumed for the description of the switching statistics in RRAM devices. Inspired by the cell-based percolation model of oxide BD, a general framework to deal with the statistics of CF-based resistive switching will be developed, which is

made up of two elements: (i) cell-based geometrical model to describe the dependence of the resistive switching distribution on the defect generation in CF (ii) a deterministic model for the set/reset dynamics to describe the relation of the defect generation with measurable variables such as the set/reset voltages and currents.

## 3.2 Cell-based Geometrical Model of CF-based RRAM device

The cell-based percolation model for oxide breakdown of thin gate insulators[99, 106, and 107] can be easily adapted to model the set and reset statistics of filament-based RRAM. In the case of set transition, defects somehow accumulate in the CF and finally trigger the current jump. In the reset transition, the out-diffusion of the conductive defects from the CF cells finally causes the complete path distribution and the transition to the HRS.

The cell-based geometrical model of CF in reset transition as shown in Fig.3.3(a), which is 2D for convenience, but our model is actually 3D. The most constrictive part or “bottleneck” of CF in LRS determines the reset transition. The number of slices in most constrictive part of CF is N and each one has n cells. The reset transition occurs at least all the cells of one slice have diffused out of the CF (i.e. an oxygen vacancy in CF recombined with an oxygen ion).

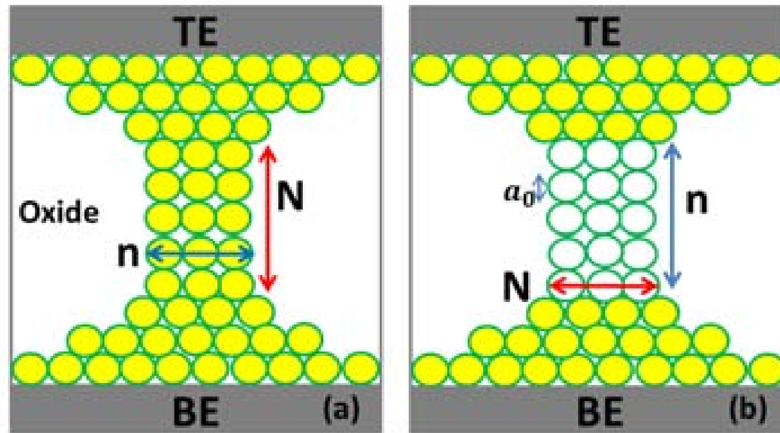


**Fig. 3.3** Schematic pictures of cell-based reset (a) and set (b) model. The most constrictive part of CF in LRS (a) and the gap of CF in HRS (b) determine the reset and set transition, respectively.

For simplicity, we define $\lambda$ as the probability of out-diffusion of a cell and all the cells in the CF are considered have the same probability. The reset transition is assumed to occur when all the cells of a slice or more slices have diffused out of the CF, thus leaving a gap. Therefore, the cumulative probability of reset of each slice is given by:

$$P_{\text{SLICE}} = \lambda^n \quad (3\text{-}8)$$

and the survival probability of a CF is given by the survival of the whole set of $N$ slices :

$$1 - F_{\text{RESET}} = (1 - \lambda^n)^N \quad (3\text{-}9)$$

And $F_{\text{RESET}}$ is the reset probability. So the Weibull,$W_{RESET} \equiv \text{Ln}[-\text{Ln}(1-F_{\text{RESET}})]$ is given by

$$W_{\text{RESET}} = \text{Ln}(N) + \text{Ln}[-\text{Ln}(1-\lambda^n)] \quad (3\text{-}10)$$

Considering $Ln(1-\lambda^n) \approx -\lambda^n$, an approximation which is valid when the value of $\lambda$ is very small, so the Weibull distribution for reset transition is

$$W_{\text{RESET}} \cong \text{Ln}(N) + n\,\text{Ln}(\lambda) \quad (3\text{-}11)$$

Comparing with the equation (3-5) of Weibull distribution, in reset transition, the shape factor equals to n and scale factor is dependent on N.

The cell-cased geometrical model of CF in set transition as shown in Fig. 3.3(b), there is a gap existing in CF before set transition occurs. This gap is comprised of N columns with each column having n cells. The set transition occurs at least all the cells of one column have been defected. Similarly, we define $\lambda$ as the probability of a cell being defective and the cumulative probability of a column being defective is given by:

$$P_{\text{col}} = \lambda^n \quad (3\text{-}12)$$

The survival probability of the gap can be calculated:

$$1 - F_{\text{SET}} = (1-\lambda^n)^N \quad (3\text{-}13)$$

Where $F_{\text{SET}}$ is the SET probability, which is at least one of the $N$ columns having all the $n$ cells defective. When $\lambda \ll 1$, the Weibull of the SET distribution can be approximated as:

$$W_{\text{SET}} \equiv \text{Ln}[-\text{Ln}(1-F_{\text{SET}})] \cong \text{Ln}(N) + n\,\text{Ln}(\lambda) \quad (3\text{-}14)$$

The shape factor is equal to $n$ and the scale factor depends on $N$. The dependence on $n$ is a key point of the model since $N$ is assumed to play a secondary role and to remain essentially constant during cycling.

Eq. (3-11) and Eq. (3-14) are the Weibull distribution for reset and set statistics in the case of cell-based geometrical model of CF, respectively.

## 3.3 Deterministic model for CF-based RRAM device

In section 3.2, we have obtained the relationship between the Weibull distribution for reset statistics and the probability of out-diffusion of a cell $\lambda$ (set statistics and the probability of a cell being defective $\lambda$). Now it is necessary to relate the probability $\lambda$ to the measurable variables such as reset voltage, reset current, set voltage and set current.

### 3.3.1 Deterministic model for the reset dynamics

Assuming a Poisson distribution of defects in the cells, $\lambda$ can be related to the average number of defects per cell, $n_{DEF}$ as:

$$\lambda = 1 - exp(-n_{\text{DEF}}) \quad (3\text{-}15)$$

When $n_{\text{DEF}} \ll 1$, $\lambda \approx n_{\text{DEF}}$. By analogy to BD, the defect generation under constant voltage can be modeled by a very simple power law[97-99], analogous to that of Eq. (3-6):

$$n_{\text{DEF}} = \left(\frac{t}{\tau_T}\right)^{\alpha} \quad (3\text{-}16)$$

Where $\tau_T$ is the characteristic time for defect generation which is expected to depend strongly on the applied voltage, and $\alpha$ is a voltage-independent exponent[99]. In the

case of a ramp voltage stress ($V$(t) =$R$t, $R$ being the ramp rate) , the average number of defects per cell at the time when reset occurs is given by:

$$n_{\text{DEF}}(t_{RESET}) \cong \left(\int_0^{t_{\text{RESET}}} \frac{1}{\tau_T(t)} dt\right)^{\alpha} \quad \text{(3-17)}$$

In unipolar valence change mechanism (VCM) device, the reset is controlled by a temperature-activated out diffusion of defects[89]. Assuming an Arrhenius law for the diffusion coefficient:

$$D = D_0 exp\left(-\frac{E_a}{K_B T}\right) \quad \text{(3-18)}$$

with

$$T = T_0 + R_{TH}/R_{ON}\, V^2 \quad \text{(3-19)}$$

Where $D$ is the diffusion coefficient, $E_a$ is the activation energy for diffusion, $K_B$ is the Boltzmann constant, $T$ is the temperature in the CF and $T_0$ is sample temperature with no applied bias, $R_{ON}$ is the CF resistance in LRS and $R_{TH}$ is the equivalent thermal resistance of CF[83]. Taking into account equation (3-18) and (3-19), the relation between the characteristic diffusion time $\tau_T$ and $V$reset can be obtained:

$$\tau_T \sim \tau_0\, exp\left[\frac{E_a}{K_B(T_0+\eta V^2)}\right] \quad \text{(3-20)}$$

Where $\eta \equiv R_{\text{TH}}/R_{\text{ON}}$. Substituting equation (3-20) into (3-17), we can get

$$n_{DEF} = \left\{\int_0^{t_{\text{RESET}}} \frac{1}{\tau_0} exp\left[-\frac{E_a}{K_B(T_0+\eta V^2)}\right]\right\}^{\alpha} \quad \text{(3-21)}$$

If we directly try to use formula (3-21), it is difficult to obtain analytical results for $n_{\text{DEF}}$, so it is convenient to make a power law approximation[89] to Eq. (3-20) so that:

$$\tau_T \approx \tau_{T0} V^{-m} \quad \text{(3-22)}$$

By combining (3-17) and (3-22), we can obtain:

$$n_{\text{DEF}} = \left(\frac{V_{\text{RESET}}}{V_0}\right)^{(m+1)\alpha} \quad \text{(3-23)}$$

With $V_0 = [(m+1)R\, \tau_{T0}]^{\frac{1}{(m+1)}}$. Therefore, we can get the density of defects as a function of the current as:

$$n_{\text{DEF}} = \left(\frac{I_{\text{RESET}}}{I_0}\right)^{(m+1)\alpha} \quad \text{(3-24)}$$

With $I_0 = \frac{1}{R_{ON}}[(m+1)R\, \tau_{T0}]^{\frac{1}{(m+1)}} = \frac{1}{R_{ON}} V_0$

The Eq. (3-23) and Eq. (3-24) provide a simple analytical link between the measurable switching variables, i.e. $V_{\text{RESET}}$ and $I_{\text{RESET}}$, and the density of generated defects, $n_{\text{DEF}}$, required for the calculations of the switching statistics.

By combining (3-5), (3-11) and (3-23), (3-24), we can get the final expression of the complete analytical model of reset statistics. The reset deterministic model predicts a Weibull shape for the reset voltage and current distributions. In the most reasonable case of $N = 1$, the model predicts a constant $V_{\text{RESET63\%}}$while $\beta_{V_{\text{RESET}}}$, $\beta_{I_{\text{RESET}}}$ and $I_{\text{RESET63\%}}$ are predicted to be proportional to $n$ (i.e. proportional to $1/R_{\text{ON}}$) as expressed by the following equations:

$$\beta_{V_{\text{RESET}}} = \alpha n(m+1), \quad \text{(3-25)}$$

$$\beta_{I_{\text{RESET}}} = \alpha n(m+1), \quad \text{(3-26)}$$

$$V_{\text{RESET63\%}} = [(m+1)R\tau_{T0}]^{\frac{1}{m+1}} \quad \text{(3-27)}$$

$$I_{\text{RESET63\%}} = \frac{1}{R_{\text{ON}}} V_{\text{RESET63\%}} \quad \text{(3-28)}$$

where $R$ is the voltage ramp rate.

### 3.3.2 Deterministic model for the set dynamics

Similar to the analysis of the reset dynamics, the evolution of $\lambda$ up to the set switching time can be written as:

$$n_{\mathrm{DEF}}(t_{SET}) \cong \left(\int_0^{t_{\mathrm{SET}}} \frac{1}{\tau_T(t)} dt\right)^{\alpha} \tag{3-29}$$

where $\tau_T(t)$ is strongly dependent on the oxide field with a power law [103]:

$$\tau_T(t) = \gamma_{T0} \left(\frac{V(t)}{t_{\mathrm{gap}}}\right)^{-m} \tag{3-30}$$

After straightforward calculations involving (3-29) and (3-30) and substitution into (3-14), a Weibull model for the distribution of set voltage is obtained:

$$W(V_{\mathrm{SET}}) = \mathrm{Ln}(N) + (m+1)\alpha n \,\mathrm{Ln}\left\{\frac{V_{\mathrm{SET}}}{\left[(m+1)R\gamma_{T0}{t_{\mathrm{gap}}}^{m}\right]^{\frac{1}{m+1}}}\right\} \tag{3-31}$$

with Weibull slope and scale factor given by:

$$\beta_{V_{\mathrm{SET}}} = \left(\alpha \frac{m+1}{a_0}\right) t_{\mathrm{gap}} \tag{3-32}$$

$$V_{\mathrm{SET63\%}} \approx const \cdot R^{\frac{1}{m+1}} \left(t_{\mathrm{gap}}\right)^{\frac{m}{m+1}}, \tag{3-33}$$

Thus, $\beta_{V_{\mathrm{SET}}}$ is proportional to $t_{\mathrm{gap}}$ and $V_{\mathrm{SET63\%}}$ is also roughly proportional to $t_{\mathrm{gap}}$ if $m$ is large ($m \approx 27$ has been reported for the voltage acceleration of the time-to-set distribution in Ni/$HfO_2$/Si devices [108, 109]).

The parameter $t_{\mathrm{gap}}$ is not directly accessible to the electrical measurements but it is directly related to the resistance of the CF in the OFF-state. We have used the QPC model to relate the CF $I-V$ characteristic to a parabolic potential barrier in the OFF-state. For high enough barriers and small applied voltages, the QPC model gives the following $I-V$ relation:

$$I \cong G_0 N_{\mathrm{ch}} \exp(-\alpha\Phi)\, V \tag{3-34}$$

where $N_{\mathrm{ch}}$ is the number of opened conducting channels, $\Phi$ is the height of the tunneling barrier in the conducting channel, and $\alpha$ is related to the inverse of the curvature of the barrier. Thus, the initial resistance in the HRS is given by

$$R_{\mathrm{OFF}} \cong \exp(\alpha\Phi)/(G_0 N_{\mathrm{ch}}). \tag{3-35}$$

$t_{\mathrm{gap}}$ can be calculated from the QPC model parameters[74] as

$$t_{\mathrm{gap}} = \frac{\hbar\alpha}{\pi}\sqrt{\frac{2\Phi}{m_0}} \tag{3-36}$$

where $\hbar$ is the reduced Plank constant, and $m_0$ is the electron mass. Thus, $t_{\mathrm{gap}}$ can be expressed by:

$$t_{\mathrm{gap}} = \frac{\hbar}{\pi}\sqrt{\frac{2}{m_0\Phi}}\,\mathrm{Ln}(G_0 N_{\mathrm{ch}} R_{\mathrm{OFF}}). \tag{3-37}$$

Using first-principle calculation method, the value of $\Phi \sim 1.16$ eV is determined. Consequently, according to (3-32), (3-33) and (3-37), our compact analytical model for the set switching statistics predicts that both $\beta_{V_{\mathrm{SET}}}$ and $V_{\mathrm{SET63\%}}$ have a linear relation with $\mathrm{Ln}(R_{\mathrm{OFF}})$. In next section, the experimental results for reset and set

statistics of Pt/$HfO_2$/Pt devices will be shown, to be in nice agreement with the proposed models.

## 3.4 Experimental results for reset and set statistics

In this section, the experimental results for reset and set statistics are shown, mainly for Pt/$HfO_2$/Pt devices. Fig. 3.4 shows the $I-V$ curves of several typical set and reset switching cycles of a Pt/$HfO_2$/Pt device operated by DC voltage sweep.

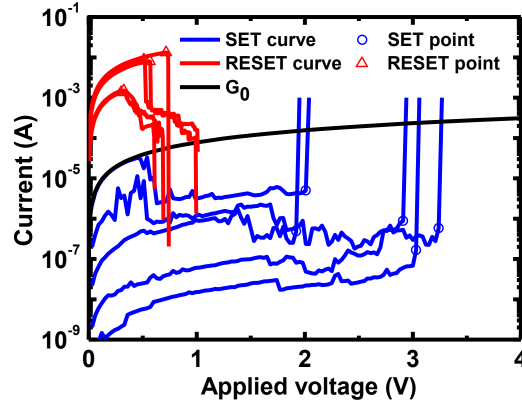


**Fig. 3.4** $I-V$ curves of set (blue lines) and reset switching (red lines) of Pt/$HfO_2$/Pt device. set and reset points are defined as those at which the partially broken filament just begin to grow and those at the maximum of the current in reset curves, respectively.

### 3.4.1 Experimental reset statistics

The raw voltage and current data were corrected by the series resistance $R_S$, which was estimated to be $R_S \sim 28\ \Omega$ by adding the resistance of the experimental set up (~18 Ω) to the Maxwell resistance, estimated to be ~10 Ω for a CF with a diameter of ~10 nm. After this correction, the reset voltage $V_{RESET}$ appears to be rather independent on $R_{ON}$ (Fig. 3.5(a)) and the reset current $I_{RESET}$ (Fig. 3.5(b)) is inversely proportional to $R_{ON}$. This behavior is completely analogous to what previously reported for NiO-based RRAM devices[89, 110] and it is compatible with the predictions of the thermal dissolution model of reset[67, 83].

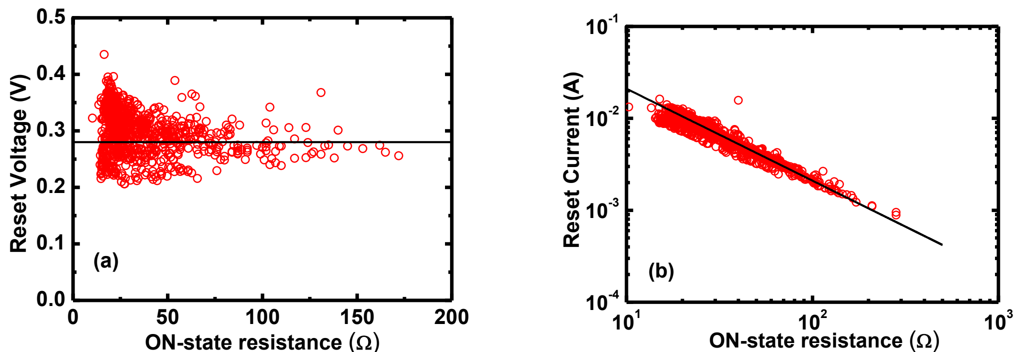


**Fig. 3.5** (a) The scatter plots of the measured 1250 cycles of Pt/$HfO_2$/Pt devices reset voltage

versus $R_{ON}$ and (b) The scatter plots of reset current versus $R_{ON}$ after data correction by the series resistance Rs=28 Ω .

In order to obtain the $V_{RESET}$ and $I_{RESET}$ statistics distribution in different ON-state resistance ($R_{ON}$) ranges, we use a data screening method for $R_{ON}$. Fig. 3.6(a) and 3.6(b) show the global cumulative distribution of $V_{RESET}$ and $I_{RESET}$ together with the screened distributions for the different $R_{ON}$ ranges. In both cases, the distributions have been displayed in the Weibull plot. Since the screened cumulative distributions are around straight lines in these plots, we conclude that they are compatible with Weibull distributions. If we compare the global distributions of $V_{RESET}$ and $I_{RESET}$ with the screened distributions, we find that the shape of the global distribution has nothing to do with the intrinsic dispersion of the reset results. We have checked that whether the screened distributions are combined with adequate statistical weights according to the number of samples in each resistance range, the original global cumulative distributions of $V_{RESET}$ and $I_{RESET}$ are nicely reproduced. This confirms the consistency of our screening method. In particular, the change of slope in the global $I_{RESET}$ distribution is perfectly reproduced, thus emphasizing that the shape of this global distribution is fully controlled by the distribution of $R_{ON}$. In fact, the change of slope is only related to the fact that the probability of finding $R_{ON}$ within the two lowest resistance ranges (i.e. between 15 W and 25 W) is much higher than for higher $R_{ON}$ values. According to these results, we can conclude that the shape of the global distributions of $V_{RESET}$ and $I_{RESET}$ do not provide useful insight about the intrinsic statistics of the reset process unless we get rid of the variations of $R_{ON}$.

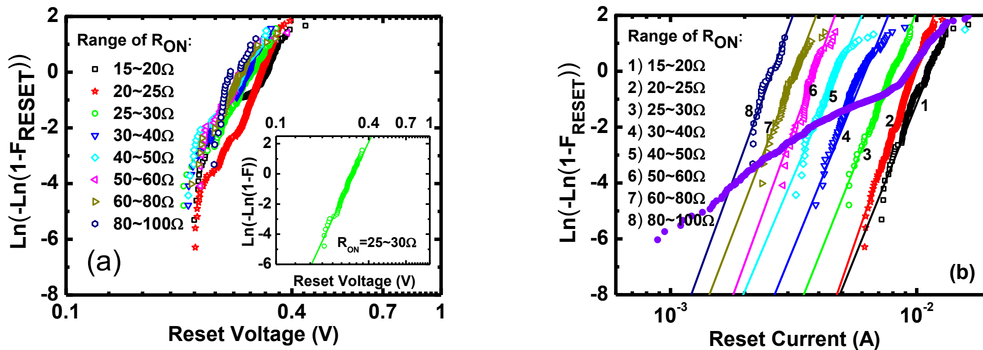


**Fig. 3.6** Experimental distributions (symbols) of Pt/$HfO_2$/Pt device and fitting to Weibull distributions (lines) of $V_{RESET}$ (a) and $I_{RESET}$ (b) as a function of $R_{ON}$. The extreme $R_{ON}$ ranges ($R_{ON}$ < 15 W and $R_{ON}$ > 100 W) are not included in these plots because of the limited number of points which yield distorted distributions. The purple dots show the global distribution of $I_{RESET}$ of all the 1250 cycles in Fig. 3.6 (b).

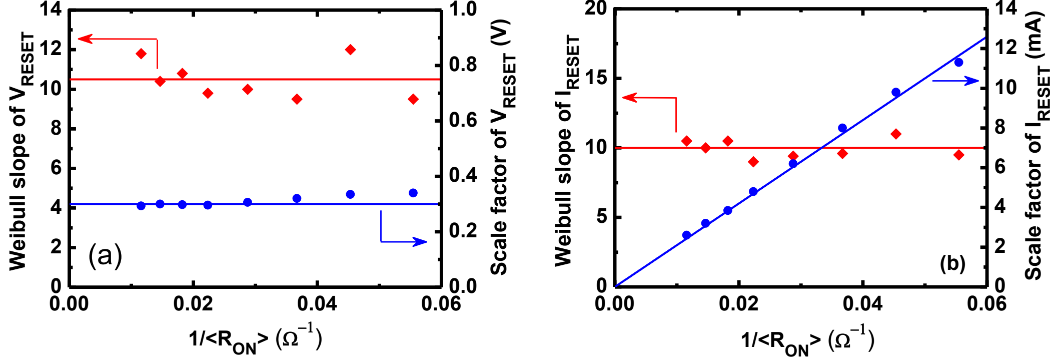


**Fig. 3.7** $R_{ON}$ dependence of the shape and scale factors of the $V_{RESET}$ (a) and $I_{RESET}$ (b) distributions of Pt/$HfO_2$/Pt device. The straight lines show the fitting results. $<R_{ON}>$ is the average of $R_{ON}$ in each screening range. $\beta_V$, $\beta_I$ and $V_{RESET63\%}$ are roughly constant, while $I_{RESET63\%}$ is proportional to $1/R_{ON}$.

Fig. 3.7 shows weibull parameters extracted from the $R_{ON}$ screening method as a function of $1/R_{ON}$. $V_{RESET63\%}$ is constant and $I_{RESET63\%}$is proportional to $1/R_{ON}$, which is in good accordance with the model for the reset statistics. However, $\beta_{V_{RESET}}$ and $\beta_{I_{RESET}}$ remain independent of $R_{ON}$, which is in clear contrast with our model prediction. This difference can be understood by discussing the meaning of reset point and looking at the details of what happens before the reset point. If there is no degradation of the CF before the reset point, then the reset event should be regarded as representing the initial step of the CF dissolution, i.e. the out-diffusion of the first conductive defect from the CF bottleneck. In this case, the result reported for Pt/$HfO_2$/Pt (i.e. $\beta_{V_{RESET}}$and $\beta_{I_{RESET}}$being independent of $R_{ON}$) would be consistent with our theoretical cell-based deterministic model for the reset dynamics.

In other words, our observations suggest that little or no structural change occurs in the $HfO_2$ device before the reset point, while significant degradation of the CF occurs in Pt/NiO/W devices[89] before the reset point. To explore the degradation occurring in the CF prior to the reset point, we designed a methodology based on calculating the maximum CF temperature by means of two different procedures[89]. First, we consider a linear temperature dependence of the CF typical of metallic behavior[111], i.e.

$$R_{CF}(T_{MAX1}) = R_0[1 + \gamma\alpha(T_{MAX1} - T_0)], \tag{3-38}$$

where $R_0$ is the CF resistance at ambient temperature $T_0$, $\gamma$ is a geometrical parameter ($\gamma$=2/3 for a cylindrical CF) and $\alpha$ is the experimental resistance temperature coefficient. Applying Eq. (3-38) to the experimental $I-V$ data, we can get the “experimental” $T_{MAX1}$ as a function of the applied voltage. On the other hand, we can also calculate the evolution of the maximum temperature as a function of the applied voltage from the heat dissipation equation[83], i.e.

$$T_{\mathrm{MAX2}} = T_0 + \frac{R_{\mathrm{TH}}}{R_{\mathrm{CF}}} V^2, \qquad (3\text{-}39)$$

where the $R_{\mathrm{TH}}/R_{\mathrm{CF}}$ ratio is assumed to be given by the Wiedemann-Franz law, i.e.

$$\frac{R_{\mathrm{TH}}}{R_{\mathrm{CF}}} = \frac{1}{8\zeta L T_{\mathrm{MAX2}}} \qquad (3\text{-}40)$$

with $L$=2.45×10$^{-8}$ WΩ/K$^2$ being the Lorentz number and $\zeta$ a fitting parameter which allows us to trim the thermal resistance so as to ensure $T_{\mathrm{MAX1}}$=$T_{\mathrm{MAX2}}$ at low voltages, where all the conductance change is due to temperature effects. Combining Eqs. (3-39) and (3-40), we can get a "theoretical" $T_{\mathrm{MAX2}}$. Divergence of both temperatures indicates that the CF suffers structural degradation. Fig. 3.8 shows very different behavior for NiO and $HfO_2$ structures. In the case of NiO, we concluded that significant degradation occurs before the reset point because these two temperatures diverge well before the maximum of the reset current[110]. While in our $HfO_2$-based devices, the results are quite different since, as shown in Fig. 3.8(b), the experimental and theoretical CF temperature curves nearly coincide before the reset point ($V_{\mathrm{app,RESET}}$=0.3 V, which corresponds to the maximum current). This means that, contrary to what reported for NiO-based structures[89], in case of the present $HfO_2$-based devices, the reset point nearly coincides with the starting point of the CF dissolution and the CF suffers little structural degradation before reset, which explains the different behavior of $\beta_{V_{\mathrm{RESET}}}$ and $\beta_{I_{\mathrm{RESET}}}$ independent of $R_{\mathrm{ON}}$.

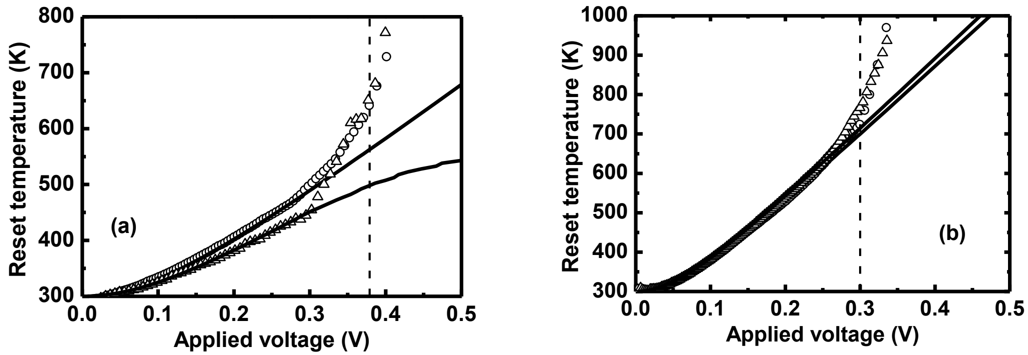


Fig. 3.8 Evolution of the experimental (dots) and theoretical reset temperature (lines) of two reset cycles in NiO (a) and $HfO_2$ (b) devices. The vertical dashed lines indicate the reset voltage (0.38V in (a) and 0.3V in (b)) corresponding to the maximum current. In (a) a sudden departure of the experimental $T_{\mathrm{MAX}}$ curve from the theoretical one occurs at about 0.3V, indicating CF degradation occurs before the reset point in NiO device. In (b) two types of curves nearly coincide before the reset point, so the reset point nearly coincides with the starting point of the CF dissolution in $HfO_2$ device.

The experimental results for reset voltage and current statistics of Pt/$HfO_2$/Pt devices have been shown in this section. $V_{\mathrm{RESET63\%}}$ is constant and $I_{\mathrm{RESET63\%}}$is proportional to $1/R_{\mathrm{ON}}$, which is in good accordance with the model for the reset statistics. $\beta_{V_{\mathrm{RESET}}}$ and $\beta_{I_{\mathrm{RESET}}}$ remain independent of $R_{\mathrm{ON}}$, which means the reset point nearly coincides with the starting point of the CF dissolution and the CF suffers

little structural degradation before reset. In next section, the experimental set voltage statistics of Pt/$HfO_2$/Pt devices will be reported.

### 3.4.2 Experimental set statistics

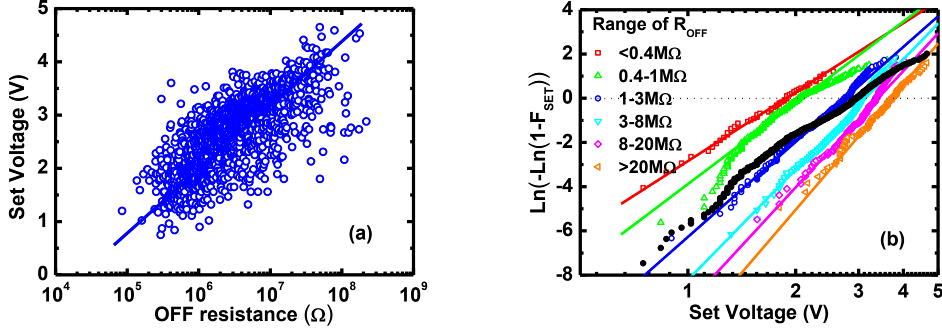


**Fig. 3.9** (a) Experimental scatter plots of $V_{\mathrm{SET}}$ versus $R_{\mathrm{OFF}}$ for 1750 cycles of Pt/$HfO_2$/Pt device. The spread of $V_{\mathrm{SET}}$ is comparatively wide but $V_{\mathrm{SET}}$ slightly increases with $R_{\mathrm{OFF}}$. (b) Experimental distribution (dots) and the fitting results (lines) of $V_{\mathrm{SET}}$ as a function of $R_{\mathrm{OFF}}$ in $HfO_2$ device. The black solid circles show the global distribution of $V_{\mathrm{SET}}$.

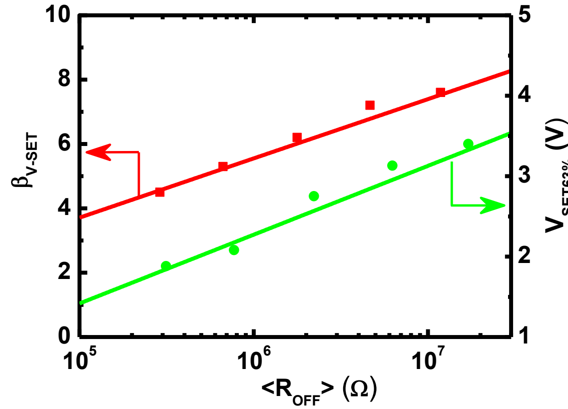


**Fig. 3.10** The shape (red points) and scale factor (green points) of the $V_{\mathrm{SET}}$ distribution versus $\langle R_{\mathrm{OFF}}\rangle$ in $HfO_2$ device. Both the shape and scale factor increase logarithmically with $R_{\mathrm{OFF}}$.

Fig. 3.9 (a) shows the experimental scatter plot of $V_{\mathrm{SET}}$ as a function of $R_{\mathrm{OFF}}$ for 1750 cycles of Pt/$HfO_2$/Pt device. It is clearly seen that $V_{\mathrm{SET}}$ increases with $R_{\mathrm{OFF}}$. Since $R_{\mathrm{OFF}}$ is widely distributed, it has a strong influence on the global distribution of $V_{\mathrm{SET}}$. Thus, we need to use a "resistance screening" method to get partially rid of the $R_{\mathrm{OFF}}$variations so as to study the “intrinsic” $V_{\mathrm{SET}}$ distribution. In Fig. 3.9(b), we decomposed the $V_{\mathrm{SET}}$ data into six different $R_{\mathrm{OFF}}$ ranges to study the distribution of $V_{\mathrm{SET}}$ as a function of $R_{\mathrm{OFF}}$. We can find that the global $V_{\mathrm{SET}}$ distributions are strongly linked to the $R_{\mathrm{OFF}}$ distribution. As shown in Fig. 3.10, both shape factor (Weibull slope) $\beta_{V_{\mathrm{SET}}}$and scale factor $V_{\mathrm{SET63\%}}$ of $V_{\mathrm{SET}}$ increase logarithmically with $R_{\mathrm{OFF}}$, in good agreement with deterministic model for the SET statistics.

Departing from the cell-based percolation model to propose an analytical model for set and reset statistics which are based on the formation and disconnection of a conducting filament (CF) in RRAM devices, this model is composed of two basic elements: (i) cell-based geometrical model to describe the dependence of the RS

distribution on the defect generation in the CF, and (ii) a deterministic model for the set/reset dynamics to describe the relation of the defect generation with measurable variables such as the set/reset voltages and currents. The experimental observations in $HfO_2$-based RRAM devices can be successfully accounted for by our model for RS statistics. The model sets a framework for the consideration of performance-reliability tradeoffs in RRAM.

## 3.5 Conclusions

This chapter has established a general framework for the analysis and modeling of resistive switching statistics for set/reset dynamics, which is inspired by the analogy with the percolation model of oxide breakdown and is based on two elements: (1) a cell-based geometrical description of the switching conducting filament and (2) a deterministic physics-based model, which are found to be equivalent to a simple Weibull model for the switching statistical variables.

For reset statistics, the Weibull slopes of $V_{\mathrm{RESET}}$ and $I_{\mathrm{RESET}}$ are found to be proportional to the number of cells $n$ (the number of parallel paths which form the CF), $\beta_{\mathrm{V}} = \beta_{\mathrm{I}} = (m+1)\alpha n$. This means that the Weibull slopes increase linearly with $1/R_{\mathrm{ON}}$. The scale factor of $V_{\mathrm{RESET63\%}}$ is constant while $I_{\mathrm{RESET63\%}}$ is proportional to $1/R_{\mathrm{ON}}$. For set statistics, both $\beta_{V_{\mathrm{SET}}}$ and $V_{\mathrm{SET63\%}}$ have a linear relation with $\mathrm{Ln}(R_{\mathrm{OFF}})$. Moreover, the experimental results based on $Pt/HfO_2/Pt$ sample for set and reset statistics have been shown in this chapter, which further demonstrates the validity of the general statistics method and the physical analytical model. $V_{\mathrm{RESET63\%}}$, $I_{\mathrm{RESET63\%}}$, $V_{\mathrm{SET63\%}}$ and $\beta_{V_{\mathrm{SET}}}$ are in good accordance with the model for the reset and set statistics. However, $\beta_{V_{\mathrm{RESET}}}$ and $\beta_{I_{\mathrm{RESET}}}$ remain independent of $R_{\mathrm{ON}}$, which means the reset point nearly coincides with the starting point of the CF dissolution and the CF suffers little structural degradation before reset. Our proposed framework allows an improved physics-based understanding the RS mechanisms and set up a basis for the consideration of performance-reliability tradeoffs.

# Chapter 4

## A quantum wire state for RRAM

The operating principle of RRAM is based on the reversible resistive switching (RS) between at least two stable resistance states, the high resistance state (HRS) and the low resistance state (LRS). Understanding the physics of the RS phenomena is of great importance to control the performance, variability and reliability of these devices and to foster their real application as nonvolatile memories. In this chapter, we mainly investigate the reset transition of $HfO_2$-based RRAM structures with emphasis on revealing three-state resistive switching effects.

We focus on both nonpolar switching in symmetric Pt/$HfO_2$/Pt structures and unipolar and bipolar switching in asymmetric Pt/Ti/$HfO_2$/Pt devices. Between the LRS and the HRS, a rather stable intermediate state is revealed and shown to have the properties of a quantum wire (QW). This QW state is characterized by having conductance of the order of $G_0 \sim 2e^2/h$ and represents a natural boundary between two different electron transport regimes. Above the $G_0$ limit, the conduction is associated to extended quantum transport states which connect the two electrodes, while below it, a spatial gap is opened in the conducting filament (CF) and the conduction is controlled by hopping or tunneling.

Three different electrical methods for the reset transition are used in this chapter: ramp-voltage sweep (RVS), successive-voltage sweep (SVS) and constant-voltage stress (CVS) in first three sections respectively. On the contrary, all the set transition was achieved by the application of a voltage ramp with a current compliance limit of 1mA to avoid complete oxide breakdown. All the electrical measurements are performed with a Keithley 4200-SCS semiconductor characterization system. Analysis of the statistics of conductance during the reset experiments strongly support the existence of these three states and help understanding the evolution of the CF structure during RS. Finally, we also perform two-step reset experiments to show the

impact of the intermediate state on the reset voltage and reset current statistical distributions in section 4.4.

## 4.1 Ramp-voltage sweep reset method in Pt/$HfO_2$/Pt and Pt/Ti/$HfO_2$/Pt structures

Firstly, in this section, we study both the Pt/$HfO_2$/Pt and Pt/Ti/$HfO_2$/Pt structures using a ramp-voltage stress (RVS) method, which is the most widely used method for the investigation of the reset transition. The structures of Pt/$HfO_2$/Pt and Pt/Ti/$HfO_2$/Pt have been introduced in detail in section 2.4. These experiments have been performed in Pt/$HfO_2$/Pt structures operated in the unipolar RS mode and in Pt/Ti/$HfO_2$/Pt structures operated under unipolar and bipolar stress conditions.

The measured I-V characteristics during 125 successive RVS reset cycles applied to the Pt/$HfO_2$/Pt structure are shown in Fig. 4.1(a), as a representative example of the reset phenomenology under RVS method. In some cycles, this current drop is large enough to reach the HRS directly. In other cases, the drop is much smaller and it is followed by a more progressive reduction of the CF conductance. When the reset ramp finishes, two well defined bunches of conduction states are observed, one slightly above $G_0$ (red curves) and another one below ~0.1$G_0$ (blue curves). These red curves correspond to the quantum wire state (QW), where the CF behaves as a QW with at least one conducting channel that contributes with ~$G_0$ to the CF conductance. After the final reset event, the conductance is non-linear because a spatial gap has been opened in the CF and this strongly limits the conductance, which must take place either by thermally-assisted tunneling or hopping. The change of transport regime when the CF conductance is of the order of $G_o$ is confirmed by measuring the temperature dependence of the CF conduction as a function of its conductance. Assuming an Arrhenius model for the temperature dependence, $I = I_0 \exp(-E_{ACT}/K_B T)$, the activation energy $E_{ACT}$ measured at low-voltage is reported in Fig. 4.2 to show that the CF conduction is essentially temperature independent when conductance is above $G_0$ (slightly negative values of $E_{ACT}$ account for the metallic-like behavior) while $E_{ACT}$ becomes positive for $G<G_0$ , a signature of temperature-assisted barrier-limited transport. The idea that the CF behaves as a QW with two different transport regimes was previously assumed in the quantum point contact model of CF conduction[10, 70]. This model was shown to reproduce the experimental current-voltage characteristics in different materials and both in the LRS and the HRS, nicely tracking the change from linear to non-linear transport. However, direct evidence of quantum conductance effects has not been reported until very recently [112-114].

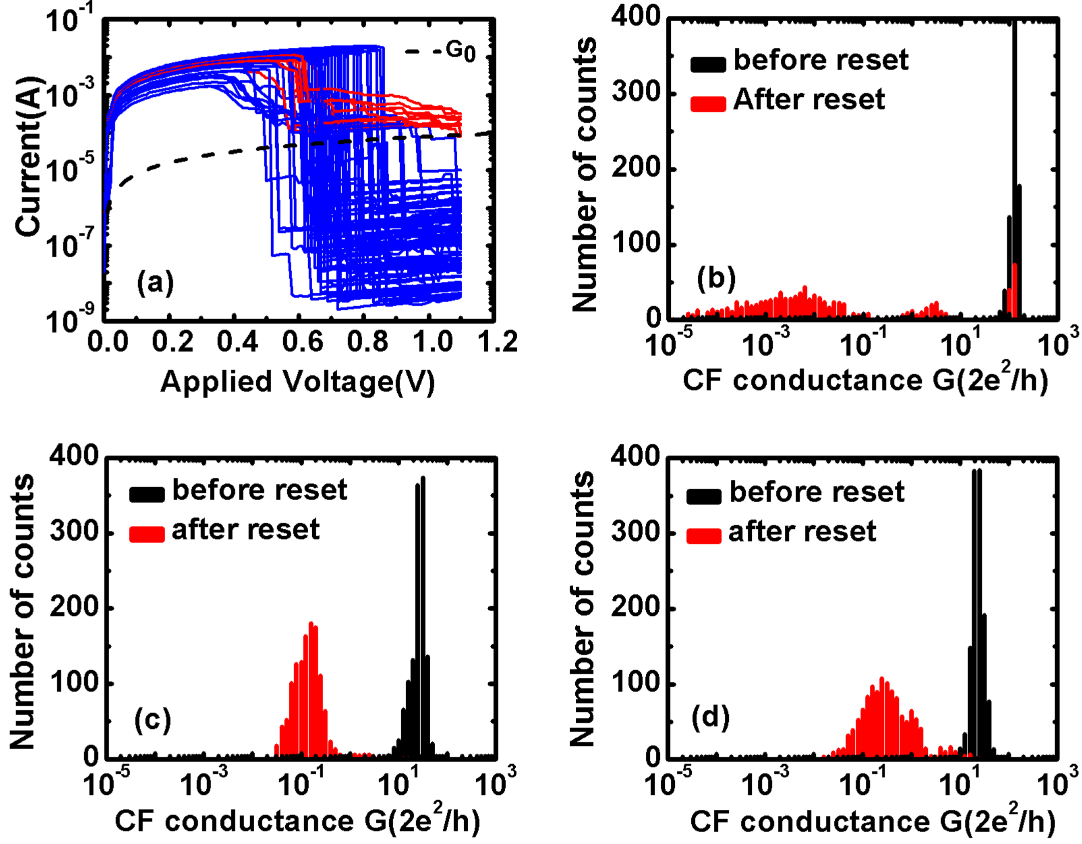


**Fig. 4.1** (a) I-V curves measured during 125 reset cycles using ramped voltage stress method (from 0.1V to 1.1V). The results correspond to a Pt/$HfO_2$/Pt device stressed in the unipolar switching mode. The dashed line represents a linear I-V with conductance equal to the quantum of conductance $G_0$. Low-voltage (0.1V) conductance histograms before and after each reset cycle are represented for long cycling experiments (1250 cycles each) in three different cases: (b) Pt/$HfO_2$/Pt unipolar switching; (c) Pt/Ti/$HfO_2$/Pt bipolar switching and; (d) Pt/Ti/$HfO_2$/Pt unipolar switching.

Inspired by the phenomenology observed in Fig. 4.1(a), we have performed longer cycling experiments consisting in the application of 1250 set/reset cycles on each RRAM device. The statistics of CF conductance measured at low voltage (0.1V) before and after each reset cycle are presented in Fig. 4.1(b) to 4.1(d) for all the analyzed cases. Fig. 4.1(b) shows the conductance histogram for the unipolar reset experiment of Pt/$HfO_2$/Pt samples. While only one peak is observed before reset (the CF is highly conductive as corresponding to the LRS), three peaks are revealed after the reset cycle. One small peak overlaps the LRS peak, this meaning that in some cycles of the experiment, the CF did not suffer any reset. On the other hand, one broad peak is observed spanning several orders of CF conductance and with values below $0.1G_0$[115]. This peak corresponds to the final HRS and, according to previous interpretations[116]; this state is related to a CF with a spatial gap. The CF gap introduces a potential barrier that limits the electron transmission through the filament and this is the reason why the conductance is strongly reduced below the $G_0$ boundary. In between the LRS and the HRS conductance peaks, there is another well-defined

peak located just above $G_0$. This peak is associated to what we have called the intermediate QW state.

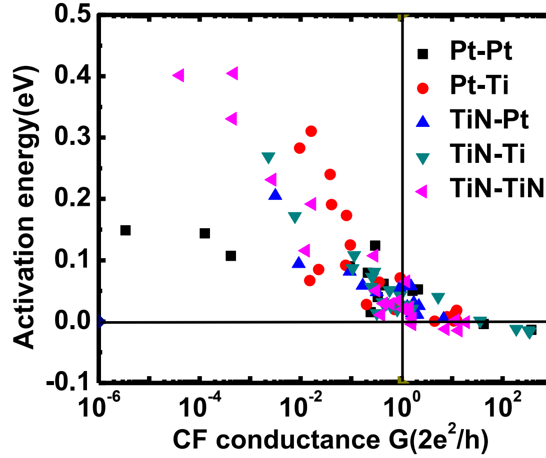


**Fig. 4.2** Activation energy of the low-voltage CF current as a function of the CF conductance normalized to the quantum of conductance. The vertical line emphasizes the change of regime at the CF conductance of the order of $G_0$.

The Pt/Ti/$HfO_2$/Pt devices were operated both in the bipolar (positive set and negative reset) and the unipolar (set and reset under negative polarity) switching modes. The histograms of low-voltage conductance measured before and after set and reported in Fig. 4.1(c) and 4.4(d), respectively. First we notice that the reset is much less effective than in the samples without Ti layer, in the sense that the conductance after reset is only at most slightly below $G_0$. The results obtained under bipolar and unipolar reset conditions are indeed very similar and only one big peak is observed after the reset. Since this peak is centered at approximately $0.1G_0$ and its tail reaches conductance values above $G_0$, we don"t have evidence of the existence of the intermediate QW state in these structures. We believe that the differences in the reported conductance histograms reflect significant differences in the microscopic structure of the CF in both types of structures. We speculate that the CF might be rather symmetric in the case of unipolar switching of Pt/$HfO_2$/Pt structure with the most constrictive region being located near the middle of the filament (hourglass shape) where the higher temperature is reached and favors CF dissolution during reset. On the other hand, in the asymmetric Pt/Ti/$HfO_2$/Pt structure, the CF might be significantly wider at the Ti/$HfO_2$ interface (conical shape) due to the higher density of oxygen vacancies near this interface. This asymmetric CF might limit the extent to which the CF can be reset and make the observation of the intermediate QW state more difficult due to overlapping with the HRS state. These significant differences of CF in both Pt/$HfO_2$/Pt and Pt/Ti/$HfO_2$/Pt structures are also shown in chapter 2. Given these results, our study of the three-state RS effects has focused on the case of unipolar switching in Pt/$HfO_2$/Pt structures in the following sections.

## 4.2 Three-state resistive switching using the successive-voltage sweep reset method.

The transition from the LRS to the intermediate QW state can be controlled by applying successive-voltage ramps with increasing maximum voltage[67], as shown in Fig. 4.3. Although this technique allows a certain control of the reduction of the CF conductance when $G>G_0$, i.e. a control of the transition from the LRS to the intermediate QW state, the resistance of the final HRS is difficult to control. This is because in the HRS the CF conductance depends exponentially on the length of the spatial gap opened in the CF. The successive-voltage sweep (SVS) experiment of Fig. 4.3 corresponds to a Pt/$HfO_2$/Pt structure subjected to unipolar switching conditions. As shown in Fig. 4.3(a), the CF conductance is reduced from the initial value of ~125$G_0$ to a conductance of ~8$G_0$ with six successive voltage sweeps. The seventh sweep caused a disconnection of the CF (a spatial gap was opened) and the CF conductance was reduced by orders of magnitude. We speculate that this progressive reduction of conductance is achieved by making the CF progressively narrower. The last voltage sweep, however, disrupts the CF and opens a gap, thus decreasing its conductance by several orders of magnitude. Similar results are shown in Fig. 4.3(b). In this experiment, the CF conductance is reduced from the initial value of 210$G_0$ to 1.5$G_0$ through the application of 10 successive-voltage sweeps with increasing maximum voltage.

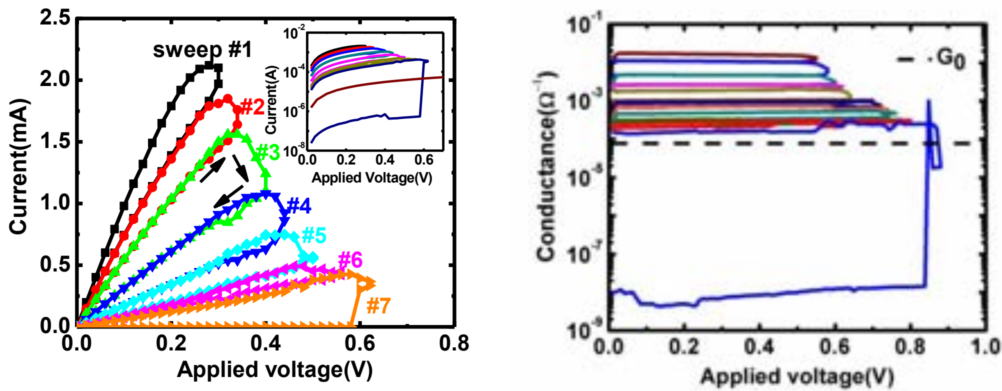


**Fig. 4.3** Control of the transition from the LRS to the intermediate reset state by a voltage ramp with maximum voltage. By progressively increasing the maximum voltage, the conductance of the CF can be controlled down to a value close to $G_0$. (a) From an initial conductance of 125$G_0$, the first six sweeps reduce the CF conductance to 95$G_0$, 70$G_0$, 40$G_0$, 22$G_0$, 13$G_0$ and 8$G_0$, respectively. This progressive reduction of conductance is achieved by making the CF progressively narrower. The seventh sweep disrupts the CF and opens a gap, thus decreasing its conductance by several orders of magnitude, as shown in the inset, which depicts the same results using a logarithmic current scale. (b) By progressively increasing the maximum voltage, the conductance of the CF can be controlled down to a value close to $G_0$ (dashed line). When a gap is opened in the CF, an abrupt current drop of several orders of magnitude is registered, and the HRS

state is reached.

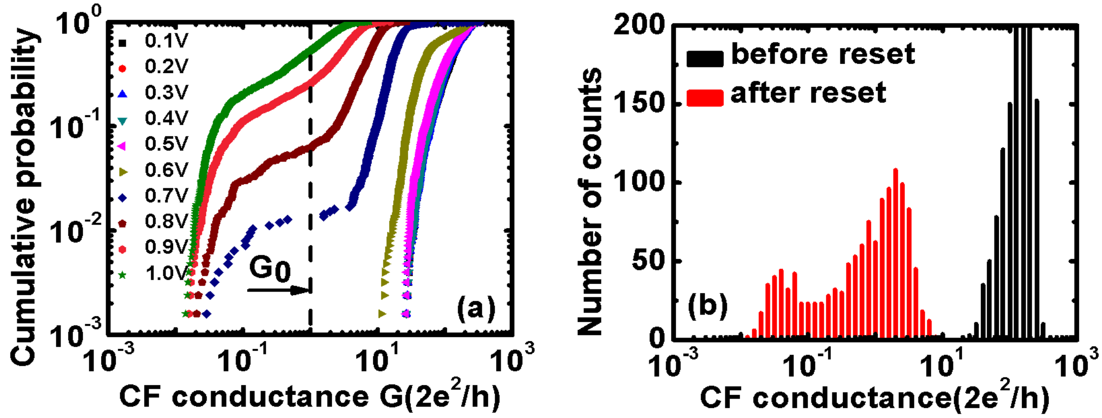


**Fig. 4.4** (a) Distributions of CF conductance G ($2e^2/h$) measured during 1250 cycles SVS reset experiment. The conductance was measured at low voltage (0.1V) after the application of each reset voltage ramp with maximum voltage increasing from 0.1V to 1.0V. (b) The histograms of CF conductance G ($2e^2/h$) measured at the end of each reset cycle during a SVS reset experiment consisting in 1250 cycles. In the LRS, the characteristic conductance peak is around $100G_0$. After the reset process, two clear peaks are distinguished. A large peak is located above $G_0$ and small amplitude peak is below $0.1G_0$.

Given these results, we designed a 1250 cycles SVS experiment in which the set transition was achieved by a single RVS (positive bias) while each reset cycle consisted in the application of 10 successive-voltage ramps with increasing maximum voltage starting from 0.1 V and ending at 1.0V with a linear increment step of 0.1V. After each partial reset ramp, the voltage is swept back to 0V and the CF conductance is measured at low voltage (0.1V). With this method we obtain the statistical distributions of CF conductance as a function of the maximum partial reset voltage, as shown in Fig. 4.4(a). Note that the conductance distribution remains nearly unchanged while the maximum reset voltage is kept below 0.6V. Only a shoulder begins to appear at this voltage and this corresponds to the initial progressive transition from the LRS to the intermediate QW state. At $V_{MAX}$=0.7V, the distribution already shows significant changes. In particular we can identify two plateaus which separate three steep regions which correspond to the LRS ($G/G_0 \sim 10^2$), the intermediate QW state ($0.1 < G/G_0 < 10$) and the HRS ($G/G_0 < 0.1$). For $V_{MAX}$=0.8V and above, the LRS peak does not appear anymore and the distribution of conductance is bimodal. This means that reset has occurred in all the cycles. However, while a certain fraction of them have reached the HRS (full reset), in the majority of cases, a small CF remains as a QW connection between the electrodes.

The histograms of CF conductance both before and after reset are shown in Fig. 4.4(b). Before the reset (i.e. after the application of the set voltage ramp), the device are in the LRS and the conductance shows a single peak around $100G_0$. After the complete application of the reset cycles, two clear peaks are distinguished. A large peak is located above $G_0$ and small amplitude peak is below $0.1G_0$. As in the case of the conventional RVS reset method, the first peak is interpreted as being associated to the intermediate QW state. On the other hand, the low-conductance peak is considered

to correspond to the HRS. These results further support the existence of an intermediate QW state between the LRS and the HRS, confirming the results of the RVS reset experiment. Moreover, it is realized that under the softer stress conditions of SVS reset cycling, the transitions towards the QW state are strongly favored as compared to the direct transitions to the HRS. This indicates that the conductance of the final state after reset strongly depends on the details of the reset algorithm. To further investigate this issue, we have performed constant-voltage reset experiments under different voltages in next section 4.3.

## 4.3 Unipolar reset of Pt/$HfO_2$/Pt structures under constant-voltage conditions

In this section, we study the reset phenomenology when the reset transition is achieved by means of a constant voltage stress in the Pt/$HfO_2$/Pt structures operating in the unipolar switching mode. The CVS reset experiment consists in the application of a constant voltage during a long enough time so as to induce the transition from the LRS to the HRS. This reset mode is similar to the fast reset (in the nanosecond scale) induced by high voltage pulses which are required for practical RRAM applications. However, the stress voltages considered here are much smaller and the associated reset times are orders of magnitude longer (in the scale of hundreds of seconds). Under CVS conditions, the reset transition is registered as a sudden current drop in the time evolution of the current (or conductance), as shown in Fig. 4.5. In our experiments, the CVS stress voltage were varied from 0.5V to 0.9V and, between each CVS stress, a RVS was used to set the device back into its original LRS.

Fig. 4.5(a) to Fig. 4.5(c) show the conductance-time traces corresponding to three different CVS reset voltages. Fig. 4.5(a) shows the current-time traces corresponding to a CVS reset experiment at 0.6V applied to a single device during 125 cycles set/reset experiment. Each reset curve is measured after a RVS set transition. According to the set I-V curves (not shown), in all the cycles, the system ends up in the LRS. However, not all the measured reset traces begin with the high current corresponding to the LRS and this is due to the fact that they suffer reset before the first current measurement. In the time scale of hundreds of seconds, all the reset I-t traces shows one or more sudden current drops which correspond to partial reset events which are related either to a reduction of the CF width or to the opening of a spatial gap in the filament. As we have already reported in the case of RVS and SVS, at the end of the stress experiment, the CF conductance is either above (red lines) or orders of magnitude below (blue lines) the quantum of conductance. In other words, these RS structures show three obvious states: (1) the LRS, corresponding to a wide CF with classical metallic properties; (2) a partial reset state in which the CF behaves as a QW and which can be as narrow as a single-defect conducting path; and (3) the HRS, in which a physical gap has been opened in the CF. A single transport channel QW with a conductance ～$G_0$ represents the natural boundary between two different reset states.

In Fig. 4.5, we can also notice that under this CVS conditions, the intermediate QW state is more stable than the initial LRS. If the transition from the LRS to the QW state occurs, then the transition to the final HRS is strongly suppressed. This means that a transition to the QW state might induce a reset failure. However, the relative probability of a reset transition from the initial LRS to the intermediate QW state or to the final HRS changes with the applied voltage. This is demonstrated in Fig. 4.5(b) and Fig. 4.5(c), which shows the current-time traces corresponding to CVS experiments performed at 0.55V and 0.8V, respectively. If we compare these results with those reported in Fig. 4.5(a), it becomes evident that the higher is the stress voltage, the higher is the probability to fully reset the CF by creating a spatial gap in it. This indicates that the QW state might have negligible importance when the devices are operated under high voltage pulses.

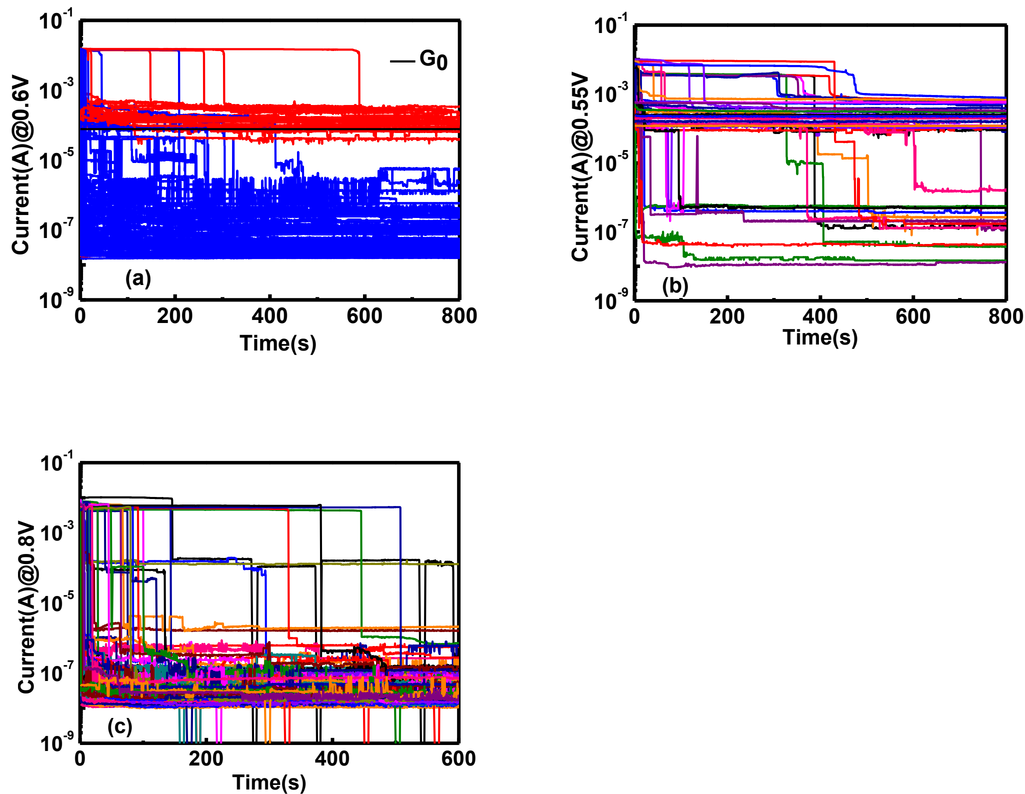


**Fig. 4.5** (a) Evolution of the CF current during a 0.6V constant-voltage stress reset experiment. The initial current is about 10 mA and the structure is in the LRS. When the reset experiment finishes (after 800 s) two different final situations are possible which correspond to two different types of CF states (red or blue curves, respectively). One corresponds to a continuous CF, i.e. to the intermediate QW state, and the other is related to a broken CF, and corresponds to the HRS. (b) CVS reset experiment at 0.55V and (c) 0.8V demonstrating the voltage-dependent probability of the reset transition to the intermediate QW state of the final HRS.

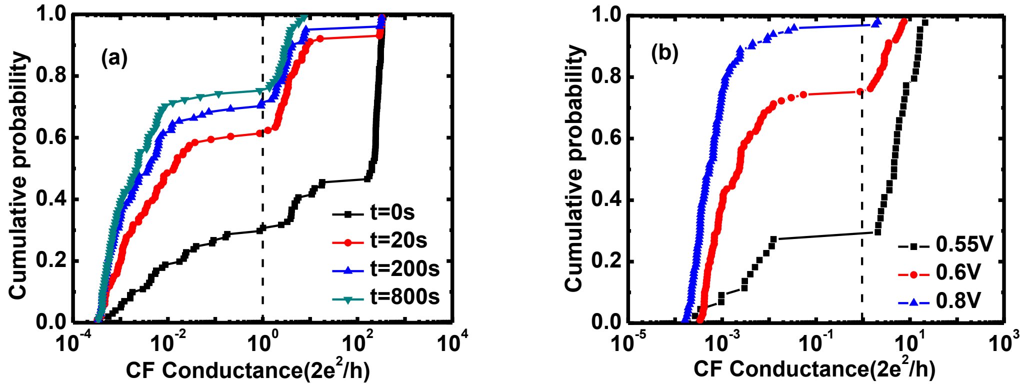


**Fig. 4.6** (a) Cumulative distribution of CF conductance after different CVS stress times (at 0.6V); (b) Cumulative distribution of CF conductance after 600s of stress under different voltages.

Again, these three-state RS phenomena are clearly revealed in the cumulative statistical distributions of conductance obtained for different stress times. To construct these distributions, all the reset cycles were considered and the cumulative probability F(G) is represented in Fig. 4.6(a) as a function of CF conductance, which is defined as the fraction of samples showing CF conductance smaller than G. In the distribution corresponding to the first current reading (labeled as t=0s), almost 50% of the cycles had already shown some reset event. However, at the beginning of the reset cycle (i.e. just after the previous set transition), the device is always in the LRS. In consequence, in most of the cycles, the reset occurs very fast, during the duration of the first current measurement under the CVS. In the distributions corresponding to 0s, 20s and 200s, two plateaus are found to separate three regions with dF/dG>0. These conductance ranges correspond to the three states of the CF: the HRS, the intermediate QW state and the LRS. After 200s of stress, the CF can only be found either in the HRS or the intermediate QW state.

The probability of the transition from the LRS to the intermediate QW decreases with the applied voltage and the fraction of cycles which end with the CF in the HRS increases. This is shown in Fig. 4.6(b) which shows the cumulative conductance probability corresponding to three CVS reset experiments performed at 0.55V, 0.6V and 0.8V, respectively. From these results, it becomes evident that the higher is the stress voltage, the higher is the probability to fully reset the CF by creating a spatial gap. This indicates that the QW state might have negligible importance when the devices are operated under high voltage pulses. However, this issue should be further evaluated to determine whether the transition to the QW state can induce some kind of memory failure under realistic operation conditions even if with low probability. The impact of the transition to the intermediate QW state is further explored in the following section 4.4 where the results of two-step reset experiments are reported. In any case, the results obtained under CVS reset conditions confirm the three-state switching phenomenology in Pt/$HfO_2$/Pt structures operated in the unipolar switching mode. From Fig. 4.6, we can also demonstrate that the higher stability of the QW state might be due to a reduction of energy dissipation in the CF constriction (ballistic

transport through the CF and energy dissipation in the anode metal electrode) but it can also be related to the fact that the reset voltage increases with the resistance of the CF. From the practical point of view, the enhanced stability of the QW state might cause reset failures because a transition from the LRS to the intermediate QW state might impede the ulterior transition to the final HRS. This issue is further explored in the following section 4.4 by means of two-step reset experiments.

## 4.4 Two-step reset experiments of unipolar switching in Pt/$HfO_2$/Pt structures

In the previous section, we have concluded that the transitions to the intermediate QW state during reset experiments might reduce the probability of full reset of the CF to the HRS. To investigate this issue, we have designed two-step reset experiments consisting in a low-voltage CVS stage (0.55V and 30s) followed by a conventional RVS cycle. The goal of the initial CVS is to cause a transition from the LRS to the intermediate QW state in most of the samples. The final RVS reset properties are then compared with those obtained with an equivalent RVS reset experiment performed without the initial CVS. In this way, we obtain information about the impact of the QW state on the final transition to the HRS.

Fig. 4.7(a) and Fig. 4.7 (b) show the scatter plots of the final reset voltage (during the RVS) and final reset current, respectively. The impact of the initial CVS on the initial resistance of the CF is evident in these two figures. Except some cycles which remained in the LRS and showed CF initial resistances below 100 Ω, the rest of cycles suffered a transition from the LRS to the intermediate QW state and showed initial CF resistances well above this value and up to $10^4$ Ω. This increase of initial CF resistance causes an increase of the reset voltage and a decrease of the reset current which is shown to be compatible with the thermal dissolution of the CF[8], as shown by the model lines in Fig. 4.7(a) and 4.7(b). The same results can also be represented in Fig. 4.7(c) and 4.7(d) in the form of cumulative distributions of reset voltage and reset current, respectively. These two figures show how the reset voltages are increased while the reset current decreases. However, since the thermal dissolution process is voltage controlled (the voltage determines the local temperature and hence the rate of diffusion of oxygen species), we can conclude that the transition to the intermediate QW state increases the stress requirements for the full transition to the HRS. The decrease of the reset current is fully determined by the increase of CF resistance associated to the transition from LRS to intermediate QW state. The increase of the voltage required to fully reset the CF to the HRS in those cycles that suffer the transition to the QW state needs to be accounted in the design of the reset operation to avoid reset failures related to this issue. Notice that this works has demonstrated that the transitions to the QW state occur under any kind of reset methodology. It is true that the probability of these transitions to the QW state are strongly suppressed at the

high stress voltages required for fast pulse RRAM operation. However, these should anyhow be considered to increase the reset yield to high percentiles.

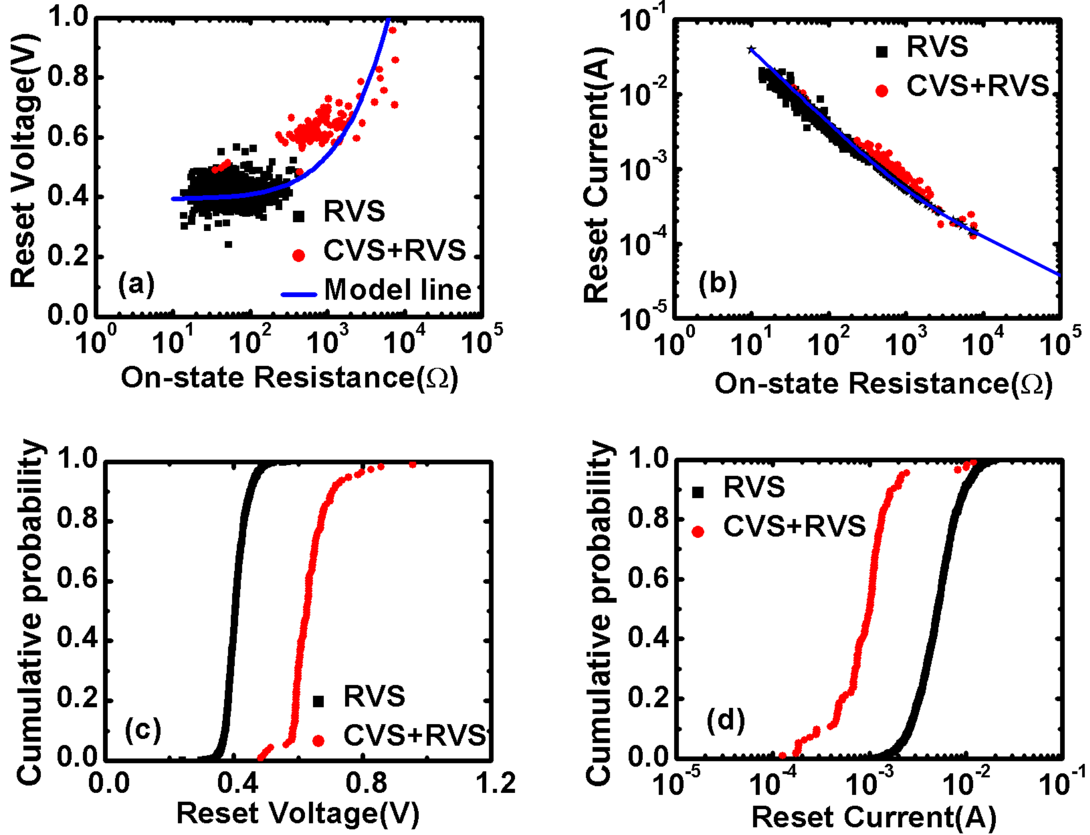


**Fig. 4.7** Comparison of the results of a two-step reset experiment with those of a conventional RVS reset. The experiments were performed on the very same sample. The two-step reset method consists in an initial low-voltage CVS reset cycle (the CVS stress voltage is 0.55V and the during time is 30s) which induces the transition to the intermediate QW state with high probability and a subsequent VRS reset which is used to determine the distribution of reset voltage and current. (a) Scatter plot of the reset voltage versus the resistance of the CF in the LRS (at the beginning of the RVS step); the model line corresponds to a simple analytical thermal dissolution model[67]; (b) Scatter plot of the reset current as a function of the CF resistance in the LRS; the model line correspond to the simple thermal dissolution model[67]; (c) Cumulative distribution of reset voltage during the RVS reset cycle with and without the initial CVS phase; (d) Cumulative distribution of reset current during the RVS reset cycle with and without the initial CVS phase.

The existence of a QW state has been demonstrated for the resistive switching CF in Pt/$HfO_2$/Pt devices. No clear evidence of this intermediate QW state is found in Pt/Ti/$HfO_2$/Pt operated under unipolar or bipolar conditions. This might be due to the much lower resistances of the HRS achieved in these structures, likely related to the asymmetric shape of the CF. Different methods have been used for the reset including RVS, CVS and SVS. In all cases, experiments support the three-state RS phenomenon. Three states are identified for the CF: (1) the LRS, which corresponds to a wide CF with metallic properties; (2) a partial reset state in which the CF behaves as a QW;

and (3) the HRS, in which a physical gap has been opened in the CF. The probability of full reset (transition from LRS to HRS) has been reported to increase with the applied voltage but in all the reported experiments a significant fraction of the CFs remains in the QW state. It has also been demonstrated that the transitions from the LRS to the QW state increases the voltage required for the full reset of the CF. Thus, this issue needs to be taken into account when designing reset operation algorithms.

# Chapter 5

## Conclusions

On the basis of the RS effect of transition metal oxides (TMOs), RRAM is widely accepted as a promising candidate for future non-volatile memory applications due to its simple structure, good scalability, high switching speed, low operation current and power. RS in electroformed TMOs has been used to design new electron devices that behave as memristors. These devices, which are based on the combined action of ions (which store the information) and electrons (which carry the current), are important for the new NVM technology based on RRAM, for reconfigurable nanoelectronic hardware and neuromorphic computing architectures. The memory function in RRAM is achieved through the reversible RS between at least two stable resistance states, the HRS and the LRS. In this dissertation we aim at exploring the physics of CF and switching statistics of $HfO_2$-based RRAM devices.

This thesis focuses on two key issues: (1) unveiling the physics of the switching and conductance mechanisms of CF and (2) exploring and modeling the switching statistics and the reliability issues. Therefore, this thesis has been divided into three main parts. The first one is dedicated to reveal the nature of the CF, its conduction properties and the mechanisms which control its formation and disruption, which is shown in Chapter 2. The second part is dedicated to study the statistical variation of switching parameters of RRAM devices, which is introduced in Chapter 3. Departing from the cell-based percolation model of gate dielectric breakdown to propose an analytical model for set and reset statistics in RRAM devices. The third one is to reveal three-state RS effects for $HfO_2$-based RRAM devices using RVS, SVS and CVS these three different electrical methods. These experimental results are given in Chapter 4.

In Chapter 2, the QPC model has been applied to model the conduction properties

of CF in $HfO_2$-based RRAM devices both in the HRS and the LRS.

a. On the basis of Landauer transmission approach to conduction along narrow microscopic constrictions, the formula of QPC model for multiple breakdown paths has been obtained in MOS devices. This equation can be applicable to both the HRS and the LRS for $HfO_2$-based RRAM devices;
b. The QPC model has been reformulated by coupling it to the results of ab-initio simulations of oxygen vacancy paths. Assuming that $m^{*}{\sim}m_0$ results in a barrier height $\Phi{\sim}1.16\,\text{eV}$, which is a perfectly consistent value. As a result, the new QPC model has three fitting parameters: the number of vacancy paths *N*, the average $t_{gap}$ ($t_{gap} = 0.12\alpha\Phi\,\text{nm}$) and the average value of the asymmetry parameter $\beta\,(0 < \beta < 1)$. The Least square-estimation (LSE) method has been used to extract the three QPC parameters according to fit the experimental I-V curves;
c. Fitting of the experimental I-V characteristics in both HRS and the LRS provides indirect information about the microscopic structure of the CF for Pt/Ti/$HfO_2$/Pt and Pt/$HfO_2$/Pt structures. For nonpolar Pt/$HfO_2$/Pt structure, the CF is symmetry where the most constrictive part is in the center of the CF. Starting from a very wide CF in the LRS, the width of the CF in its narrowest part reduces to a limit where only one or few oxygen vacancy paths connect the electrodes. This stage is followed by the opening of a gap that the thickness of the most conductive single vacancy path determines the CF conductance in the HRS;
d. For Pt/Ti/$HfO_2$/Pt structure, the CF is highly asymmetry, with the narrowest constrictive part near the bottom of interface. The Ti film is believed to act as an oxygen extraction layer and to introduce a high density of oxygen vacancies in the $HfO_2$. In the LRS, the CF area is rather large and there is one re-oxidized vacancy gap for bipolar RS mode, then the gap increases to two or three vacancies and the CF is narrower than the LRS. For unipolar RS mode, the number of paths in the HRS is much less than bipolar RS mode, this is to say, the unipolar RS mode is more effective than bipolar RS mode.

In Chapter 3, departing from the cell-based percolation model of oxide BD, a general framework to deal with the statistics of CF-based resistive switching has been developed, which is composed of two elements:

a. A cell-based geometrical model to describe the dependence of the RS distribution on the defect generation in the CF;
b. A deterministic model for the reset and set dynamics to describe the relation of the defect generation with measurable variables such as the voltages and currents.

A reset deterministic model predicts a constant $V_{\text{RESET63\%}}$ while $\beta_{V_{\text{RESET}}}$, $\beta_{I_{\text{RESET}}}$ and $I_{\text{RESET63\%}}$ are predicted to be proportional to $n$ (i.e. proportional to $1/R_{\text{ON}}$). A compact analytical model for the set switching statistics predicts that both $\beta_{V_{\text{SET}}}$ and $V_{\text{SET63\%}}$ have a linear relation with $\text{Ln}(R_{\text{OFF}})$;

c. The experimental results based on the Pt/$HfO_2$/Pt sample for reset and set statistics have been shown in section 3.4, which further demonstrates the validity of the general statistics method and the physical analytical model. $V_{\mathrm{RESET63\%}}$, $I_{\mathrm{RESET63\%}}$, $V_{\mathrm{SET63\%}}$ and $\beta_{V_{\mathrm{SET}}}$ are in good accordance with the model for the reset and set statistics. However, $\beta_{V_{\mathrm{RESET}}}$ and $\beta_{I_{\mathrm{RESET}}}$ remain independent of $R_{\mathrm{ON}}$, which means the reset point nearly coincides with the starting point of the CF dissolution and the CF suffers little structural degradation before reset.

In Chapter 4, the reset transition of $HfO_2$-based RRAM structures has been investigated in detail with emphasis on revealing three-state resistive switching effects.

a. A rather stable intermediate state is revealed and shown to have the properties of QW by using three different electrical methods, RVS, SVS and CVS. This QW state is characterized by having conductance of the order of $G_0\sim 2e^2/h$ and represents a natural boundary between two different electron transport regimes.
b. Three obvious states are: (1) the LRS, corresponding to a wide CF with classical metallic properties; (2) a partial reset state in which the CF behaves as a QW and which can be as narrow as a single-defect conducting path; and (3) the HRS, in which a physical gap has been opened in the CF. A single transport channel QW with a conductance $\sim G_0$ represents the natural boundary between two different reset states.
c. Two-step reset experiments consisting in a low-voltage CVS stage followed by a conventional RVS cycle has been designed to show the impact of the intermediate state on the reset voltage and reset current statistical distributions. The goal of the initial CVS is to cause a transition from the LRS to the intermediate QW state in most of the samples. The final RVS reset properties are then compared with those obtained with an equivalent RVS reset experiment performed without the initial CVS.

To conclude, the QPC model is shown to adequately model the conduction properties of CF in $HfO_2$-based RRAM devices both in the HRS and the LRS. The Least square-estimation method has been used to extract the QPC parameters according to fit the experimental I-V curves excellently, which provide indirect information about the microscopic structure of the CF in both Pt/$HfO_2$/Pt and Pt/Ti/$HfO_2$/Pt devices. An analytical model for the reset and set statistics in RRAM devices has been developed, which is made up of two elements: (a) a cell-based geometrical model to describe the dependence of the RS distribution on the defect generation in the CF and (b) a deterministic model for the reset and set dynamics to describe the relation of the defect generation with measurable variables such as the voltages and currents. Finally, we obtain the three RS states, the LRS, the QW state and the HRS. The QW state has the conductance of the value of $G_0\sim 2e^2/h$ and has the impact on reset voltage and reset current statistical distributions.

# References

1. C. Sealy, "Winning the memory race", Materialstoday, vol. 11, No: 6, pp. 16-18, 2008.
2. J. J. Yang, F. Miao, M. Pickett, D. Ohlberg, D. Steward, Ch. Lau and R.S. Williams, "The mechanism of electroforming of metal oxide memristive switches", Nanotechnology 20, 215201 (2009).
3. H.-S. P. Wong, H.-Y. Lee, S. Yu, Y.-S. Chen, Y. Wu, P.-S. Chen, B. Lee, F.T. Chen, M.-J. Tsai, "Metal Oxide RRAM," invited paper, Proceedings of the IEEE, vol. 100, No. 6, pp. 1951-1970, June, 2012.
4. W. R. Hiatt and T.W. Hickmott, "bistable switching in niobium oxide diodes", Appl. Phys. Lett. 6, 106 (1965).
5. S. R. Ovshinsky, "reversible electrical switching phenomena in disordered structures", Phys. Rev. Lett., 21, 1450 (1968).
6. K. L. Chopra, "Current-controlled negative resistance in thin niobium oxide films", Proc. IEEE 51, 941 (and 1784) (1963).
7. D. Ielmini and Y. Zhang, "Analytical model for subthreshold conduction and threshold switching in chalcogenide-based memory devices", J. Appl. Phys. 102, 054517 (2007).
8. S. Lavizzari, D. Ielmini and A. L. Lacaita, "Transient Simulation of Delay and Switching Effects in Phase-Change Memories", IEEE Trans. Elect. Dev. 57, 3257 (2010).
9. K. M. Kim, D. S. Jeong, and C. S. Hwang, "Nanofilamentary resistive switching in binary oxide system; a review on the present status and outlook", Nanotechnology, vol. 22, p. 254002 (2011).
10. R. Degraeve, P. H. Roussel, L. Goux, D. Wouters, J. Kittl, L. Altimime, M. Jurczak, G. . Groeseneken, "Generic learning of TDDB applied to RRAM for improved understanding of conduction and switching mechanism through multiple filaments", Techn. Dig. of Int. Electron Devices Meeting, pp. 632-635, 2010.
11. J. Suñé, E. Miranda, D. Jiménez, S. Long, M. Liu. Invited talk, "From dielectric failure to memory function: Learning from oxide breakdown for improved

understanding of resistive switching memories", 11th Non-Volatile Memory Technology Symposium, Shanghai, China, 2011.

12. I. K. Yoo, B. S. Kang, S. E. Ahn, C. B. Lee, M. J. Lee, G. S. Park and X. S. Li, "Fractal Dimension of Conducting Paths in Nickel Oxide (NiO) Thin Films during Resistance Switching", IEEE Trans. Nanotechnology, 9, 131 (2010).
13. D. H. Kwon, K. M. Kim, J. H. Jang, J. M. Jeon, M. H. Lee, G. H. Kim, X. S. Li, G. S. Park, B. Lee, S. Han, M. Kim, and C. S. Hwang, "Atomic structure of conducting nanofilaments in $TiO_2$ resistive switching memory," Nat. Nanotechnol. 5, 148 (2010).
14. J. P. Stratchan, M. D. Pickett, J. J. Yang, S. Aloni, A. L. David Kilcoyne, G. Medeiros-Ribeiro, R. Stanle Williams, "Direct identification of the conducting channels in a functioning memristive device", Adv. Mater., 22, 3573 (2010).
15. A. Sawa, "Resistive switching in transition metal oxides", Mater. Today, vol. 11, pp. 28-36, 2008.
16. G. Dearnaley, A. M. Stoneham, and D. V. Morgan, "Electrical phenomena in amorphous oxide films", Rep. Prog. Phys., 33, 1129 (1970).
17. S. Seo, M. J. Lee, D. H. Seo, E. J. Jeoung, D.-S. Suh, Y. S. Joung, I. K. Yoo, I. R. Hwang, S. H. Kim, I. S. Byun, J.-S. Kim, J. S. Choi, and B. H. Park, "Reproducible resistance switching in polycrystalline NiO films", Appl. Phys. Lett., 85, 5655 (2004);
18. B. J. Choi, D. S. Jeong and S. K. Kim, "Resistive switching mechanism of TiO2 thin films grown by atomic-layer deposition", J. Appl. Phys. 98, 033715 (2005).
19. D. B. Strukov, G. S. Snider, D. R. Stewart and R. S. Williams, "The missing memristor found", Nature, 453, 80 (2008);
20. L. O. Chua, "Memristor-The Missing Circuit Element", IEEE Trans. Circuit Theory, 18, 507 (1971).
21. L. Chua, "Resistance switching memories are memristors", Appl. Phys. A, 102, 785 (2011).
22. Y. Iwasa, T. Koda, S. Koshihara, Y. Tokura, N. Iwasawa, G. Saito, "Intrinsic negative-resistance effect in mixed-stack charge-transfer crystals", Phys. Rev. B, 39(1989)10441-10444.
23. A. Asamitsu, Y. Tomioka, H. Kuwahara, and Y. Tokura, "Current switching of resistive states in magnetoresistive manganites", Nature 388, 50-52, 1997.
24. M. N. Kozicki, M. Yun, L. Hilt and A. Singh, "Applications of programmable resistance changes in metal-doped chalcogenides", Pennington NJ USA: Electrochem. Soc. 298-309, 1999.
25. A. Beck, J. G. Bednorz, C. Gerber, C. Rossel, and D. Widmer, "Reproducible switching effect in thin oxide films for memory applications", Appl. Phys. Lett., vol. 77, pp. 139-141, 2000.
26. Y. Watanabe, J. G. Bednorz, A. Bietsch, Ch. Gerber, D. Widmer, A. Beck, and S. J. Wind, "Current-driven insulator-conductor transition and nonvolatile memory in chromium-doped $SrTiO_3$ single crystals," Appl. Phys. Lett., vol. 78, pp. 3738-3740, 2001.
27. C. Rohde, B. J. Choi, D. S. Jeong, S. Choi, J. S. Zhao, and C. S. Hwang,

"Identification of a determining parameter for resistive switching of $TiO_2$ thin films," Appl. Phys. Lett., vol. 86, 262907, 2005.
28. I. G. Baek, M. S. Lee, S. Seo, M. J. Lee, D. H. Seo, D.-S. Suh, J. C. Park, S. O. Park, H. S. Kim, I. K. Yoo, U.-In. Chung, and J. T. Moon, "Highly scalable nonvolatile resistive memory using simple binary oxide driven by asymmetric unipolar voltage pulses," in Tech. Dig. IEEE Int. Electron Devices Meeting, pp. 587-590, 2004.
29. R. Waser, R. Dittmann, G. Staikov, and K. Szot, "Redox-based resistive switching memories- nanoionic mechanisms, prospects, and challenges,"Adv. Mater., vol. 21, pp. 2632-2663, 2009.
30. K. Szot, M. Rogala,W. Speier, Z. Klusek, A. Besmehn and R.Waser, "$TiO_2$-a prototypical memristive material", Nanotechnology 22, 254001 (2011).
31. D. Ielmini, R. Bruchhaus, R. Waser, "Thermochemical resistive switching: materials, mechanisms, and scaling projections", Phase Transitions 84, 570-602 (2011).
32. I. Valov, R. Waser, J. R. Jameson and M. N. Kozicki, "Electrochemical metallization memories-fundamentals, applications, prospects", Nanotechnology 22, 254003 (2011).
33. D. Ielmini and A. Lacaita, "Phase change materials in non-volatile storage", Materials Today, 14, 600-607 (2011).
34. M. Wuttig and N. Yamada, "Phase-change materials for rewriteable data storage," Nat. Mater, 6, 824 (2007).
35. J. Borguetti, Z. Li, J. Straznicky, X. Li, D. A. A. Ohlberg, W. Wu, D. R. Steward and R. S. Williams, "A hybrid nanomemristor/transistor logic circuit capable of self-programming", Proceedings of the National Academy of Sciences 106, 1699-1703 (2009).
36. D. A. Patterson, "Latency lags bandwidth," Communications of the ACM, vol. 47, no. 10, pp. 71-75, Oct. 2004.
37. E. Linn, R. Rosezin, C. Kügeler and R. Waser, "Complementary resistive switches for passive nanocrossbar memories," Nat. Mater 9, 403 (2010).
38. G. I. Meijer, "Who Wins the Nonvolatile Memory Race?" Science 319, 1625 (2008).
39. M. Di Ventra, Y. V. Pershin, "Biologically-Inspired Electronics with Memory Circuit Elements", Mater. Today 44, 584 (2011).
40. Prof. Di Ventra"s group at the University of California Santa Barbara is a reference in the the theory of memristive devices and applications.
41. R. Freitas and W.W. Wilcke, "Storage-class memory: The next storage system technology", IBM J. Res. & Dev. 52, 439-447 (2008).
42. C. Lau, D. Stewart, R.S. Williams, and M. Bockrath, "Direct Observation of Nanoscale Switching Centers in Metal/Molecule/Metal Structures", Nano Lett, 4, 569 (2004).
43. G. Snider, "Self-organized computation with unreliable, memristive nanodevices", Nanotechnology 18, 365202 (2007).
44. Q. Xia, "Nanoscale resistive switches: devices, fabrication and integration", Appl.

Phys. A 102, 955 (2011).
45. D. Strukov and K. Likharev, "CMOL FPGA: A cell-based, reconfigurable architecture for hybrid digital circuits using two-terminal nanodevices", Nanotechnology 16, 888 (2005).
46. G. Snider and R. S. Williams, "Nano/CMOS architectures using a field-programmable nanowire interconnect", Nanotechnology 18, 035204 (2007).
47. J. Borguetti, Z. Li, J. Straznicky, X. Li, D. A. A. Ohlberg, W. Wu, D. R. Steward and R. S. Williams, "A hybrid nanomemristor/transistor logic circuit capable of self-programming", Proc. Nat. Acad. Sci. 106, 1699 (2009).
48. Y. V. Pershin and M. di Ventra, "Practical approach to programmable analog circuits with memristors", IEEE Trans. Circuits & Syst., 57, 1857 (2010).
49. D. B. Strukov, "Smart connections", Nature (London) 476, 403 (2011).
50. M. Versace and B. Chandler, "The Brain of a New Machine", IEEE Spectrum 47, 30-37 (2010).
51. S. H. Jo, T. Chang, I. Ebong, B. B. Bhadviya, P. Mazumder and W. Lu, "Nanoscale memristor device as synapse in neuromorphic systems", Nano Lett. 10, 1297 (2010).
52. D. Kuzum, R. G. D. Jeyasingh, B. Lee, and H.-S. P. Wong, "Nanoelectronic Programmable Synapses Based on Phase Change Materials for Brain-Inspired Computing", Nano Lett. (online) (2011).
53. Profs. Wong and Nishi at Stanford University lead the Non-Volatile Memory Technology Research Initiative considering RRAM in addition to other memories such as PCRAM.
54. T. Ohno, T. Hasegawa, T. Tsuruoka, K. Terabe, J. K. Gimzewski and M. Aono, "Atomically controlled electrochemical nucleation at superionic solid electrolyte surfaces electrolyte surfaces", Nat. Mater. 10, 591 (2011).
55. Aono"s group at the National Institute for material science has been key for the development of the atom-transistor which essentially behaves as a memistor.
56. S. Long, X. Lian, C.Cagli, L. Perniola, H. Lv, Q.Liu, L. Li, Z. Huo, E. Miranda, D. Jiménez, M. Liu, J. Suñé, "Compact Analytical Models for the SET and RESET Switching Statistics of RRAM Inspired in the Cell-Based Percolation Model of Gate Dielectric Breakdown", IEEE International Reliability Physics Symposium (IRPS) 2013.
57. J. S. Lee, S. B. Lee, S. H. Chang, L. G. Gao, B. S. Kang, M.-J. Lee, C. J. Kim, T. W. Noh, and B. Kahng, "Scaling theory for unipolar resistance switching," Phys. Rev. Lett., vol. 105, p. 205701, 2010.
58. S. C. Chae, J. S. Lee, S. Kim, S. B. Lee, S. H. Chang, C. Liu, B. Kahng, H. Shin, D.-W. Kim, C. U. Jung, S. Seo, M.-J. Lee, and T. W. Noh,"Random circuit breaker network model for unipolar resistance switching," Adv. Mater., vol. 20, pp. 1154-1159, 2008.
59. H. D. Lee, B. Magyari-Köpe, and Y. Nishi, "Model of Metallic Filament Formation and Rupture in NiO for Unipolar Switching," Phys. Rev. B, vol. 81, p. 193202, 2010.
60. A. Kalantarian, G. Bersuker, D.C. Gilmer, D. Veksler, B. Butcher, A. Padovani, O.

Pirrotta, L. Larcher, R. Geer, Y. Nishi, and P. Kirsch,“Controlling uniformity of RRAM characteristics through the forming process,” Proc. of the International Reliability Physics Symposium, pp. 6C.4.1-6C.4.5, 2012.

61. Y. Wang, Q. Liu, S. Long, W. Wang, Q. Wang, M. Zhang, S. Zhang, Y. Li, Q. Zuo, J. Yang, and M. Liu, “Investigation of resistive switching in Cu-doped $HfO_2$ thin film for multilevel non-volatile memory applications,” Nanotechnology, vol. 21, no.4, p. 45202, Jan. 2010.
62. H. Y. Lee, Y. S. Chen, P. S. Chen, P. Y. Gu, Y. Y. Hsu, S. M. Wang, W. H. Liu, C. H. Tsai, S. S. Sheu, P. C. Chiang, W. P. Lin, C. H. Lin, W. S. Chen, F. T. Chen, C. H. Lien, and M.-J. Tsai, “Evidence and solution of over-RESET problem for HfOx based resistive memory with sub-ns switching speed and high endurance,” in IEDM Tech. Dig., 2010, pp. 460-463.
63. J. Lee, J. Shin, D. Lee, W. Lee, S. Jung, M. Jo, J. Park, K. P. Biju, S. Kim, S. Park, and H. Hwang, “Diode-less nano-scale ZrOx/HfOx RRAM device with excellent switching uniformity and reliability for high-density cross-point memory applications,” in IEDM Tech. Dig., 2010, pp. 452-455.
64. J. Suñé, E. Miranda, M. Nafria and X. Aymerich, “ Point contact conduction at the oxide breakdown of MOS devices”, Techn. Dig. of IEEE Int. Electron Devices Meeting, pp. 191-194 (1998).
65. J. Suñé and E. Miranda, “Post soft breakdown conduction in $SiO_2$ gate oxides”, Techn. Dig. of the IEEE Int. Electron Devices Meeting, pp. 533-536 (2000).
66. S. Yu, X. Guan, and H.-S. P. Wong, “Conduction mechanism of TiN/HfOx/Pt resistive switching memory: a trap-assisted-tunneling model”, Appl. Phys. Lett. 99, 063507 (2011).
67. D. Ielmini, F. Nardi and C. Cagli, “Physical models of size-dependent nanofilament formation and rupture in NiO resistive switching memories”, Nanotechnology 22, 254022 (2011).
68. D. Ielmini, “Modeling the Universal Set/Reset Characteristics of Bipolar RRAM by Field- and Temperature-Driven Filament Growth”, IEEE Trans. Electron Devices 58, 4309 (2011).
69. H. Y. Lee, P.-S. Chen, T.-Y. Wu, Y. S. Chen, F. Chen, C.-C. Wang, P.-J. Tzeng, C. H. Lin, M.-J. Tsai, and C. Lien, “HfOx Bipolar Resistive Memory With Robust Endurance Using AlCu as Buffer Electrode”, IEEE Electron Device Lett. 30, 703 (2009).
70. E. Miranda, C. Walczyk, C. Wenger, and T. Schroeder, “Model for the resistive switching effect in $HfO_2$ MIM structures based on the transmission properties of narrow constrictions”, IEEE Electron Device Lett. 31, 609 (2010).
71. S. Datta, Electronic transport in microscopic systems, Cambridge University Press, 1997.
72. M. Büttiker, “Quantized transmission of a saddle-point constriction”, Phys. Rev. B41, 7906(1990).
73. E. N. Bogachek, A. G. Scherbakov, and U. Landman, “Shape effects on conductance quantization in three-dimensional nanowires: Hard versus soft potentials”, Phys. Rev. B 56, 1065 (1997).

74. E. Miranda and J. Suñé, “Analytic Modeling of leakage current through multiple breakdown paths in $SiO_2$ films”, Annual Proceedings-Reliability Physics (Symposium). 367-379 (2001).
75. J. M. Soler, E. Artacho, J. D. Gale, A. García, J. Junquera, P. Ordejón, and D. Sánchez-Portal, “The SIESTA method for ab initio order-N materials simulation”, J. Phys.:Condens. Matter 14, 2745 (2002).
76. J. P. Perdew, K. Burke, and M. Ernzerhof, “Generalized Gradient Approximation Made Simple”, Phys. Rev. Lett. 77, 3865 (1996).
77. X. Zhao and D. Vanderbilt, “First-principles Study of Electronic and Dielectric Properties of $ZrO_2$ and $HfO_2$”, Phys. Rev. B 65, 233106 (2002).
78. H. J. Monkhorst and J. D. Pack, “On Special Points for Brillouin Zone Integrations”, Phys. Rev. B 13, 5188 (1976).
79. S.-G. Park, B. Magyari-Köpe, and Y. Nishi, “Electron correlation effects in reduced rutile $TiO_2$ within the LDA+U method”, Phys. Rev. B 82, 115109 (2010).
80. N. F. Mott, “Metal-Insulator Transitions”, 2nd ed., Taylor Francis, London, 1990.
81. X. Cartoixà, R. Rurali and J. Suñé, “Transport properties of oxygen vacancy filaments in metal / crystalline or amorphous $HfO_2$ / metal structures”, Phys. Rev. B 86, 165445 (2012).
82. U. Russo, D. Ielmini, C. Cagli, A. L. Lacaita, S. Spiga, C. Wiemer, M. Perego, M. Fanciulli, “Conductive-filament switching analysis and self-accelerated thermal dissolution model for reset in NiO-based RRAM”, in IEDM Tech. Dig. 2007, 775.
83. U. Russo, D. Ielmini, C. Cagli and A.L. Lacaita, “Self-Accelerated Thermal Dissolution Model for Reset Programming in Unipolar Resistive-Switching Memory (RRAM) Devices”, IEEE Trans. Elect. Dev. 56, 193 (2009).
84. D. C. Gilmer, G. Bersuker, S. Koveshnikov, M. Jo, A. Kalantarian, B. Butcher, R. Geer, Y. Nishi, P. D. Kirsch and R. Jammy, “Asymmetry, Vacancy Engineering and Mechanism for Bipolar RRAM”, Proc. of IEEE International Memory Workshop, 978 (2012).
85. D. J. DiMaria, E. Cartier and D. Arnold, “Impact Ionization, Trap Creation, Degradation, and Breakdown in Silicon Dioxide Films on Silicon,” Journal of Applied Physics, vol.73, no. 7, pp. 3367-3384, 1993.
86. R. Degraeve, P. H. Roussel, G. Groeseneken, and H. E. Maes, “A new analytic model for the description of the intrinsic oxide breakdown statistics of ultra-thin oxides,” Microelectronics and Reliability, vol. 36, no. 11-12, pp. 1639-1642, 1996.
87. R. Degraeve, B. Kaczer and G. Groeseneken, “Degradation and breakdown in thin oxide layers: mechanisms, models and reliability prediction,” Microelectronics Reliability, vol.39, no. 10, pp. 1445-1460, 1999.
88. J. Suñé, I. Placencia, N. Barniol, E. Farrés, F. Martín, and X. Aymerich, “On the breakdown statistics of very thin $SiO_2$ films,” Thin Solid Films, vol. 185, no. 2, pp. 347-362, 1990.
89. S. Long, C. Cagli, D. Ielmini, M. Liu, and J. Suñé. “Analysis and modeling of resistive switching statistics,” Journal of Applied Physics, 2012, 111, 074508.
90. J. Suñé, G. Mura and E. Miranda, “Are soft breakdown and hard breakdown of ultrathin gate oxides actually different failure mechanisms?” IEEE Electron

Device Letters, vol. 21, No.4, 2000.
91. E. Miranda, J. Suñé, R. Rodríguez, M. Nafría and X. Aymerich, "Soft breakdown fluctuation events in ultrathin $SiO_2$ layers," Applied Physics Letters, vol. 73, no. 4, pp. 490-492, 1998.
92. S. Lee, B. Cho, J. Kim i S. Choi, "Quasi-breakdown of ultrathin gate oxide under high field stress," Proceedings of the International Electron Devices Meeting, pp. 605-608, 1994.
93. K. Okada, S. Kawasaki, and Y. Hirofuji, "New experimental findings on stress induced leakage current of ultra-thin silicon dioxides," in Ext. Abstr. 1994 Int. Conf. Solid State Devices and Materials, pp. 565-567, 1994.
94. B. P. Linder, S. Lombardo, J. H. Stathis, A. Vayshen and D. J. Frank, "Voltage dependence of hard breakdown growth and the reliability implication in thin dielectrics," IEEE Electron Device Letters, vol. 23, no. 11, pp. 661-663, 2002.
95. F. Monsieur, E. Vincent, D. Roy, S. Bruyere, J. C. Vildeuil, G. Pananakakis and G. Ghibaudo, "A thorough investigation of progresive breakdown in ultra-thin oxides. Physical understanding and application for industrial reliability assessment," Proceedings of the IEEE International Reliability Physics Symposium (IRPS), pp. 45-54, 2002.
96. J. Suñé, E. Y. Wu, W. L. Lai, "Statistics of Competing Post-Breakdown Failure Modes in Ultrathin MOS Devices", IEEE Electron Device Letters, vol. 53, no. 2, pp. 224-234, 2006.
97. R. Degraeve, G. Groeseneken, R. Bellens, J. L. Ogier, M. Depas, P. J. Roussel, and H. E. Maes, "A consistent model for the thickness dependence of intrinsic breakdown in ultra-thin oxides", in IEDM Tech. Dig., 1995, pp. 866-869.
98. J. H. Stathis, "Percolation models for gate oxide breakdown," J. Appl. Phys., vol. 86, no. 10, pp. 5757-5766, Nov. 1999.
99. J. Suñé, "New physics-based analytic approach to the thin-oxide breakdown statistics," IEEE Electron Device Lett., vol. 22, no. 6, pp. 296-298, Jun. 2001.
100. A. T. Krishnan and P. Nicollian, "Analytic extension of the cell-based oxide breakdown model to full percolation and its implications," Proc. of the International Reliability Physics Symposium 2007, p. 232-239.
101. E. Y. Wu and J. Suñé, "Power-law voltage acceleration: A key element for ultra-thin gate oxide reliability," Microelectronic Reliability, vol. 45, 1809-1834 (2005).
102. E. Y. Wu , J. Suñé, W. Lai, E. Nowak, J. McKenna, and A. Vayshenker, "Interplay of voltage and temperature acceleration of oxide breakdown for ultra-thin oxides," Solid-State Electronics vol. 46, 1787-1798 (2002).
103. A. Conde, C. Martínez-Domingo, D. Jiménez, E. Miranda, J.M. Rafí, F. Campabadal and J. Suñé, "Modeling the breakdown statistics of $Al_2O_3/HfO_2$ nanolaminates grown by Atomic-Layer-Deposition," Solid-State Electronics (2011) Vol. 71, 48-52 (2012).
104. E. Y. Wu, J. H. Stathis, and L. K. Han, "Ultra-thin oxide reliability for ULSI applications", Semicond. Sci. Technol. 15 (2000) 425-435.
105. E. Y. Wu, J. Suñé, and W. Lai, "On the Weibull Shape Factor of Intrinsic

Breakdown of Dielectric Films and Its Accurate Experimental Determination-Part II Experimental Results and the Effects of Stress Conditions," IEEE Trans. Electron Devices, vol. 49, no. 12, pp. 2141-2150, Dec. 2002.

106. J. Suñé, S. Tous, and E. Y. Wu, "Analytical cell-based model for the breakdown statistics of multilayer insulator stacks," IEEE Electron Device Lett., vol. 30, pp. 1359-1361, 2009.

107. S. Tous, E. Y. Wu and J. Suñé, "A compact analytic model for the breakdown distribution of gate stack dielectrics," Proc. of the International Reliability Physics Symposium, pp. 792-798, 2010.

108. W.-C. Luo, K.-L. Liun, J.-J. Huang, C.-L. Lee, and T.-H. Hou, "Rapid prediction of RRAM RESET-state disturb by ramped voltage stress," IEEE Electron Device Lett., vol. 33, pp. 597-599, April 2012.

109. W.-C. Luo, J.-C. Liu, H.-T. Feng, Y.-C. Lin, J.-J. Huang, K.-L. Lin, and T.-H. Hou, "RRAM SET speed-disturb dilemma and rapid statistical prediction methodology," International Electron Device Meeting Tech. Dig., 2012.

110. S. Long, C. Cagli, D. Ielmini, M. Liu, and J. Suñé, "Reset Statistics of NiO-Based Resistive Switching Memories," IEEE Electron Device Lett., vol. 32, no. 11, pp. 1570-1572, Nov. 2011.

111. U. Russo, D. Ielmini, C. Cagli, and A. L. Lacaita, "Filament conduction and reset mechanism in NiO-based resistive-switching memory (RRAM) devices," IEEE Trans. Electron Devices, vol. 56, pp. 186-192, 2009.

112. S. Long, C. Gagli, X. Cartoixà, R. Rurali, E. Miranda, D. Jiménez, J. Buckley, M. Liu and J. Suñé, "Conductance quantization in resistive switching, in Frontiers in electronic materials", Nature Conference, p.257, Wiley-VCH (2012).

113. X. Zhu et al., "Observation of Conductance Quantization in Oxide-Based Resistive Switching Memory", Adv. Mat. DOI: 10.1002/adma.201201506 (2012).

114. S. Tappertzhofen, I. Valov and R. Waser, "Quantum conductance and switching kinetics of AgI-based microcrossbar cells", Nanotechnology, 23, 145703 (6pp) (2012).

115. S. Long, X. Lian, C. Cagli, X. Cartoixà, R. Rurali, E. Miranda, D. Jiménez, L. Perniola, M. Liu and J. Suñé, "Quantum-size effects in hafnium-oxide resistive switching", Appl. Phys. Lett., 2013:102: 183505.

116. S. Long, X. Lian, C. Cagli, L. Perniola, E. Miranda, M Liu and J. Suñé, "A Model for the Set Statistics of RRAM Inspired in the Percolation Model of Oxide Breakdown", Electron Device Letters, IEEE,2013, 8 (34) :999-1001.

# PAPERS (A-E)

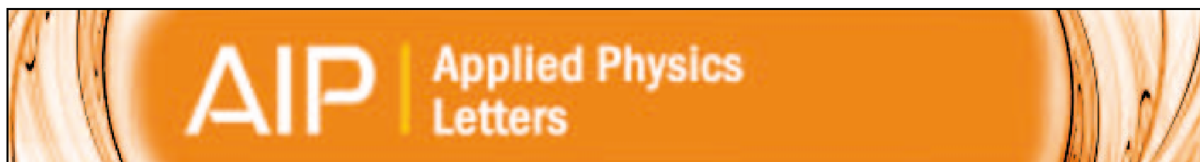


# Quantum-size effects in hafnium-oxide resistive switching

Shibing Long, Xiaojuan Lian, Carlo Cagli, Xavier Cartoix , Riccardo Rurali, Enrique Miranda, David Jiménez, Luca Perniola, Ming Liu, and Jordi Su é

Citation: Applied Physics Letters **102**, 183505 (2013); doi: 10.1063/1.4802265
View online: http://dx.doi.org/10.1063/1.4802265
View Table of Contents: http://scitation.aip.org/content/aip/journal/apl/102/18?ver=pdfcov
Published by the AIP Publishing

**Articles you may be interested in**

Conductance quantization in oxygen-anion-migration-based resistive switching memory devices
Appl. Phys. Lett. **103**, 043510 (2013); 10.1063/1.4816747

Well controlled multiple resistive switching states in the Al local doped HfO2 resistive random access memory device
J. Appl. Phys. **113**, 164507 (2013); 10.1063/1.4803076

Resistive switching mechanisms relating to oxygen vacancies migration in both interfaces in Ti/HfOx/Pt memory devices
J. Appl. Phys. **113**, 064510 (2013); 10.1063/1.4791695

Role of oxygen vacancies in TiO2-based resistive switches
J. Appl. Phys. **113**, 033707 (2013); 10.1063/1.4779767

Improvement of resistive switching characteristics in TiO 2 thin films with embedded Pt nanocrystals
Appl. Phys. Lett. **95**, 042104 (2009); 10.1063/1.3193656

This article is copyrighted as indicated in the article. Reuse of AIP content is subject to the terms at: http://scitation.aip.org/termsconditions. Downloaded to IP: 158.109.68.252 On: Wed, 23 Apr 2014 10:22:57

# Quantum-size effects in hafnium-oxide resistive switching

Shibing Long,[1,2] Xiaojuan Lian,[1] Carlo Cagli,[3] Xavier Cartoixà,[1] Riccardo Rurali,[4] Enrique Miranda,[1] David Jiménez,[1] Luca Perniola,[3] Ming Liu,[2] and Jordi Suñé[1,a)]
[1]*Departament d'Enginyeria Electrònica, Universitat Autònoma de Barcelona, Bellaterra, Spain*
[2]*Laboratory of Nanofabrication and Novel Device Integration, Institute of Microelectronics, Chinese Academy of Sciences, Beijing, China*
[3]*CEA-LETI, Grenoble, France*
[4]*Institut de Ciència de Materials de Barcelona (ICMAB-CSIC), Bellaterra, Spain*

(Received 25 January 2013; accepted 5 April 2013; published online 7 May 2013)

Discrete changes of conductance of the order of $G_0 = 2e^2/h$ reported during the unipolar reset transitions of Pt/$HfO_2$/Pt structures are interpreted as the signature of atomic-size variations of the conducting filament (CF) nanostructure. Our results suggest that the reset occurs in two phases: a progressive narrowing of the CF to the limit of a quantum wire (QW) followed by the opening of a spatial gap that exponentially reduces the CF transmission. First principles calculations show that oxygen vacancy paths in $HfO_2$ with single- to few-atom diameters behave as QWs and are capable of carrying current with $G_0$ conductance. © *2013 AIP Publishing LLC*. [http://dx.doi.org/10.1063/1.4802265]

Simple metal-insulator-metal (MIM) devices show memory properties related to reversible chemical and structural changes that translate into a non-volatile modification of the electrical resistance.[1] An important feature of these resistive switching (RS) phenomena is the combined implication of ions and electrons.[2] Electrons are responsible for the conduction, and ions modify the internal state of the device, thus introducing the memory effects. In the case of interest to this Letter, RS is related to the formation and partial destruction of a nanoscale conducting filament (CF). The nature of the CF is different in different material systems,[3,4] and so are the conduction and switching properties.[1,5–7] However, all these systems share some important features, involving the motion of ions and redox reactions, which form and destroy the CF during the set and reset transitions, respectively. Understanding the physics of the RS phenomena is of great importance to control the performance, variability, and reliability of these devices and to foster their real application as non-volatile memories.

In this Letter, we focus on the reset transition in Pt/$HfO_2$/Pt devices operated under unipolar switching conditions, i.e., the same voltage polarity is used for set and reset. The considered structures are 2.5 $\mu m^2$ MIM capacitors fabricated in a mesa structure on top of a tungsten plug. The insulator is a 10-nm-thick $HfO_2$ layer deposited by atomic layer deposition (ALD) at 350 °C on top of the Pt bottom electrode (BE), followed by Pt top electrode (TE) deposition and patterning. BE and TE were deposited by physical vapor deposition (PVD). Samples with other metal electrodes including Ti and TiN were also considered in the measurements of the temperature dependence of the CF resistance. These RS devices require a preliminary electrical stress usually known as *electroforming* to activate the switching. In the case of CF-based RS, electroforming is very similar to a soft dielectric breakdown event and consists in the generation of at least one CF. After electroforming, long lasting repetitive set/reset cycling experiments (1250 consecutive cycles) were performed using a voltage ramp both for set and reset. During the set transition, a compliance current with 1 mA was applied to avoid the hard breakdown of the $HfO_2$ layer. In the High-Resistance-State (HRS), the resistance distribution is quite wide (spanning from $\sim 10^4\,\Omega$ to more than $10^7\,\Omega$); while in the Low-Resistance-State (LRS), the resistance is around $10^2\,\Omega$, with much smaller variation. Fig. 1 reports some examples of the current-voltage characteristics measured during typical reset cycles. All these curves show a rather abrupt current drop (particularly when the LRS conductance is high) followed by a progressive current reduction. These curves finally show abrupt jumps between discrete current levels with conductance of the order of few times the quantum of conductance, $G_0 = 2e^2/h$. These results are very similar to those obtained for atomic-sized conductors using different techniques, such as mechanically controllable break junctions or different experiments based on scanning tunneling microscopy.[8,9]

These similarities suggest that the current levels shown in Fig. 1 are related to conductance quantization or to structural variations of the CF constriction involving the motion of one or very few atoms. On the other hand, all the reset traces show a final drop to zero in the linear current scale of Fig. 1(b), which appears as a change of orders of magnitude in the log scale of Fig. 1(a). Before the final current drop, the CF behaves as a quantum wire (QW) with at least one conducting channel that contributes with $\sim G_0$ to the CF conductance. After the final reset event, the conduction is nonlinear because a spatial gap has been opened in the CF and it might be related to thermally assisted tunneling or hopping.

A way to further reveal preferred atomic-scale configurations and/or quantization of the conductance is to study the statistics of conductance readings. Fig. 1(c) shows the histogram of the CF conductance at the point of the final transition to the HRS. At this point, the conductance range is limited to few times $G_o$ (two orders of magnitude smaller

a)Author to whom correspondence should be addressed. E-mail: jordi.sune@uab.cat. Telephone: +34-935813527. Fax: +34-935812600

 © 2013 AIP Publishing LLC

This article is copyrighted as indicated in the article. Reuse of AIP content is subject to the terms at: http://scitation.aip.org/termsconditions. Downloaded to IP: 158.109.68.252 On: Wed, 23 Apr 2014 10:22:57

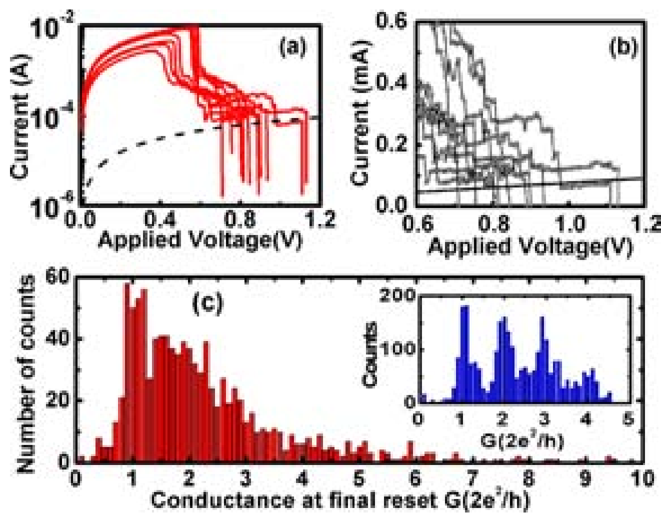


FIG. 1. (a) Current-voltage traces measured during the application of reset voltage ramps. The dashed line corresponds to a linear I(V) with conductance equal to $G_0 = 2e^2/h$. (b) Detail of the current-voltage evolution during the last phase of the reset transients. (c) Histogram of conductance at the final *reset* point; the inset shows the histogram of conductance readings during 100 successive conductance-time traces.

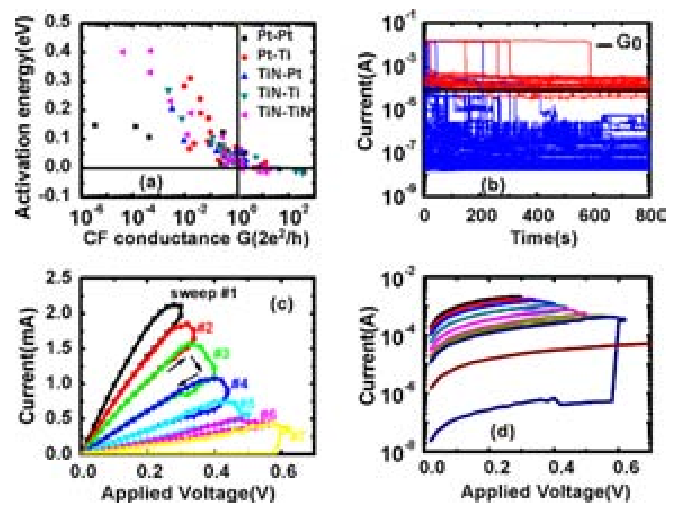


FIG. 2. (a) Activation energy of the low-voltage CF current as a function of the CF conductance. The vertical line emphasizes the change of transport regime for CF conductance of the order of $G_0$. (b) Evolution of the CF current during a constant-voltage reset experiment. (c) Control of the transition from the LRS to the intermediate reset state by successive voltage ramps with increasing maximum voltage. From an initial conductance of $125G_0$, the first six sweeps reduce the CF conductance to $95G_0$, $70G_0$, $40G_0$, $22G_0$, $13G_0$, and $8G_0$, respectively. The seventh sweep disrupts the CF and opens a gap, thus decreasing its conductance by several orders of magnitude, as shown in (d), which depicts the same results in a logarithmic current scale together with a reference line ($I = G_0V$).

than in the initial LRS), a clear peak is found at $G \sim G_0$ and the probability of higher values of CF conductance decreases exponentially. This emphasizes that $G_0$ is a natural physics-based boundary between the LRS and the HRS, and supports the idea that there is an intermediate reset state in which the CF is a nanoscale filament with properties similar to a QW. However, the existence of preferred CF atomic-scale configurations or of conductance quantization is not revealed by any clear peak structure in Fig. 1(c). Assuming that this might be due to averaging effects related to the drift of the CF shape along the cycling experiment, we have considered a subset of only 100 successive reset cycles. Both the direct observation of the conductance-voltage traces and the conductance histogram (see inset of Fig. 1(c)) clearly reveal the existence of well-defined atomic-size configurations of the CF. The peaks at roughly integer multiples of $G_0$ can either be due to the CF behaving as a QW or to a nanoscale CF cross section corresponding to few atomic-size conducting defects.

The change of transport regime when the CF conductance is of the order of $G_0$ is confirmed by the temperature dependence of the CF conduction as a function of its conductance. Assuming an Arrhenius model for the temperature dependence, $I = I_o \exp(-E_{ACT}/K_BT)$, the activation energy $E_{ACT}$ measured at low-voltage is reported in Fig. 2(a) to show that the CF conduction is essentially temperature independent when its conductance is above $G_0$ (slightly negative values of $E_{ACT}$ account for the metallic-like behavior) while $E_{ACT}$ becomes positive for $G < G_0$, a signature of temperature-assisted barrier-limited transport.

The idea that the CF behaves as a QW with two different transport regimes was previously assumed in the quantum point contact model of CF conduction,[10,11] an extension of a model initially proposed for the post-breakdown conduction through thin gate oxides.[12] This model was shown to reproduce the experimental current-voltage characteristics in different materials and both in the LRS and the HRS, nicely tracking the change from linear to non-linear transport. However, direct evidence of quantum conductance effects has not been reported until very recently and only in systems in which active metal cations form a CF through a solid electrolyte.[13–15] The results presented in this Letter suggest that these quantum-size effects also appear in systems in which oxygen vacancies are considered to form the CFs.

The existence of two well-defined transport regimes is also evidenced by constant-voltage stress (CVS) reset experiments. Fig. 2(b) shows that after some time under CVS conditions, a reset transition occurs from the LRS to a lower conductance state. At the end of the stress experiment, the CF conductance is either above (red lines) or orders of magnitude below (blue lines) the quantum of conductance. This indicates that either a narrow CF remains and supports one or few quantum modes or there is spatial gap in the CF that strongly suppresses the conduction. In other words, these RS structures show three well defined states: (1) the LRS, corresponding to a wide CF with classical metallic properties; (2) a partial reset state in which the CF behaves as a QW and which can be as narrow as a single-defect conducting path; and (3) the HRS, in which a physical gap has been opened in the CF, so that the conduction is non-linear and strongly temperature dependent. The transition from the LRS to the intermediate QW state can be controlled by applying successive voltage ramps with increasing maximum voltage,[16] as shown in Fig. 2(c). In this particular experiment, the CF conductance is reduced from the initial value of $\sim 125G_0$ to a conductance of $\sim 8G_0$ with six successive voltage sweeps. The seventh sweep caused a disconnection of the CF (a spatial gap was opened), and the CF conductance was reduced by orders of magnitude, as shown in Fig. 2(d). Although this technique allows a certain control of the reduction of the CF

This article is copyrighted as indicated in the article. Reuse of AIP content is subject to the terms at: http://scitation.aip.org/termsconditions. Downloaded to IP: 158.109.68.252 On: Wed, 23 Apr 2014 10:22:57

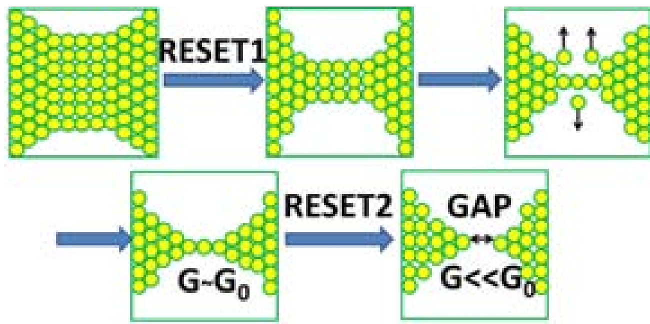


FIG. 3. Schematic representation of the evolution of the CF structure during the reset transient.

diameter when $G > G_0$, the resistance of the final HRS is difficult to control because the CF conductance depends exponentially on the gap length.

A qualitative explanation of the previous results is given in the schematic diagram of Fig. 3. In the LRS, a large number of conducting defects (likely oxygen vacancies) form a wide CF with metallic conducting properties. During the application of the reset voltage ramp, a critical temperature is reached and induces the first abrupt reset event (RESET 1), which in most of the cases causes a significant narrowing of the CF. After this abrupt event, the CF conductance progressively evolves until the CF is only composed by one or few single defect paths. Then, the final transition to the HRS occurs when a gap is opened in the CF (RESET 2). In this figure, we have arbitrarily assumed that the CF becomes narrower in the center of the insulator film. However, asymmetric CF shapes are also possible and this should not significantly alter the results provided that the CF has an atomic-scale size at its most constrictive section.

Oxygen vacancies have been suggested to play a significant role in the RS phenomenon in transition metal oxides with non-active metal electrodes. The results of this Letter suggest that, before the transition to the HRS, the CF behaves as a nanoscale filament with one or few defects in its most constrictive section (or as a bundle of single-defect wide filaments). Therefore, our next step was exploring whether oxygen vacancy paths can explain this type of behavior. To address this, we have carried out first-principles calculations in order to obtain the electronic structure of oxygen vacancy filaments in a crystalline $HfO_2$ host. These calculations are made within the density-functional theory (DFT), as implemented in the SIESTA package.[17,18] In order to minimize the coupling between the filament instances, which we take to be along the **c** axis for the crystalline material (see Ref. 19 for the definition of the axes), we use a $3 \times 3$ supercell of the monoclinic unit cell—the stable phase up to 1720 °C—in the **ab** directions, sampling them in the Brillouin zone with a grid of $2 \times 2$ of **k**-points within the Monkhorst-Pack algorithm.[20] All the structures discussed have been relaxed until all the forces on the atoms were lower than 0.04 eV/Å. The ballistic conductance is calculated from first-principles within Landauer theory.[21] Open boundary conditions are accounted for through the left (right) self-energy. The zero-bias transmission T(E) is calculated using non-equilibrium Green's functions, and the conductance is then calculated through the Landauer formula as $G = T(E)G_0$.

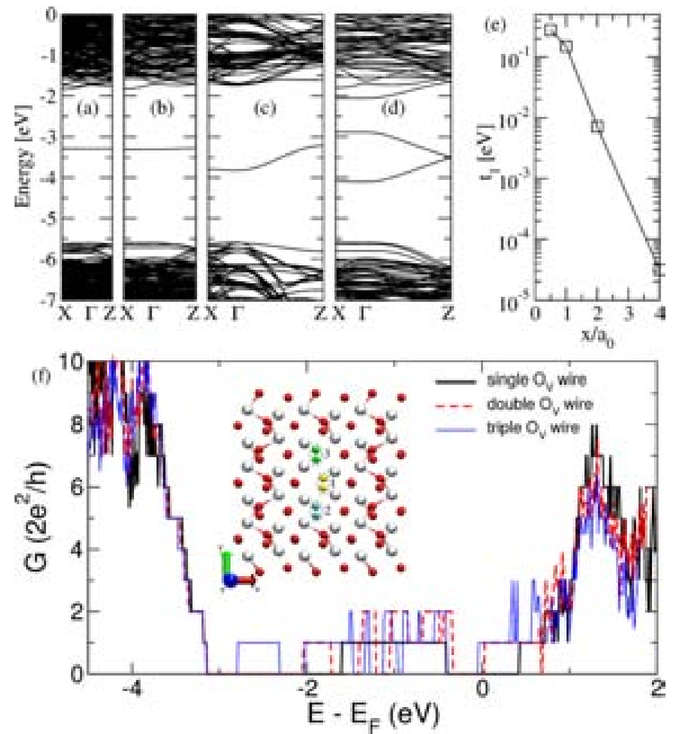


FIG. 4. Band structure for crystalline m-$HfO_2$ with O vacancies separated by (a) $4a_0$, (b) 2 $a_0$, (c) $a_0$ and (d) $a_0/2$. (e) Hopping parameter as a function of vacancy-vacancy separation. (f) Conductance as a function of energy corresponding to a $HfO_2$ matrix where one, two, or three O atom rows are removed. The rows subsequently removed are shown in the instate (marked as "1," "2," and "3"), where red and white spheres correspond to O and Hf atoms, respectively.

The removal of a single O atom in a monoclinic-$HfO_2$ (m-$HfO_2$) matrix introduces a filled impurity state in the gap, similarly to $TiO_2$,[22] but farther from the band edges [see Fig. 4(a)]. The spatial extent of the impurity wavefunction determines the state overlap between two neighboring vacancies and thus relates to the transition from hopping to band transport. Figures 4(a)–4(d) show the band structure of m-$HfO_2$ with a chain of oxygen vacancies that are increasingly close together. It can be seen that, as the overlap between the impurity wavefunctions increases, the impurity band width increases as well. This can be well described with a single band, second-neighbor one-dimensional (1D) tight-binding Hamiltonian, which is well known to have the dispersion relation

$$E(k_x) = E_0 - 2t_1 \cos\left(k_x \frac{a_o}{2}\right) - 2t_2 \cos(k_x a_o), \qquad (1)$$

where $E_0$ is the isolated impurity energy, $t_1$ and $t_2$ are the first and second neighbor hopping parameters, closely related to the amount of overlap between the wavefunctions of neighboring impurities, and $a_0$ is the length of the **c**-axis vector for the m-$HfO_2$ primitive cell (5.296 Å). Fig. 4(e) shows the behavior of $t_1$ as the vacancy-vacancy distance varies, showing the expected exponential decay from which a localization parameter $\chi = 0.36a_0$ can be extracted. From the Mott criterion for metal-to-insulator transitions,[23] we can find that the critical vacancy concentration is $\sim 1.5 \times 10^{21}$ cm$^{-3}$, i.e., a local composition $HfO_{2-x}$ with $x = 0.05$ will be enough to enable the band transport mechanism.

This article is copyrighted as indicated in the article. Reuse of AIP content is subject to the terms at: http://scitation.aip.org/termsconditions. Downloaded to IP: 158.109.68.252 On: Wed, 23 Apr 2014 10:22:57

Fig. 4(f) shows how atomic-sized changes in the CF diameter bring out significant increases in the conductance. Specifically, we show the intrinsic conductance (i.e., without the effects of the metallic electrodes) for increasingly wider CFs. We remove one to three oxygen columns (see inset), observing that conductance increases stepwise for certain energy ranges, with each transmitting channel contributing a quantum of conductance $G_0$. This supports our interpretation that the observed quantization of the experimental data arises from few/single atom changes in the atomic structure of the CF. These results have to be taken qualitatively, as the model considered is simplified for a number of reasons (no metal contacts, zero bias conditions). However, we believe that they are able to capture the essential physics, namely that atomic size modifications of the structure of the CF will give rise to changes in the quantized conductance that are qualitatively consistent with the experimental observations.

In conclusion, atomic size effects have been reported during the reset of CFs in Pt/$HfO_2$/Pt structures. The existence of a rather stable CF intermediate state between the LRS and the HRS has been demonstrated. In this state, the CF behaves as a QW with conductance of the order of the quantum of conductance and the existence of preferred atomic-scale configurations has been revealed by conductance histograms. Our results indicate that the reset begins by a progressive narrowing of the CF towards the limit of one single-atom chain with conductance of about $G_0$. Then, a spatial gap is opened and the CF switches to the HRS, with its conductance dropping orders of magnitude. Thus, the quantum of conductance is a natural boundary between the LRS and HRS. The temperature dependence of the CF transport properties also confirm that the transition from metallic to temperature activated transport occurs for a CF conductance of the order of $G_o$. The study of the transport properties of oxygen vacancy paths using *ab-initio* methods shows that they are able to introduce band transport (as opposed to hopping transport) and support multiple transport channels with conductance $G_o$ related to increasing path width. Furthermore, increasing the distance between vacancies has been shown to exponentially decrease the hopping parameter. This indicates that opening a gap in these vacancy paths would decrease the CF conductance exponentially, as it is observed in the experimental transition to the HRS.

This work was funded by Spanish Ministry of Science and Technology under Contract TEC2012-32305 (partially supported by the EU under the FEDER Program), FIS2009-12721-C04-03, and CSD2007-00041, the DURSI of the Generalitat de Catalunya under Contract 2009SGR783, the Ministry of Science and Technology of China under Grant Nos. 2010CB934200, 2011CBA00602, 2009CB925003, 2011CB921804, 2011AA010401, and 2011AA010402, and the National Natural Science Foundation of China under Grant Nos. 61221004, 60825403, 61274091, 50972160, 61106119, and 61106082. J. Suñé also thanks the funding support of the ICREA ACADEMIA Award. Devices and data have been obtained in the frame of internal CEA-LETI research programs.

[1]R. Waser, R. Dittmann, G. Staikov, and K. Szot, Adv. Mater. **21**, 2632 (2009).
[2]M. Di Ventra and Y. V. Pershin, Mater. Today **14**, 584 (2011).
[3]I. K. Yoo, B. S. Kang, S. E. Ahn, C. B. Lee, M. J. Lee, G. S. Park, and X. S. Li, IEEE Trans. Nanotechnol. **9**, 131 (2010).
[4]D. H. Kwon, K. M. Kim, J. H. Jang, J. M. Jeon, M. H. Lee, G. H. Kim, X.-S. Li, G.-S. Park, B. Lee, S. Han, M. Kim, and C. S. Hwang, Nature Nanotechnology **5**, 148 (2011).
[5]I. Valov, R. Waser, J. R. Jameson, and M. N. Kozicki, Nanotechnology **22**, 254003 (2011).
[6]K. Szot, M. Rogala, W. Speier, Z. Klusek, A. Besmehn, and R. Waser, Nanotechnology **22**, 254001 (2011).
[7]D. Ielmini, R. Bruchhaus, and R. Waser, Phase Trans. **84**, 570 (2011).
[8]N. Agraït, A. Levy-Yeyati, J. M. van Ruitenbeek, Phys. Rep. **377**, 81 (2003).
[9]T. Schmidt, R. Martel, R. L. Sandstrom, and P. Avouris, Appl. Phys. Lett. **73**, 2173 (1998).
[10]E. Miranda, C. Walczyk, C. Wenger, and T. Schroeder, IEEE Electron Device Lett. **31**, 609 (2010).
[11]R. Degraeve, Ph. Roussel, L. Goux, D. Wouters, J. Kittl, L. Altimine, M. Jurczak, and G. Groseneken, Tech. Dig.-Int. Electron Devices Meet. **2010**, 632.
[12]J. Suñé, E. Miranda, M. Nafria, and X. Aymerich, Tech. Dig.-Int. Electron Devices Meet. **1998**, 191.
[13]J. R. Jameson, N. Gilbert, F. Koushan, J. Saenz, J. Wang, S. Hollmer, M. Kozicki, and N. Derhacobian, IEEE Electron Device Lett. **33**, 257 (2012).
[14]X. Zhu, W. Su, Y. Liu, B. Hu, L. Pan, W. Lu, J. Zhang, and R.-W. Li, Adv. Mater. **24**, 3941 (2012).
[15]S. Tappertzhofen, I. Valov, and R. Waser, Nanotechnology **23**, 145703 (2012).
[16]D. Ielmini, F. Nardi, and C. Cagli, Nanotechnology **22**, 254022 (2011).
[17]J. M. Soler, E. Artacho, J. D. Gale, A. García, J. Junquera, P. Ordejón, and D. Sánchez-Portal, J. Phys.: Condens. Mater. **14**, 2745 (2002).
[18]J. P. Perdew, K. Burke, and M. Ernzerhof, Phys. Rev. Lett. **77**, 3865 (1996).
[19]X. Zhao and D. Vanderbilt, Phys. Rev. B **65**, 233106 (2002).
[20]H. J. Monkhorst and J. D. Pack, Phys. Rev. B **13**, 5188 (1976).
[21]M. Brandbyge, J.-L. Mozos, P. Ordejón, J. Taylor, and K. Stokbro, Phys. Rev. B **65**, 165401 (2002).
[22]S.-G. Park, B. Magyari-Köpe, and Y. Nishi, Phys. Rev. B **82**, 115109 (2010).
[23]N. F. Mott, *Metal-Insulator Transitions*, 2nd ed. (Taylor & Francis, London, 1990).

This article is copyrighted as indicated in the article. Reuse of AIP content is subject to the terms at: http://scitation.aip.org/termsconditions. Downloaded to IP: 158.109.68.252 On: Wed, 23 Apr 2014 10:22:57

# Cycle-to-Cycle Intrinsic RESET Statistics in $HfO_2$-Based Unipolar RRAM Devices

Shibing Long, *Member, IEEE*, Xiaojuan Lian, Tianchun Ye, Carlo Cagli, Luca Perniola, Enrique Miranda, *Senior Member, IEEE*, Ming Liu, *Senior Member, IEEE*, and Jordi Suñé, *Fellow, IEEE*

***Abstract*— The statistics of the RESET voltage ($V_{RESET}$) and the RESET current ($I_{RESET}$) of Pt/$HfO_2$/Pt resistive random access memory (RRAM) devices operated under unipolar mode are analyzed. The experimental results show that both the distributions of $I_{RESET}$ and $V_{RESET}$ are strongly influenced by the distribution of initial resistance in the ON state ($R_{ON}$), which is related to the size of the conductive filament (CF) before RESET. By screening the statistical data into different resistance ranges, both the distributions of $I_{RESET}$ and $V_{RESET}$ are shown to be compatible with a Weibull model. Contrary to previous reports for NiO-based RRAM, the Weibull slopes of the $I_{RESET}$ and $V_{RESET}$ are demonstrated to be independent of $R_{ON}$. This is an indication that the RESET point, defined in this letter as the point of maximum current, corresponds to the initial phase of CF dissolution. On the other hand, given that the scale factor of the $V_{RESET}$ distribution ($V_{RESET63\%}$) is roughly independent of $R_{ON}$, the scale factor of the $I_{RESET}$ ($I_{RESET63\%}$) is inversely proportional to $R_{ON}$. This is analogous to what was found in NiO-based RRAM and it is consistent with the thermal dissolution model of RESET. Our results highlight the intrinsic link between the SET and RESET statistics and the need for controlling the variation of ON-state resistance to reduce the variability of the RESET voltage and current.**

***Index Terms*— RESET statistics, resistive random access memory (RRAM), resistive switching (RS).**

## I. Introduction

As a PROMISING candidate for next-generation non-volatile and storage-class memories, the resistive random access memory (RRAM), which is based on the resistive switching (RS) phenomenon in transition metal oxides, has been intensively investigated recently. The reasons for this interest are the simple structure of the devices, their good scalability, high speed, and good compatibility with silicon CMOS technology [1]–[4]. $HfO_2$ has been used in the gate dielectric stack of CMOS devices starting from the 32-nm technology node. Hence, it might be one of the most competitive RS functional materials for RRAM [5]–[8]. However, the wide cycle-to-cycle and cell-to-cell fluctuation of RS parameters such as the SET/RESET voltage and current, and the ON/OFF resistances still represent a significant barrier to engineer RRAM into large-scale commercial manufacturing [9]–[11]. In this letter, we present the characterization of the statistics of RESET voltage and current correlated to the statistics of ON-state resistance in $HfO_2$-based RRAM. The operation of these devices involves the creation and dissolution of a conductive filament (CF), likely related to oxygen vacancies.

Manuscript received September 9, 2012; accepted February 28, 2013. Date of publication April 3, 2013; date of current version April 22, 2013. This work was supported in part by Spanish Ministry of Science and Technology under Contract TEC2012-32305 (Partially funded by the European Union FEDER Program), the DURSI of the Generalitat de Catalunya under Contract 2009SGR783, the Ministry of Science and Technology of China under Grant 2010CB934200, Grant 2011CBA00602, Grant 2009CB930803, Grant 2011CB921804, Grant 2011AA010401, and Grant 2011AA010402 and the National Natural Science Foundation of China under Grant 61221004, Grant 61274091, Grant 60825403, Grant 61106119, and Grant 61106082. The review of this letter was arranged by Editor T. Wang.

S. Long, T. Ye, and M. Liu are with the Lab of Nanofabrication and Novel Devices Integration, Institute of Microelectronics, Chinese Academy of Sciences, Beijing 100029, China (e-mail: tcye@ime.ac.cn; liuming@ime.ac.cn).

X. Lian, E. Miranda, and J. Suñé are with the Departament d'Enginyeria Electròica, Universitat Autònoma de Barcelona, Bellaterra 08193, Spain.

C. Cagli and L. Perniola are with CEA, LETI, Grenoble F-38054, France.

Color versions of one or more of the figures in this letter are available online at http://ieeexplore.ieee.org.

Digital Object Identifier 10.1109/LED.2013.2251314

## II. Experimental Setup

Pt/$HfO_2$/Pt structures were fabricated with a 10-nm-thick $HfO_2$ RS layer deposited by atomic layer deposition at 350 °C. The Pt bottom (BE) and top (TE) electrodes were prepared by physical vapor deposition. TE was patterned by etching a square area of 1 $\mu m^2$. The RESET statistics were studied by cycling five individual devices for 1250 successive SET/RESET cycles each. Currents and voltages were measured by an Agilent 4155C semiconductor parameter analyzer which was also used to apply positive voltage ramp stress to the TE with the BE connected to ground. During the SET transition, a 1-mA current compliance limit was used to avoid the occurrence of hard dielectric breakdown, which would otherwise destroy the device.

## III. Results and Discussion

The fabricated Pt/$HfO_2$/Pt devices were operated in the unipolar mode. As shown in Fig. 1(a), the RESET point ($V_{RESET}$, $I_{RESET}$) is defined as the maximum of the RESET current [10], [11]. The raw voltage and current data were corrected by the series resistance $R_S$, which was estimated to be ∼28 Ω by adding the resistance of the experimental setup (∼18 Ω) to the Maxwell resistance, estimated to be ∼10 Ω for a CF with a diameter of ∼10 nm. After this correction, the RESET voltage $V_{RESET}$ appears to be rather independent of $R_{ON}$ [Fig. 1(b)], and the RESET current $I_{RESET}$ [inset of Fig. 1(b)] is inversely proportional to $R_{ON}$. This behavior is completely analogous to what was previously reported for NiO-based RRAM devices [10], [11] and it is compatible with the predictions of the thermal dissolution model of RESET [12], [13]. In this model, RESET is considered to occur by the out-diffusion of the conducting defects (i.e., oxygen vacancies) when the local CF temperature

0741-3106/$31.00 © 2013 IEEE

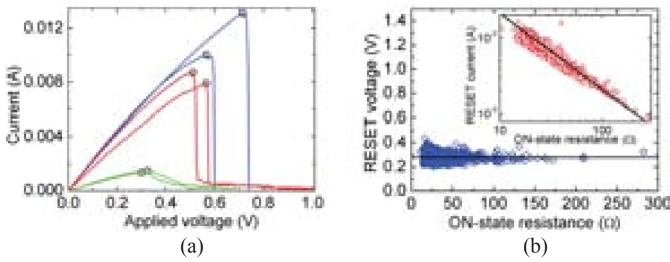


Fig. 1. (a) Six typical $I$–$V$ curves during dc RESET voltage sweeping of a Pt/HfO2/Pt device showing progressive RESET (green and red curves) and abrupt RESET (blue curves) events. The black circles represent the RESET points. (b) $V_{\mathrm{RESET}}$–$R_{\mathrm{ON}}$ and $I_{\mathrm{RESET}}$–$R_{\mathrm{ON}}$ (inset) scatter plots of the measured 1250 cycles of the same device after data correction by the series resistance $R_S = 28\ \Omega$.

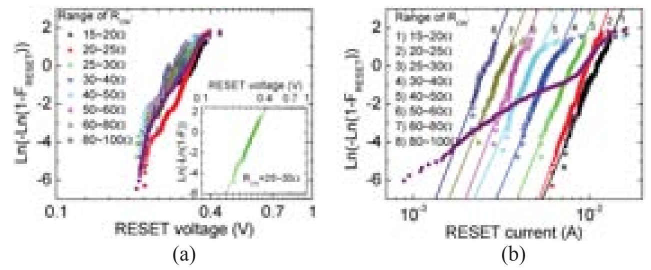


Fig. 2. Experimental distributions (symbols) of the same device and fitting of (a) $V_{\mathrm{RESET}}$ and (b) $I_{\mathrm{RESET}}$ to Weibull distributions (lines) as a function of $R_{\mathrm{ON}}$. The extreme $R_{\mathrm{ON}}$ ranges ($R_{\mathrm{ON}} < 15\ \Omega$ and $R_{\mathrm{ON}} > 100\ \Omega$) are not included in these plots because of the limited number of points which yield distorted distributions. The purple dots show the global distribution of $V_{\mathrm{RESET}}$ and $I_{\mathrm{RESET}}$ of all the 1250 cycles.

reaches a critical value $T_{\mathrm{RESET}}$. Taking into account the balance between Joule dissipation and heat evacuation, the basic equation of the model is $T_{\mathrm{RESET}} = T_0 + (R_{\mathrm{TH}}/R_{\mathrm{ON}})V_{\mathrm{RESET}}^2$, where $T_0$ is the operation temperature and $R_{\mathrm{TH}}$ is the thermal resistance describing heat dissipation from the CF to the environment [12], [13]. If $R_{\mathrm{ON}}$ is low enough, $R_{\mathrm{TH}} \propto R_{\mathrm{ON}}$ due to the Wiedemann–Franz law, and $V_{\mathrm{RESET}}$ is predicted to be independent of $R_{\mathrm{ON}}$, as found in our experiments [Fig. 1(b)]. $V_{\mathrm{RESET}}$ being independent of $R_{\mathrm{ON}}$, it follows that $I_{\mathrm{RESET}}$ is proportional to $1/R_{\mathrm{ON}}$, as found in the inset of Fig. 1(b).

Due to the statistical variation of $R_{\mathrm{ON}}$, we use a data screening method to get the $V_{\mathrm{RESET}}$ and $I_{\mathrm{RESET}}$ distributions in different $R_{\mathrm{ON}}$ ranges. Fig. 2 shows the global cumulative distribution of $V_{\mathrm{RESET}}$ and $I_{\mathrm{RESET}}$ together with the screened distributions for the different $R_{\mathrm{ON}}$ ranges. In both cases, the distributions have been displayed in the Weibull plot. Since the screened cumulative distributions are straight lines in these plots, we conclude that they are compatible with Weibull distributions. The Weibull distribution $F = 1 - \exp[-(x/x_{63\%})^{\beta}]$ is described by two parameters, the scale factor $x_{63\%}$, which is the value of the statistical variable at $F \approx 0.63$, and the shape factor or Weibull slope $\beta$, which measures the statistical dispersion (similar to the standard deviation in the normal distribution). If we compare the global distributions of $V_{\mathrm{RESET}}$ and $I_{\mathrm{RESET}}$ with the screened distributions, we find that the shape of the global distribution has nothing to do with the intrinsic dispersion of the RESET results. We have verified that if the screened distributions are combined with adequate statistical weights according to the number of samples in each resistance range, the original global cumulative distributions of $V_{\mathrm{RESET}}$ and $I_{\mathrm{RESET}}$ are nicely reproduced. This confirms the consistency of our screening method. In particular, the change of slope in the global $I_{\mathrm{RESET}}$ distribution is perfectly reproduced, thus emphasizing that the shape of this global distribution is fully controlled by the distribution of $R_{\mathrm{ON}}$. In fact, the change of slope is only related to the fact that the probability of finding $R_{\mathrm{ON}}$ within the two lowest resistance ranges (i.e., between 15 and 25 $\Omega$) is much higher than for higher $R_{\mathrm{ON}}$ values, because $I_{\mathrm{RESET}}$ decreases monotonically with $R_{\mathrm{ON}}$ and has a narrow spread in each $R_{\mathrm{ON}}$ value as shown in the inset of Fig. 1(b). According to these results, we can conclude that the shape of the global distributions of $V_{\mathrm{RESET}}$ and $I_{\mathrm{RESET}}$ does not provide useful insight about the intrinsic statistics of the RESET process unless we get rid of the variations of $R_{\mathrm{ON}}$. On the other hand, Fig. 2 demonstrates that a steep distribution of $I_{\mathrm{RESET}}$ can be obtained by

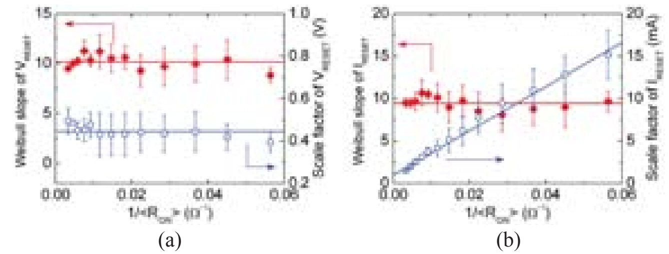


Fig. 3. $R_{\mathrm{ON}}$ dependence of the shape and scale factors of the (a) $V_{\mathrm{RESET}}$ and (b) $I_{\mathrm{RESET}}$ distributions of five different devices. The straight lines show the fitting results. $\langle R_{\mathrm{ON}} \rangle$ is the average of $R_{\mathrm{ON}}$ in each screening range. Each device shows the same trends between the shape/scale factors and $R_{\mathrm{ON}}$, that is, $\beta_V$, $\beta_I$, and $V_{\mathrm{RESET63\%}}$ are roughly constant, while $I_{\mathrm{RESET63\%}}$ is proportional to $1/R_{\mathrm{ON}}$. The five devices show a good reproducibility of the observed trends.

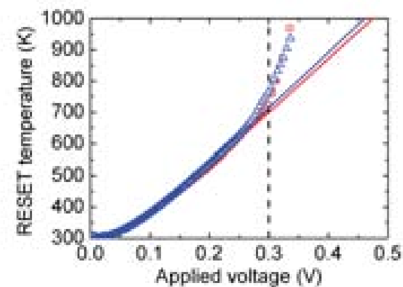


Fig. 4. Evolution of the experimental (circles and triangles) and theoretical RESET temperatures (continuous lines) of two RESET cycles in the $HfO_2$ device. The vertical dashed line indicates the same RESET applied voltage ($V_{\mathrm{app,RESET}} = 0.3$ V) obtained from the maximum current criterion.

adequately controlling the SET process to reduce the variability of $R_{\mathrm{ON}}$.

Fig. 3 shows that $V_{\mathrm{RESET63\%}}$ remains independent of $R_{\mathrm{ON}}$, while $I_{\mathrm{RESET63\%}}$ scales with $1/R_{\mathrm{ON}}$, as expected from the scatter plots of Fig. 1. On the other hand, the shape factors ($\beta_V$ and $\beta_I$) appear to be independent of $R_{\mathrm{ON}}$. Though the change of the scale factors of $V_{\mathrm{RESET}}$ and $I_{\mathrm{RESET}}$ distributions with $R_{\mathrm{ON}}$ is the same for both $HfO_2$ and NiO-based devices, the behavior of the shape factors is completely different because in the case of NiO, $\beta_V$ and $\beta_I$ were reported to scale with $1/R_{\mathrm{ON}}$ [10]. In [10], a physics-based model was proposed for the RESET statistics. This model implements the idea that in order to fully RESET the CF, out-diffusion of all the $N_{\mathrm{DEF}}$ defects that form the CF narrowest constriction bottleneck is required.

Here $N_{\mathrm{DEF}}$ is defined as $Nnn_{\mathrm{DEF}}$, with $N$ being the number of slices that composing the CF bottleneck, $n$ being the number of cells in each slice, and $n_{\mathrm{DEF}}$ the average number of defects in each cell. Departing from this idea, it was demonstrated that $\beta_V$ and $\beta_I$ should be proportional to $N_{\mathrm{DEF}} \propto 1/R_{\mathrm{ON}}$. This prediction was shown to be consistent with the results of NiO-based RRAM, but it is not consistent with the $HfO_2$ results reported in this letter. The reasons behind this discrepancy can be found by discussing the meaning of the RESET criteria and looking at the details of what happens before the RESET point. If there is no degradation of the CF before the RESET point, then the RESET event should be regarded as representing the initial step of the CF dissolution, that is, the out-diffusion of the first conductive defect from the CF bottleneck. In this case, a result like that reported for $HfO_2$ (i.e., $\beta_V$ and $\beta_I$ being independent of $R_{\mathrm{ON}}$) would be consistent with the model of [10]. To explore the degradation occurring in the CF prior to the RESET point, we designed a methodology based on calculating the maximum CF temperature by means of two different procedures [11]. First, we consider a linear temperature dependence of the CF typical of metallic behavior, that is, $R_{\mathrm{ON}}(T_{\mathrm{MAX1}}) = R_0[1 + \gamma\alpha(T_{\mathrm{MAX1}} - T_0)]$, where $R_0$ is the CF resistance at ambient temperature $T_0$, $\gamma$ is a geometrical parameter ($\gamma = 2/3$ for a cylindrical CF), and $\alpha$ is the experimental resistance-temperature coefficient. Using this equation, we can extract $T_{\mathrm{MAX1}}$ as a function of the applied voltage departing from the experimental evolution of $R_{\mathrm{ON}}$, that is, using the CF as a self-thermometer. That is why we denote $T_{\mathrm{MAX1}}$ as the experimental temperature. On the other hand, we can also calculate the evolution of the maximum temperature as a function of the applied voltage from the heat dissipation equation, that is, $T_{\mathrm{MAX2}} = T_0 + (R_{\mathrm{TH}}/R_{\mathrm{ON}})V^2$ where the $R_{\mathrm{TH}}/R_{\mathrm{ON}}$ ratio is assumed to be given by the Wiedemann–Franz law, that is, $R_{\mathrm{TH}}/R_{\mathrm{ON}} = (8\zeta L T_{\mathrm{MAX2}})^{-1}$, with $L = 2.45 \times 10^{-8}$ W$\Omega$/K$^2$ being the Lorentz number and $\zeta$ a fitting parameter that allows us to trim the thermal resistance so as to ensure that $T_{\mathrm{MAX1}} = T_{\mathrm{MAX2}}$ at low voltages, where all the conductance change is due to temperature effects. Since no experimental data are involved in the calculation of $T_{\mathrm{MAX2}}$, we have denoted it as the theoretical temperature. In the case of NiO, we concluded that significant degradation occurs before the RESET point, because these two temperatures diverge well before the maximum of the RESET current. In the present $HfO_2$-based devices, the results are quite different since, as shown in Fig. 4, the experimental and theoretical CF temperature curves nearly coincide before the RESET point ($V_{\mathrm{app,RESET}} = 0.3$ V, which corresponds to the maximum current). This means that, contrary to what was reported for NiO-based structures, in case of the present $HfO_2$-based devices, the RESET point nearly coincides with the starting point of the CF dissolution and the CF suffers little structural degradation before RESET, which explains the different behavior of $\beta_V$ and $\beta_I$ versus $R_{\mathrm{ON}}$.

## IV. Conclusion

The statistical distributions of RESET voltage and current in Pt/$HfO_2$/Pt RRAM devices were reported to be controlled by the distribution of initial CF resistance (i.e., by the ON-state resistance). Contrary to our previous report for NiO-based structures, the Weibull slopes of the RESET voltage and current distributions were found to be independent of the CF resistance, thus indicating that the RESET point captures the initial stage of the CF dissolution process. The dependence of the scale factors on $R_{\mathrm{ON}}$ was found to be consistent with the thermal dissolution model of unipolar RESET. An intrinsic connection between the SET and RESET statistics was reported, because the spread of the RESET current statistics was directly determined by the distribution of ON-state resistance. Hence, it was concluded that the control of the ON-state resistance distribution is of great importance in order to achieve good uniformity of the RESET parameters and good performance of RRAM.

## References


[1] R. Waser, R. Dittmann, G. Staikov, and K. Szot, “Redox-based resistive switching memories-nanoionic mechanisms, prospects, and challenges,” *Adv. Mater.*, vol. 21, nos. 25–26, pp. 2632–2663, Jul. 2009.

[2] H. Akinaga and H. Shima, “Resistive random access memory ReRAM based on metal oxides,” *Proc. IEEE*, vol. 98, no. 12, pp. 2237–2251, Dec. 2010.

[3] G. W. Burr, B. N. Kurdi, J. C. Scott, C. H. Lam, K. Gopalakrishnan, and R. S. Shenoy, “Overview of candidate device technologies for storage-class memory,” *IBM J. Res. Develop.*, vol. 52, nos. 4–5, pp. 449–464, Jul.–Sep. 2008.

[4] D. S. Jeong, R. Thomas, R. S. Katiyar, J. F. Scott, H. Kohlstedt, A. Petraru, and C. S. Hwang, “Emerging memories: Resistive switching mechanisms and current status,” *Rep. Progr. Phys.*, vol. 75, no. 7, p. 076502, Jun. 2012.

[5] Y. Wang, Q. Liu, S. Long, W. Wang, Q. Wang, M. Zhang, S. Zhang, Y. Li, Q. Zuo, J. Yang, and M. Liu, “Investigation of resistive switching in Cu-doped $HfO_2$ thin film for multilevel non-volatile memory applications,” *Nanotechnology*, vol. 21, no. 4, p. 45202, Jan. 2010.

[6] H. Y. Lee, Y. S. Chen, P. S. Chen, P. Y. Gu, Y. Y. Hsu, S. M. Wang, W. H. Liu, C. H. Tsai, S. S. Sheu, P. C. Chiang, W. P. Lin, C. H. Lin, W. S. Chen, F. T. Chen, C. H. Lien, and M. J. Tsai, “Evidence and solution of over-RESET problem for HfOX based resistive memory with sub-ns switching speed and high endurance,” in *Proc. IEEE Int. Electron Devices Meeting*, Dec. 2010, pp. 19.7.1–19.7.4.

[7] J. Lee, J. Shin, D. Lee, W. Lee, S. Jung, M. Jo, J. Park, K. P. Biju, S. Kim, S. Park, and H. Hwang, “Diode-less nano-scale ZrOx/HfOx RRAM device with excellent switching uniformity and reliability for high-density cross-point memory applications,” in *Proc. IEEE Int. Electron Devices Meeting*, Dec. 2010, pp. 452–455.

[8] C. Cagli, J. Buckley, V. Jousseaume, A. Salaun, H. Grampeix, J. F. Nodin, H. Feldis, A. Persico, P. Lorenzi, L. Massari, R. Rao, F. Irrera, T. Cabout, F. Aussenac, C. Carabasse, M. Coue, L. Perniola, P. Blaise, F. Zheng, Y. H. Yu, G. Ghibaudo, D. Deleruyelle, M. Bocquet, C. Müller, A. Padovani, O. Pirrotta, L. Vandelli, L. Larcher, G. Reimbold, and B. de Salvo, “Experimental and theoretical study of electrode effects in $HfO_2$ based RRAM,” in *Proc. IEEE Int. Electron Devices Meeting*, Dec. 2011, pp. 28.7.1–28.7.4.

[9] X. Guan, S. Yu, and H. S. P. Wong, “On the switching parameter variation of metal-oxide RRAM-Part I: Physical modeling and simulation methodology,” *IEEE Trans. Electron Devices*, vol. 59, no. 4, pp. 1172–1182, Apr. 2012.

[10] S. Long, C. Cagli, D. Ielmini, M. Liu, and J. Suñé, “Reset statistics of NiO-based resistive switching memories,” *IEEE Electron Device Lett.*, vol. 32, no. 11, pp. 1570–1572, Nov. 2011.

[11] S. Long, C. Cagli, D. Ielmini, M. Liu, and J. Suñé, “Analysis and modeling of resistive switching statistics,” *J. Appl. Phys.*, vol. 111, no. 7, pp. 074508-1–074508-19, Apr. 2012.

[12] U. Russo, D. Ielmini, C. Cagli, and A. L. Lacaita, “Self-accelerated thermal dissolution model for reset programming in unipolar resistive-switching memory RRAM devices,” *IEEE Trans. Electron Devices*, vol. 56, no. 2, pp. 193–200, Feb. 2009.

[13] D. Ielmini, C. Cagli, and F. Nardi, “Physical models of size-dependent nanofilament formation and rupture in NiO resistive switching memories,” *Nanotechnology*, vol. 22, no. 25, p. 254022, Feb. 2011.

# A Model for the Set Statistics of RRAM Inspired in the Percolation Model of Oxide Breakdown

Shibing Long, *Member, IEEE*, Xiaojuan Lian, Carlo Cagli, Luca Perniola,
Enrique Miranda, *Senior Member, IEEE*, Ming Liu, *Senior Member, IEEE,* and Jordi Suñé, *Fellow, IEEE*

***Abstract*— The set voltage distribution of Pt/$HfO_2$/Pt resistive switching memory is shown to fit well a Weibull model with Weibull slope and scale factor increasing logarithmically with the resistance measured at the set point. Gaining inspiration from the percolation model of oxide breakdown, a physics-based model for the $V_{set}$ statistics is proposed. The results of the model are completely consistent with the experimental results and demonstrate the need of a strong reset to get large Weibull slope that provides some relief to the strong requirements imposed by the set speed-read disturb dilemma.**

***Index Terms*— Resistive random access memory (RRAM), resistive switching, set voltage statistics.**

## I. Introduction

RESISTIVE random access memory (RRAM) based on the resistive switching (RS) of transition metal oxides is intensively investigated [1]–[3]. RS usually originates from the creation and rupture of a conductive filament (CF). The wide fluctuation of RS parameters is a major challenge for industrial application [4]. Understanding the statistics of the RS parameters and the underlying physical mechanisms is important for the effective control of the memory performance [5]. In this letter, we report the experimental set voltage statistics of a unipolar Pt/$HfO_2$/Pt device [6]. The shape and scale factor of the $V_{set}$ cumulative distribution are found to increase logarithmically with the resistance of the device measured at the $I(V)$ point at which the set transition occurs. Based on the percolation model of BD [7], we propose an analytical model for the $V_{set}$ distribution. A tunneling model for the CF conduction [8] is used to capture the correlation between the $V_{set}$ statistics and the CF resistance in the off-state.

Manuscript received May 14, 2013; accepted May 27, 2013. Date of publication July 3, 2013; date of current version July 22, 2013. This work was supported in part by the Ministry of Science and Technology of China under Grant 2011CBA00602 and Grant 2010CB934200, the National Science Foundation of China under Grant 61221004, Grant 61274091, Grant 60825403, Grant 61106119, and Grant 61106082, the Spanish Ministry of Science and Technology under Contract TEC2012-32305, and the DURSI of the Generalitat de Catalunya under Contract 2009SGR783. The review of this letter was arranged by Editor T. Wang.

S. Long and M. Liu are with the Laboratory of Nanofabrication and Novel Device Integration, Institute of Microelectronics, Chinese Academy of Sciences, Beijing 100029, China (e-mail: liuming@ime.ac.cn).

X. Lian, E. Miranda, and J. Suñé are with the Departament d'Enginyeria Electrònica, Universitat Autònoma de Barcelona, Bellaterra 08193, Spain (e-mail: jordi.sune@uab.es).

C. Cagli and L. Perniola are with Central Electricity Authority, Grenoble, Grenoble Cedex 9 F-38054, France.

Color versions of one or more of the figures in this letter are available online at http://ieeexplore.ieee.org.

Digital Object Identifier 10.1109/LED.2013.2266332

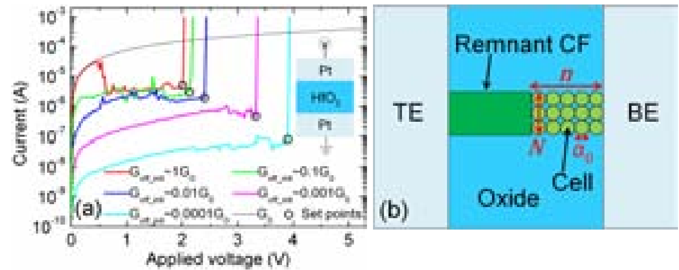


Fig. 1. (a) Typical set $I$–$V$ curves with different initial conductance $G_{off_init}$, with $G_0 \equiv 2e^2/h$ being the quantum of conductance. Inset: schematic structure of the Pt/$HfO_2$/Pt device. (b) Schematic representation of the partially broken CF after reset. The parameters of the cell-based set model are defined.

## II. Experimental Setup

On a Pt bottom electrode (BE), a 10-nm-thick $HfO_2$ RS layer is prepared by atomic layer deposition, followed by Pt top electrode (TE) deposition and patterning (see inset of Fig. 1). One thousand seven hundred fifty successive set/reset cycles with dc voltage sweep are applied to one of these devices with the bias voltage applied on the TE and the BE grounded. During the electroforming and the set operations, a compliance current of 1 mA is imposed. The device shows a nonpolar switching behavior. However, in this letter we focus only on the unipolar switching mode.

## III. Statistical Distributions of set Voltage

Fig. 1(a) shows the five typical set $I$–$V$ curves with different initial CF conductance. The black circles represent the set points at which the partially broken filament just begins to grow. The initial conductance strongly affects the current evolution in each set cycle. When it is very low, the conductance tends to gradually increase until an abrupt set occurs. On the contrary, when the initial conductance is high, some reset events are registered before the final abrupt set transition, and this corresponds to the partial dissolution of the CF. It is a fact that the competition between reset (out-diffusion of conductive defects from the CF) and set (diffusion of the conductive defects into the CF) processes always exists in each set/reset cycle [9]. As the information about the initial conductance of the CF is usually lost before the final set occurs, we use the off-resistance just at the set point for the analysis of the $V_{set}$ statistics. Thus, we define $R_{off} \equiv V_{set}/I_{set}$, with $I_{set}$ being the current just before the set current jump. $R_{off}$ is related to the CF size and shape just before the set transition and not at

0741-3106/$31.00 © 2013 IEEE

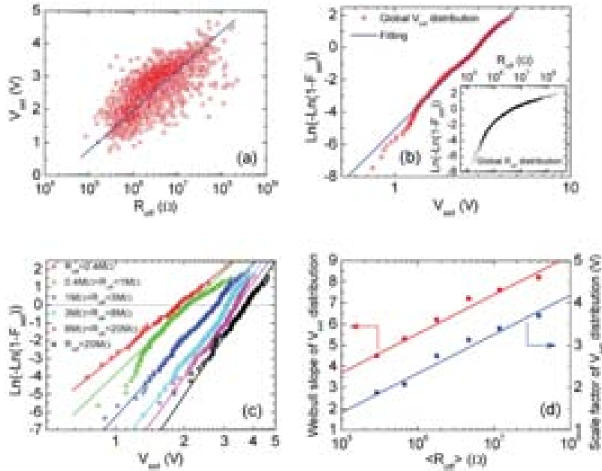


Fig. 2. Experimental statistics of $V_{\text{set}}$. (a) $V_{\text{set}} - R_{\text{off}}$ scatter plot during 1750 set/reset cycles. (b) Global cumulative distribution of $V_{\text{set}}$ (circles) and the linear fit to a Weibull distribution (line). Inset: cumulative distribution of $R_{\text{off}}$. (c) Decomposition of the $V_{\text{set}}$ distribution into six different $R_{\text{off}}$ ranges (dots) and the linear fit to Weibull distributions (lines). (d) The shape factor (red squares) and scale factor (blue circles) of the $V_{\text{set}}$ distribution versus $<R_{\text{off}}>$. $<R_{\text{off}}>$ is the geometric mean of $R_{\text{off}}$ in each resistance range.

the beginning of the set cycle. Fig. 2(a) shows the $V_{\text{set}} - R_{\text{off}}$ scatter plot corresponding to the 1750 cycles. The spread of $V_{\text{set}}$ for a fixed value of $R_{\text{off}}$ is smaller than the total statistical dispersion, thus allowing to reveal the increase of $V_{\text{set}}$ with $R_{\text{off}}$. The value of $R_{\text{off}}$ has a very wide statistical distribution [inset of Fig. 2(b)], and it has a strong influence on the global distribution of $V_{\text{set}}$. Thus, we need to use a resistance screening procedure to get partially rid of the $R_{\text{off}}$ variations and to study the intrinsic $V_{\text{set}}$ distribution. In particular, we have screened the $V_{\text{set}}$ data into six $R_{\text{off}}$ ranges hence to study the $V_{\text{set}}$ distribution as a function of $R_{\text{off}}$ [Fig. 2(c)]. Our experiments evidence that the global distribution of $V_{\text{set}}$ is strongly linked to the $R_{\text{off}}$ distribution and that both the Weibull slope and scale factor of the $V_{\text{set}}$ distribution increase logarithmically with $R_{\text{off}}$, as shown in Fig. 2(d).

## IV. An Analytical Model for Set Voltage Statistics

Considering that the set transition consists in the restoration of a partially broken CF, we claim that the cell-based percolation model for the oxide breakdown [7] can be easily adapted to model the set statistics of filament-based RRAM. Assuming that a partial filament survives after reset, the gap existing between the remaining CF and the opposite electrode will determine the set switching. Fig. 1(b) shows a schematic representation of the spatial gap, which appears between the CF stub and the counter electrode. However, our model formulation would be equally valid for a gap located in the middle of the CF. The gap area $A_{\text{CF}}$ is considered to be divided into $N$ columns with each one including $n$ cells. If this gap has a length $t_{\text{gap}}$, and we consider cubic cells with side $a_0$, then it follows that $N = A_{\text{CF}}/a_0^2$ and $n = t_{\text{gap}}/a_0$. In this letter, however, we will assume for simplicity that $N$ (i.e., the CF area) remains constant for all the set cycles and only $n$ changes from cycle to cycle. This simplification is justified by the fact that the gap resistance depends linearly on $N$ and exponentially on the gap length (i.e., on $n$), and so does the time to set (i.e., the BD of the oxide in the gap). Defining $\lambda$ as the probability of a cell being defective (i.e., conductive due to the presence of an oxygen vacancy, for instance), the cumulative probability of a column being defective is given by $P_{\text{col}} = \lambda^n$. The survival probability of the gap (i.e., the probability that the CF is not even partially reconstructed) is given by the survival of the whole set of $N$ columns:

$$1 - F_{\text{set}} = \left(1 - \lambda^n\right)^N \tag{1}$$

where $F_{\text{set}}$ is the set probability, i.e., the probability that at least one of the $N$ columns has all the $n$ cells defective. When $\lambda \ll 1$, the Weibit $W_{\text{set}} \equiv \text{Ln}\left[-\text{Ln}\left(1 - F_{\text{set}}\right)\right]$ can be approximated as follows:

$$W_{\text{set}} \cong \text{Ln}\left(N\right) + n\text{Ln}\left(\lambda\right). \tag{2}$$

Even if this is only strictly valid for $\lambda \ll 1$, it can be shown that this approximation is reasonable to deal with the experimental data for large enough $N$ ($>\sim 5$) and small enough $n$ ($<\sim 5$). To link the model and experiment, however, we need to relate $\lambda$ to measurable switching variables, such as $V_{\text{set}}$. Considering that $\lambda$ is proportional to the density of oxide defects and continuing with the analogy with oxide BD, the time evolution of $\lambda$ can be assumed to be $\lambda \sim \left(t/\tau_T\right)^\alpha$ under constant voltage stress conditions [7]. Here, $\alpha$ is a voltage-independent exponent that models the nonlinearity of the defect generation, and $\tau_T$ is a characteristic time which scales with the applied voltage according to a power law [10]

$$\tau_T\left(t\right) = \gamma_{T0}\left(V/t_{\text{gap}}\right)^{-m} \tag{3}$$

with $\gamma_{T0}$ and $m$ being constants. In the voltage ramp stress of interest to this letter, as the voltage changes with time as $V\left(t\right) = Rt$, the evolution of $\lambda$ is given by the following:

$$\lambda\left(t_{\text{set}}\right) = \left(\int_0^{t_{\text{set}}} \frac{1}{\tau_T\left(t\right)} dt\right)^\alpha. \tag{4}$$

Combining (2) to (4), we can obtain the following:

$$W\left(V_{\text{set}}\right) = \text{Ln}\left(N\right) + \left(m+1\right)\alpha n Ln\left\{\frac{V_{\text{set}}}{\left[\left(m+1\right)R\gamma_{T0}t_{\text{gap}}^m\right]^{\frac{1}{m+1}}}\right\} \tag{5}$$

which is a Weibull model for the distributions of $V_{\text{set}}$ with Weibull slope and scale factor given by the following:

$$\beta_V = \left(m+1\right)\alpha t_{\text{gap}}/a_0 \tag{6}$$

$$V_{63\%} \cong const \bullet R^{\frac{1}{m+1}}\left(t_{\text{gap}}\right)^{\frac{m}{m+1}} \tag{7}$$

respectively. The most important result is that $\beta_V$ is predicted to be proportional to $t_{\text{gap}}$. This model also predicts $V_{63\%}$ being proportional to $t_{\text{gap}}$ provided that $m$ is large ($m \sim 27$ is reported for the voltage acceleration of the time to set distributions in Ni/$HfO_2$/Si devices [11]). On the other hand, $t_{\text{gap}}$ can be directly related to $R_{\text{off}}$ provided that a model is assumed for the CF conduction. Several mechanisms are proposed for the CF conduction in the HRS including trap-assisted tunneling

[12], Poole–Frenkel conduction [13], [14] and space-charge limited current [15], hopping [16], [17], and so on. However, we will assume that tunneling through the gap potential barrier limits the conduction in the HRS [8], [12]. Since the tunneling transmission decreases exponentially with $t_{\text{gap}}$, we can write $R_{\text{off}} \cong \exp\left(t_{\text{gap}}/t_0\right)/(G_0 N)$, where $t_0$ is a characteristic barrier thickness. Thus, $t_{\text{gap}}$ is given by the following:

$$t_{\text{gap}}=t_0 \text{Ln}\left(G_0 N R_{\text{off}}\right). \tag{8}$$

Therefore, according to (5)–(8) our model predicts that both $\beta_V$ and $V_{63\%}$ linearly depend on Ln($R_{\text{off}}$), in perfect qualitative agreement with the experimental results of Fig. 2(d). Recent results also reported that the $V_{\text{set}}$ distribution of Ni/HfO$_2$/Si devices can be nicely described by a Weibull distribution [11]. In [11], a rather high $R_{\text{off}}$ ($\sim 10^8$–$10^9\,\Omega$), and a Weibull slope of $\sim$9.5 are reported. These results are also perfectly consistent with the $\beta(R_{\text{off}})$ straight line of Fig. 2(d) if it is extrapolated to their resistance range.

Trying to obtain more insight about the physics of the set statistics, we now assume that the CF consists of a bundle of vacancy paths and explore the application of our model to this dimensional scale. Recent *ab-initio* calculations showed that a single path of oxygen vacancies in $HfO_2$ supports a conduction channel with conductance $G_0$ and that the transmission probability is reduced by a factor of 10 for each reoxidized vacancy [18]. Thus, assuming $a_0 \sim 0.26$ nm, which is the separation of oxygen vacancies in monoclinic $HfO_2$, the value of $t_0$ can be estimated to be 0.12 nm. Subsequent fitting of the $\beta_V$ versus Ln ($R_{\text{off}}$) data to a straight line as in Fig. 2(d) allows obtaining $\alpha \sim 0.07$ and $N \sim 13$. This value of $\alpha$ is smaller than usually reported for the degradation of $HfO_2$ in gate oxide stacks, but values as small as 0.12 are also recently reported [19]. The value of $N$ is also reasonable as the CF conductance is found to change from an initial value of $\sim 500 G_0$ to a value of few times $G_0$ before the opening of the CF gap during the reset cycles. On the other hand, these parameters allow relating the experimental range of $R_{\text{off}}$ to a $t_{\text{gap}}$ range spanning from $\sim$0.26 to $\sim$1 nm, i.e., $n$ varying from 1 to 4. This gap is much smaller than the total oxide thickness (10 nm) and this might explain why the CF is likely to remain at the same location during RRAM cycling. Given that the set voltage corresponding to a gap of 1 nm is ~5 V, we can estimate the BD field of $\sim$50 MV/cm, which is much higher than usually reported for thin $HfO_2$ films. However, the BD field strongly increases when the thickness falls <1-nm range (a BD field of more than 30 MV/cm is measured for $Al_2O_3$ films of $\sim$1 nm [20]). In addition, the area of the stub is so small ($\sim$1 nm$^2$) that the weakest-link property of the BD might further justify a large BD field. Anyhow, any reasonable doubt raised by this result should only affect the implementation at the vacancy path scale and neither the model itself nor the derived conclusions.

## V. Conclusion

Both the shape and scale factor of the $V_{\text{set}}$ distribution of Pt/HfO$_2$/Pt device were found to increase logarithmically with $R_{\text{off}}$. An analytical cell-based model was proposed for the $V_{\text{set}}$ statistics of filament-type RRAM. Full qualitative agreement between the model and experiment was reported. Our results highlighted the importance of controlling the variations of $R_{\text{off}}$ to achieve a highly uniform distribution of set parameters. In addition, a strong reset was highly desirable to make the $V_{\text{set}}$ distribution had a large Weibull slope to meet the requirements imposed by the set speed-disturb tradeoff.

## References


[1] R. Waser, R. Dittmann, G. Staikov, *et al.*, "Redox-based resistive switching memories-nanoionic mechanisms, prospects, and challenges," *Adv. Mater.*, vol. 21, nos. 25–26, pp. 2632–2663, Jul. 2009.

[2] J. J. Yang, D. B. Strukov, and D. R. Stewart, "Memristive devices for computing," *Nature Nanotech.*, vol. 8, pp. 13–24, Jan. 2013.

[3] H.-S. P. Wong, H.-Y. Lee, S. Yu, *et al.*, "Metal oxide RRAM," *Proc. IEEE*, vol. 100, no. 6, pp. 1951–1970, Jun. 2012.

[4] S. Yu, X. Guan, and H.-S. P. Wong, "On the switching parameter variation of metal-oxide RRAM-Part II: Model Corroboration and device design strategy," *IEEE Trans. Electron Devices*, vol. 59, no. 4, pp. 1172–1182, Apr. 2012.

[5] S. Long, C. Cagli, D. Ielmini, *et al.*, "Reset statistics of NiO-based resistive switching memories," *IEEE Electron Device Lett.*, vol. 32, no. 11, pp. 1570–1572, Nov. 2011.

[6] C. Cagli, J. Buckley, *et al.*, "Experimental and theoretical study of electrode effects in HfO$_2$ based RRAM," in *IEDM Tech. Dig.*, 2011, pp. 658–660.

[7] J. Sunē, "New physics-based analytic approach to the thin-oxide breakdown statistics," *IEEE Electron Device Lett.*, vol. 22, no. 6, pp. 296–298, Jun. 2001.

[8] E. A. Miranda, C. Walczyk, C. Wenger, *et al.*, "Model for the resistive switching effect in HfO$_2$ MIM structures based on the transmission properties of narrow constrictions," *IEEE Electron Device Lett.*, vol. 31, no. 6, pp. 609–611, Jun. 2010.

[9] Y. Li, S. Long, H. Lv, *et al.*, "Reset instability in Cu/ZrO$_2$:Cu/Pt RRAM device," *IEEE Electron Device Lett.*, vol. 32, no. 3, pp. 363–365, Mar. 2011.

[10] A. Conde, C. Martínez-Domingo, D. Jiménez, *et al.*, "Modeling the breakdown statistics of Al$_2$O$_3$/HfO$_2$ nanolaminates grown by atomic-layer-deposition," *Solid-State Electron.*, vol. 71, pp. 48–52, May 2012.

[11] W.-C. Luo, K.-L. Lin, J.-J. Huang, *et al.*, "Rapid prediction of RRAM RESET-state disturb by ramped voltage stress," *IEEE Electron Device Lett.*, vol. 33, no. 4, pp. 597–599, Apr. 2012.

[12] S. Yu, X. Guan, and H.-S. P. Wong, "Conduction mechanism of TiN/HfOx/Pt resistive switching memory: A trap-assisted-tunneling model," *Appl. Phys. Lett.*, vol. 99, no. 6, p. 063507, Aug. 2011.

[13] D. Ielmini, C. Cagli, and F. Nardi, "Physical models of size-dependent nanofilament formation and rupture in NiO resistive switching memories," *Nanotechnology*, vol. 22, no. 25, p. 254022, May 2011.

[14] K.-C. Chang, T.-M. Tsai, T.-C. Chang, *et al.*, "Characteristics and mechanisms of silicon-oxide-based resistance random access memory," *IEEE Electron Device Lett.*, vol. 34, no. 3, pp. 399–402, Mar. 2013.

[15] H. Y. Lee, P.-S. Chen, T.-Y. Wu, *et al.*, "HfO2 bipolar resistive memory with robust endurance using AlCu as buffer electrode," *IEEE Electron Device Lett.*, vol. 30, no. 7, pp. 703–705, Jul. 2009.

[16] K.-C. Chang, C.-H. Pan, T.-C. Chang, *et al.*, "Hopping effect of hydrogen-doped silicon oxide insert RRAM by supercritical CO$_2$ fluid treatment," *IEEE Electron Device Lett.*, vol. 34, no. 5, pp. 617–619, May 2013.

[17] K.-C. Chang, R. Zhang, T.-C. Chang, *et al.*, "Origin of hopping conduction in graphene-oxide-doped silicon oxide resistance random access memory devices," *IEEE Electron Device Lett.*, vol. 34, no. 5, pp. 677–679, May 2013.

[18] X. Cartoixà, R. Rurali, and J. Suñé, "Transport properties of oxygen vacancy filaments in metal/crystalline or amorphous HfO$_2$/metal structures," *Phys. Rev. B*, vol. 86, no. 16, p. 165445, Oct. 2012.

[19] A. Kerber, A. Vayshenker, D. Lipp, *et al.*, "Impact of charge trapping on the voltage acceleration of TDDB in metal gate/high-k n-channel MOSFETs," in *Proc. Int. Rel. Phys. Symp.*, 2010, pp. 369–372.

[20] H. C. Lin, P. D. Yem, and G. D. Wilk, "Leakage current and breakdown electric-field studies on ultrathin atomiclayer-deposited Al$_2$O$_3$ on GaAs," *Appl. Phys. Lett.*, vol. 87, no. 18, p. 182904, Otc. 2005.

Solid-State Electronics xxx (2014) xxx–xxx

Contents lists available at ScienceDirect

Solid-State Electronics

journal homepage: www.elsevier.com/locate/sse

# Three-state resistive switching in $HfO_2$-based RRAM

Xiaojuan Lian [a,*], Enrique Miranda [a], Shibing Long [b], Luca Perniola [c], Ming Liu [b], Jordi Suñé [a]

[a] Departament d'Enginyeria Electrònica, Universitat Autònoma de Barcelona, 08193 Bellaterra, Spain
[b] Lab of Nanofabrication and Novel Device Integration, Institute of Microelectronics, Chinese Academy of Sciences, 100029 Beijing, China
[c] CEA, LETI, MINATEC Campus, 17 rue des Martyrs, F-38054 Grenoble Cedex 9, France

A R T I C L E I N F O

*Article history:*
Available online xxxx

The review of this paper was arranged by Prof. S. Cristoloveanu

*Keywords:*
Resistive switching
Quantum wire
RRAM
Non-voltatile memories

A B S T R A C T

We investigate the reset transition of $HfO_2$-based RRAM structures with emphasis on revealing three-state resistive switching effects. We study nonpolar switching in Pt/$HfO_2$/Pt and unipolar/bipolar switching in Pt/Ti/$HfO_2$/Pt structures, respectively. However, three-state resistive switching is only confirmed in the former case by means of various reset methodologies. Using two-step reset experiments it is shown that the transition to the complete reset state occurs at higher voltages if the CF first drops to the intermediate state.

© 2014 Elsevier Ltd. All rights reserved.

## 1. Introduction

Resistive Random Access Memories (RRAM), based on the resistive switching (RS) of transition metal oxide films (TMOs), such as NiO, $TiO_2$, CuO, $HfO_2$ and $ZrO_2$, is one of the viable candidates for future nonvolatile memory applications due to their good scalability, long endurance, fast switching speed, and ease of integration in the back end of the line of CMOS technology [1–3]. The operating principle of RRAM is based on the reversible resistive switching (RS) between at least two stable resistance states, the high resistance state (HRS) and the low resistance state (LRS). In most cases, the RS effect has its origin in the creation, dissolution and rejuvenation of conductive filaments (CF), and this is believed to involve the formation, migration and recombination of oxygen vacancies or metal ions. Among all kinds of TMOs, $HfO_2$ might be one of the most competitive RS functional materials for RRAM [4–7].

Understanding the physics of the RS phenomena is of great importance to control the performance, variability and reliability of these devices and to foster their real application as nonvolatile memories. In this regard, it is very important to reveal the nature of the CF, its conduction properties and the mechanisms which control its formation and disruption.

In this work, we focus on exploring the reset transition in $HfO_2$-based RRAM structures, with the main goal of investigating three-state resistive switching effects. Recent experiments of unipolar switching in Pt/$HfO_2$/Pt structures suggested the existence of an intermediate conduction state between the LRS and the HRS [8]. In this intermediate state, the CF was shown to behave roughly as a quantum wire (QW), showing conductance of the order of the quantum of conductance, $G_0 \sim 2e^2/h$. The idea that the CF in RRAM structures can be somehow understood as a QW was already at the basis of the quantum point contact (QPC) which, though originally developed for soft and hard breakdown conduction paths in thin-oxide MOS devices [9], was recently shown to adequately describe the conduction of the CF both in the LRS and the HRS of RRAM structures based on filamentary switching [10–12]. Moreover, experimental evidence of conductance quantization has also been shown recently, both in devices based on the formation of a metallic CF through a solid electrolyte [13–15] and in RRAM structures with $HfO_2$ as insulating material [8,16]. In the latter case, the CF is believed to be formed by oxygen vacancies and first-principle calculations have demonstrated the feasibility of oxygen-vacancy based CFs showing the properties of QWs [17].

To explore the phenomenology of three-state RS switching effects, we use different reset methodologies and explore both unipolar switching in symmetric Pt/$HfO_2$/Pt structures and unipolar/bipolar switching in asymmetric Pt/Ti/$HfO_2$/Pt devices. Only in the first case, which shows a much higher ON/OFF resistance ratio, three different states of the CF are revealed in the reset cycles. This confirms previous three-state resistive switching results and suggests that the structure of the CF at the microscopic level is different in these two types of structures. In the case of Pt/$HfO_2$/Pt structures, we also perform two-step reset experiments to show the impact of the intermediate state on the reset voltage and reset current statistical distributions.

* Corresponding author.
*E-mail address:* xjlian2005@gmail.com (X. Lian).

http://dx.doi.org/10.1016/j.sse.2014.04.016
0038-1101/© 2014 Elsevier Ltd. All rights reserved.

Please cite this article in press as: Lian X et al. Three-state resistive switching in $HfO_2$-based RRAM. Solid State Electron (2014), http://dx.doi.org/10.1016/j.sse.2014.04.016

ARTICLE IN PRESS



## 2. Experimental results

The structures of Pt/$HfO_2$/Pt and Pt/Ti/$HfO_2$/Pt with an area of 2.5 $\mu m^2$ were fabricated onto a tungsten plug, as shown in Fig. 1(a). The 10-nm-thick $HfO_2$ layer was deposited by atomic layer deposition (ALD) at 350 °C on the Pt bottom electrode (BE) prepared by physical vapor deposition (PVD), followed by the fabrication and pattering of the Pt or Pt/Ti top electrode (TE) using PVD and etching. The Pt/$HfO_2$/Pt structure shows a nonpolar behavior, which means that both the set and the reset transitions can be produced by positive or negative bias. In these structures, however, we only study in detail the case of unipolar switching (i.e. set and reset is achieved by electrical stress of the same polarity). Some typical examples of unipolar set/reset cycles are shown in Fig. 1(b). In the case of Pt/Ti/$HfO_2$/Pt structures, the switching behavior is significantly different. The device only shows reliable switching performance when the reset is operated in the negative polarity, i.e., the Pt/Ti electrode is the cathode in the reset switching, in agreement with recent results of other authors [18]. This is likely because the Ti acts as an oxygen extraction layer which introduces a strongly non-uniform profile of oxygen vacancies (more vacancies near the Ti/$HfO_2$ interface). In these structures, we will consider both the bipolar and the unipolar switching modes, as shown in Fig. 1(c) and (d), respectively. In all the experiments, the set transition was achieved by the application of a voltage ramp with a current compliance limit of 1 mA to avoid complete oxide breakdown. On the contrary, the reset transition was measured by three different electrical methods: constant-voltage stress (CVS), ramp-voltage sweep (RVS) and successive-voltage sweep (SVS) respectively. All the electrical measurements were performed with a Keithley 4200-SCS semiconductor characterization system.

### *2.1. Ramp-voltage sweep reset method in Pt/$HfO_2$/Pt and Pt/Ti/$HfO_2$/Pt structures*

Firstly, we consider the results of set/reset cycling experiments in which the reset was achieved by application of a ramp-voltage stress (RVS), which is the most widely used method for the investigation of the reset transition. These experiments have been performed in Pt/$HfO_2$/Pt structures operated in the unipolar RS mode and in Pt/Ti/$HfO_2$/Pt structures operated under unipolar and bipolar stress conditions. The measured I(V) characteristics during 125 successive RVS reset cycles applied to the Pt/$HfO_2$/Pt structure are shown in Fig. 2(a), as a representative example of the reset phenomenology under RVS method. In some cycles, this current drop is large enough to reach the HRS directly. In other cases, the drop is much smaller and it is followed by a more progressive reduction of the CF conductance. When the reset ramp finishes, two well defined bunches of conduction states are observed, one slightly above $G_0$ and another one below $\sim 0.1G_0$.

Inspired by the phenomenology observed in Fig. 2(a), we have performed longer cycling experiments consisting in the application of 1250 set/reset cycles on each RRAM device. The statistics of CF conductance measured at low voltage (0.1 V) before and after each reset cycle are presented in Fig. 2(b)–(d) for all the analyzed cases. Fig. 2(b) shows the conductance histogram for the unipolar reset experiment of Pt/$HfO_2$/Pt samples. While only one peak is observed before reset (the CF is highly conductive as corresponding to the LRS), three peaks are revealed after the reset cycle. One small peak overlaps the LRS peak, this meaning that in some cycles of the experiment, the CF did not suffer any reset. On the other hand, one broad peak is observed spanning several orders of CF conductance and with values below $0.1G_0$ [8]. This peak corresponds to the final HRS and, according to previous interpretations [20]; this state is related to a CF with a spatial gap. The CF gap introduces a potential barrier that limits the electron transmission through the filament and this is the reason why the conductance is strongly reduced below the $G_0$ boundary. In between the LRS and the HRS conductance peaks, there is another well-defined peak located just above $G_0$. This peak is associated to what we have called the intermediate QW state.

The Pt/Ti/$HfO_2$/Pt devices were operated both in the bipolar (positive set and negative reset) and the unipolar (set and reset under negative polarity) switching modes. The histograms of low-voltage conductance measured before and after set and reported

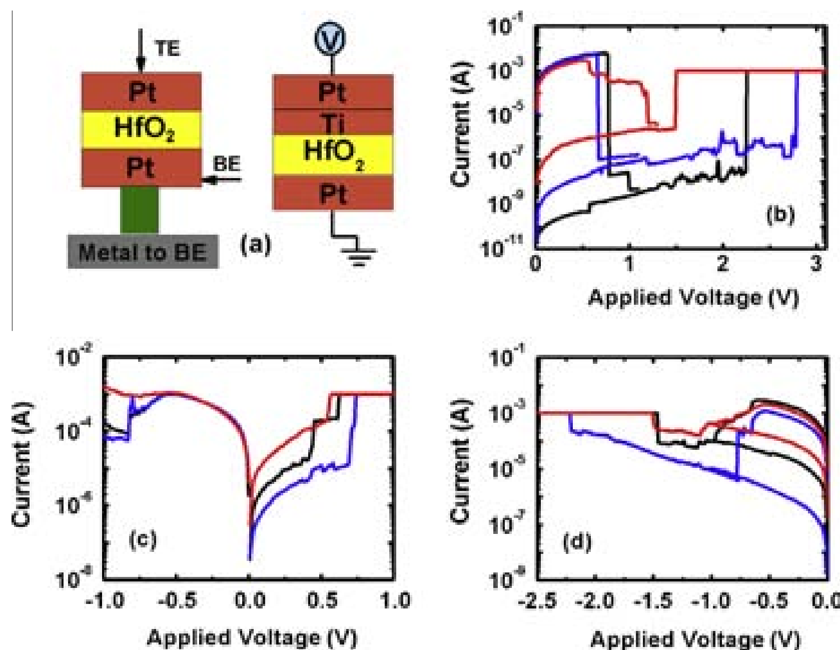


**Fig. 1.** (a) Schematic structure of the fabricated Pt/$HfO_2$/Pt and Pt/Ti/$HfO_2$/Pt devices. (b) Typical set/reset $I(V)$ curves measured in Pt/$HfO_2$/Pt structures operated under the unipolar switching mode. Typical set/reset $I(V)$ curves measured in Pt/Ti/$HfO_2$/Pt structures operated under bipolar (c) and unipolar (d) switching modes. A current compliance of 1 mA was always imposed during set to avoid destructive breakdown.

Please cite this article in press as: Lian X et al. Three-state resistive switching in $HfO_2$-based RRAM. Solid State Electron (2014), http://dx.doi.org/10.1016/j.sse.2014.04.016

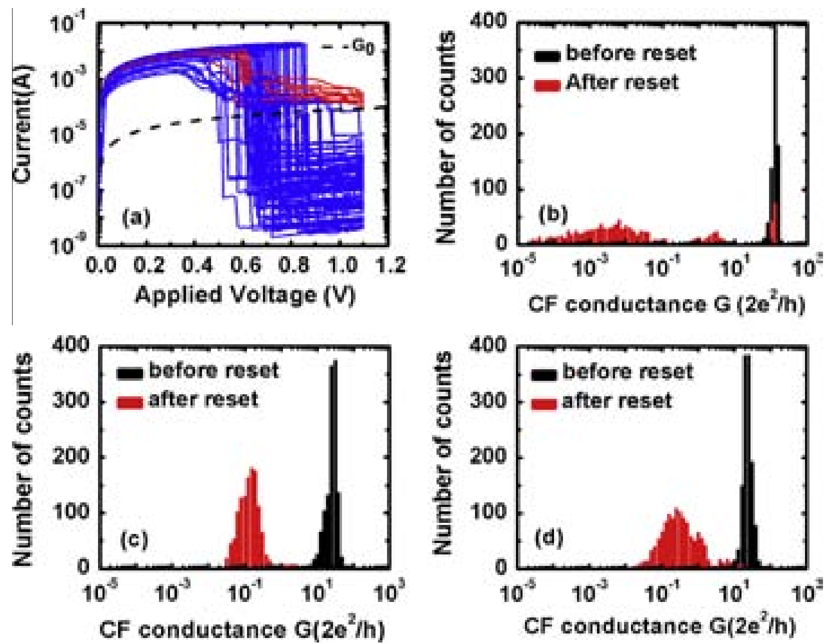


**Fig. 2.** (a) $I(V)$ curves measured during 125 reset cycles using ramped voltage stress method (from 0.1 V to 1.1 V). The results correspond to a Pt/$HfO_2$/Pt device stressed in the unipolar switching mode. The dashed line represents a linear $I(V)$ with conductance equal to the quantum of conductance $G_0$. Low-voltage (0.1 V) conductance histograms before and after each reset cycle are represented for long cycling experiments (1250 cycles each) in three different cases: (b) Pt/$HfO_2$/Pt unipolar switching; (c) Pt/Ti/$HfO_2$/Pt bipolar switching and; (d) Pt/Ti/$HfO_2$/Pt unipolar switching.

in Fig. 2(c) and (d), respectively. First we notice that the reset is much less effective than in the samples without Ti layer, in the sense that the conductance after reset is only at most slightly below $G_0$. The results obtained under bipolar and unipolar reset conditions are indeed very similar and only one big peak is observed after the reset. Since this peak is centered at approximately $0.1G_0$ and its tail reaches conductance values above $G_0$, we do not have evidence of the existence of the intermediate QW state in these structures. We believe that the differences in the reported conductance histograms reflect significant differences in the microscopic structure of the CF in both types of structures. We speculate that the CF might be rather symmetric in the case of unipolar switching of Pt/$HfO_2$/Pt structure with the most constrictive region being located near the middle of the filament (hourglass shape) where the higher temperature is reached and favors CF dissolution during reset. On the other hand, in the asymmetric Pt/Ti/$HfO_2$/Pt structure, the CF might be significantly wider at the Ti/$HfO_2$ interface (conical shape) due to the higher density of oxygen vacancies near this interface. This asymmetric CF might limit the extent to which the CF can be reset and make the observation of the intermediate QW state more difficult due to overlapping with the HRS state. Given these results, our study of the three-state RS effects has focused on the case of unipolar switching in Pt/$HfO_2$/Pt structures.

### 2.2. Three-state resistive switching using the successive-voltage sweep reset method

The transition from the LRS to the intermediate QW state can be controlled by applying successive-voltage ramps with increasing maximum voltage, as shown in Fig. 3. Although this technique allows a certain control of the reduction of the CF conductance when $G > G_0$, i.e. a control of the transition from the LRS to the intermediate QW state, the resistance of the final HRS is difficult to control. This is because in the HRS the CF conductance depends exponentially on the length of the spatial gap opened in the CF [20]. The successive-voltage sweep (SVS) experiment of Fig. 3 corresponds to a Pt/$HfO_2$/Pt structure subjected to unipolar switching

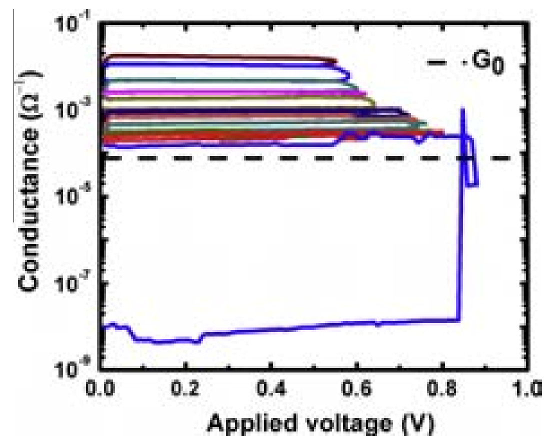


**Fig. 3.** SVS unipolar reset cycle applied to a Pt/$HfO_2$/Pt structure. By progressively increasing the maximum voltage, the conductance of the CF can be controlled down to a value close to $G_0$ (black line). When a gap is opened in the CF, an abrupt current drop of several orders of magnitude is registered, and the HRS state is reached.

conditions. In this experiment, the CF conductance is reduced from the initial value of $210G_0$ to $1.5G_0$ through the application of 10 successive-voltage sweeps with increasing maximum voltage. We speculate that this progressive reduction of conductance is achieved by making the CF progressively narrower. The last voltage sweep, however, disrupts the CF and opens a gap, thus decreasing its conductance by several orders of magnitude.

Given these results, we designed a 1250 cycles SVS experiment in which the set transition was achieved by a single RVS (positive bias) while each reset cycle consisted in the application of 10 successive-voltage ramps with increasing maximum voltage starting from 0.1 V and ending at 1.0 V with a linear increment step of 0.1 V. After each partial reset ramp, the voltage is swept back to 0 V and the CF conductance is measured at low voltage (0.1 V). With this method we obtain the statistical distributions of CF conductance as a function of the maximum partial reset voltage, as

Please cite this article in press as: Lian X et al. Three-state resistive switching in $HfO_2$-based RRAM. Solid State Electron (2014), http://dx.doi.org/10.1016/j.sse.2014.04.016

ARTICLE IN PRESS



shown in Fig. 4(a). Note that the conductance distribution remains nearly unchanged while the maximum reset voltage is kept below 0.6 V. Only a shoulder begins to appear at this voltage and this corresponds to the initial progressive transition from the LRS to the intermediate QW state. At $V_{MAX}$ = 0.7 V, the distribution already shows significant changes. In particular we can identify two plateaus which separate three steep regions which correspond to the LRS ($G/G_0 \sim 10^2$), the intermediate QW state ($0.1 < G/G_0 < 10$) and the HRS ($G/G_0 < 0.1$). For $V_{MAX}$ = 0.8 V and above, the LRS peak does not appear anymore and the distribution of conductance is bimodal. This means that reset has occurred in all the cycles. However, while a certain fraction of them have reached the HRS (full reset), in the majority of cases, a small CF remains as a QW connection between the electrodes. The histograms of CF conductance both before and after reset are shown in Fig. 4(b). Before the reset (i.e. after the application of the set voltage ramp), the device are in the LRS and the conductance shows a single peak around $100G_0$. After the complete application of the reset cycles, two clear peaks are distinguished. A large peak is located above $G_0$ and small amplitude peak is below $0.1G_0$. As in the case of the conventional RVS reset method, the first peak is interpreted as being associated to the intermediate QW state. On the other hand, the low-conductance peak is considered to correspond to the HRS. These results further support the existence of an intermediate QW state between the LRS and the HRS, confirming the results of the RVS reset experiment. Moreover, it is realized that under the softer stress conditions of SVS reset cycling, the transitions towards the QW state are strongly favored as compared to the direct transitions to the HRS. This indicates that the conductance of the final state after reset strongly depends on the details of the reset algorithm. To further investigate this issue, we have performed constant-voltage reset experiments under different voltages.

### 2.3. Unipolar reset of Pt/$HfO_2$/Pt structures under constant-voltage conditions

In this section, we study the reset phenomenology when the reset transition is achieved by means of a constant voltage stress in the Pt/$HfO_2$/Pt structures operating in the unipolar switching mode. The CVS reset mode mimics the fast reset (nanosecond scale) induced by the high voltage pulses which are required for practical RRAM applications. However, the stress voltages considered here are much smaller and the associated reset times are orders of magnitude longer (in the scale of hundreds of seconds). Under CVS conditions, the reset transition is registered as a sudden current drop in the time evolution of the current (or conductance), as shown in Fig. 5(a) and (b). In our experiments, the CVS stress voltage were varied from 0.5 V to 0.9 V and, between each CVS stress, a RVS was used to set the device back into its original LRS. Fig. 5(a) and (b) shows the conductance-time traces corresponding to two different CVS reset voltages. All the measured reset traces begin with a high conductance ($G \sim 100G_0$), as expected for the CF in the LRS. In the time scale of hundreds of seconds, all the reset $G(t)$ traces show one or more sudden drops which correspond to partial reset events which are related either to a reduction of the CF width or to the opening of a spatial gap in the filament. As we have already reported in the case of RVS and SVS, at the end of the stress experiment, two different types of CF states are distinguished and the CF conductance is either slightly above $G_0$ (i.e. the intermediate QW state) or down to orders of magnitude below the quantum of conductance, i.e. in the HRS. Again, these three-state RS phenomena are clearly revealed in the cumulative statistical distributions of conductance obtained for different stress times. To construct these distributions, all the reset cycles were considered and the cumulative probability $F(G)$ represented in Fig. 5(c), which is defined as the fraction of samples showing CF conductance smaller than $G$. In the distribution corresponding to the first current reading (labeled as $t$ = 0 s), almost 50% of the cycles had already shown some reset event. However, at the beginning of the reset cycle (i.e. just after the previous set transition), the device is always in the LRS. In consequence, in most of the cycles, the reset occurs very fast, during the duration of the first current measurement under the CVS. In the distributions corresponding to 0 s, 20 s and 200 s, two plateaus are found to separate three regions with $dF/dG > 0$. These conductance ranges correspond to the three states of the CF: the HRS, the intermediate QW state and the LRS. After 200 s of stress, the CF can only be found either in the HRS or the intermediate QW state.

The probability of the transition from the LRS to the intermediate QW decreases with the applied voltage and the fraction of cycles which end with the CF in the HRS increases. This is shown in Fig. 5(d) which shows the cumulative conductance probability corresponding to three CVS reset experiments performed at 0.55 V, 0.6 V and 0.8 V, respectively. From these results, it becomes evident that the higher is the stress voltage, the higher is the probability to fully reset the CF by creating a spatial gap. This indicates that the QW state might have negligible importance when the devices are operated under high voltage pulses. However, this issue should be further evaluated to determine whether the transition to the QW state can induce some kind of memory failure under realistic operation conditions even if with low probability. The impact of the transition to the intermediate QW state is further explored in the following section where the results of two-step reset experiments are reported. In any case, the results obtained under CVS reset conditions con-

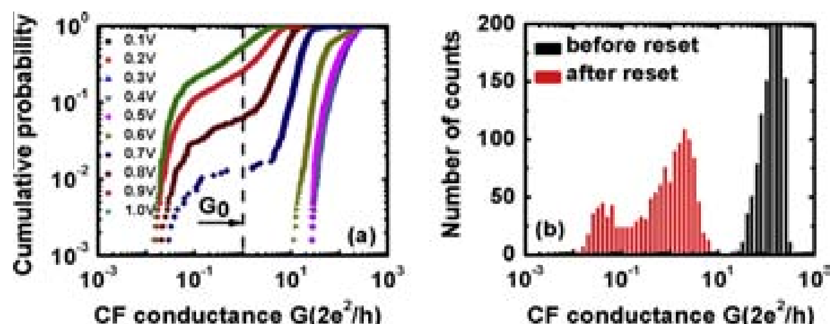


**Fig. 4.** (a) Distributions of CF conductance $G(2e^2/h)$ measured during 1250 cycles SVS reset experiment. The conductance was measured at low voltage (0.1 V) after the application of each reset voltage ramp with maximum voltage increasing from 0.1 V to 1.0 V. (b) The histograms of CF conductance $G(2e^2/h)$ measured at the end of each reset cycle during a SVS reset experiment consisting in 1250 cycles. In the LRS, the characteristic conductance peak is around $100G_0$. After the reset process, two clear peaks are distinguished. A large peak is located above $G_0$ and small amplitude peak is below $0.1G_0$.

Please cite this article in press as: Lian X et al. Three-state resistive switching in $HfO_2$-based RRAM. Solid State Electron (2014), http://dx.doi.org/10.1016/j.sse.2014.04.016

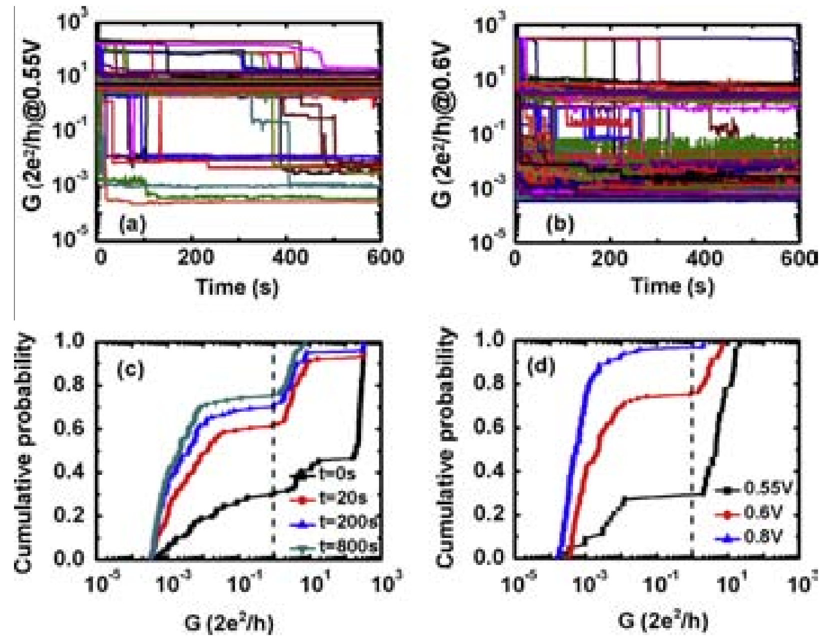


**Fig. 5.** Constant-voltage reset experiments corresponding to the unipolar switching mode of $Pt/HfO_2/Pt$ structures. (a) Conductance-time traces during a CVS reset at 0.55 V; (b) conductance-time traces during a CVS reset at 0.6 V; (c) cumulative distribution of conductance after different CVS stress times (at 0.6 V); (d) cumulative distribution of conductance after 600 s of stress under different voltages.

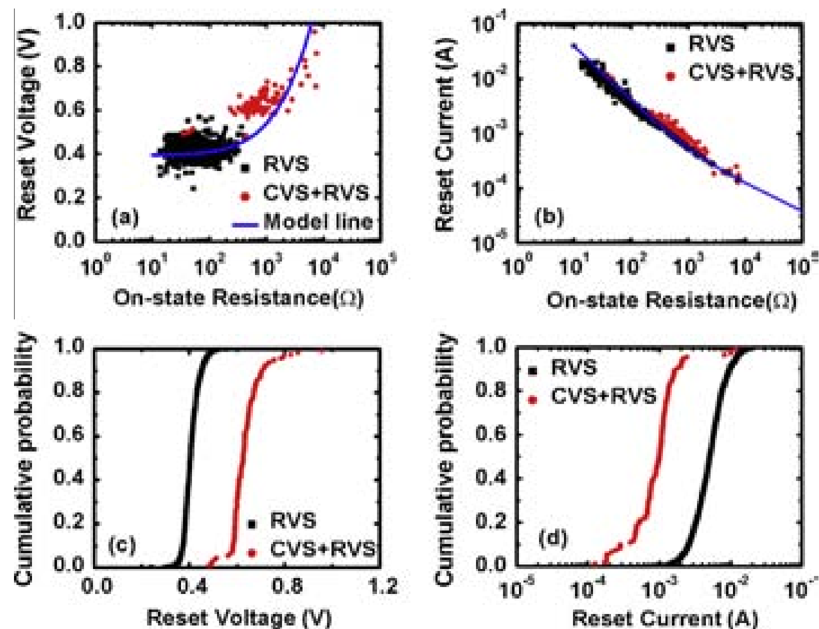


**Fig. 6.** Comparison of the results of a two-step reset experiment with those of a conventional RVS reset. The experiments were performed on the very same sample. The two-step reset method consists in an initial low-voltage CVS reset cycle (the CVS stress voltage is 0.55 V and the during time is 30 s) which induces the transition to the intermediate QW state with high probability and a subsequent VRS reset which is used to determine the distribution of reset voltage and current. (a) Scatter plot of the reset voltage versus the resistance of the CF in the LRS (at the beginning of the RVS step); the model line corresponds to a simple analytical thermal dissolution model [19]; (b) scatter plot of the reset current as a function of the CF resistance in the LRS; the model line correspond to the simple thermal dissolution model [19]; (c) cumulative distribution of reset voltage during the RVS reset cycle with and without the initial CVS phase; (d) cumulative distribution of reset current during the RVS reset cycle with and without the initial CVS phase.

firm the three-state switching phenomenology in $Pt/HfO_2/Pt$ structures operated in the unipolar switching mode.

Another conclusion that can be extracted from the results of CVS reset experiments is that the intermediate QW state is more stable than the initial LRS. This can be concluded from Fig. 5(a) and (b), where we notice that when the transition from the LRS to the QW state occurs, the transition to the final HRS is strongly suppressed. A detailed analysis of the evolution of the cumulative reset probability shown in Fig. 5(c) would also lead to the same conclusion. The higher stability of the QW state might be due to a reduction of energy dissipation in the CF constriction (ballistic transport through the CF and energy dissipation in the anode metal

electrode) but it can also be related to the fact that the reset voltage increases with the resistance of the CF. From the practical point of view, the enhanced stability of the QW state might cause reset failures because a transition from the LRS to the intermediate QW state might impede the ulterior transition to the final HRS. This issue is further explored in the following section by means of two-step reset experiments.

### 2.4. Two-step reset experiments of unipolar switching in Pt/$HfO_2$/Pt structures

In the previous section, we have concluded that the transitions to the intermediate QW state during reset experiments might reduce the probability of full reset of the CF to the HRS. To investigate this issue, we have designed two-step reset experiments consisting in a low-voltage CVS stage (0.55 V and 30 s) followed by a conventional RVS cycle. The goal of the initial CVS is to cause a transition from the LRS to the intermediate QW state in most of the samples. The final RVS reset properties are then compared with those obtained with an equivalent RVS reset experiment performed without the initial CVS. In this way, we obtain information about the impact of the QW state on the final transition to the HRS.

Fig. 6(a) and (b) shows the scatter plots of the final reset voltage (during the RVS) and final reset current, respectively. The impact of the initial CVS on the initial resistance of the CF is evident in these two figures. Except some cycles which remained in the LRS and showed CF initial resistances below 100 Ω, the rest of cycles suffered a transition from the LRS to the intermediate QW state and showed initial CF resistances well above this value and up to $10^4$ Ω. This increase of initial CF resistance causes an increase of the reset voltage and a decrease of the reset current which is shown to be compatible with the thermal dissolution of the CF [19], as shown by the model lines in Fig. 6(a) and (b). The same results can also be represented in Fig. 6(c) and (d) in the form of cumulative distributions of reset voltage and reset current, respectively. These two figures show how the reset voltages are increased while the reset current decreases. However, since the thermal dissolution process is voltage controlled (the voltage determines the local temperature and hence the rate of diffusion of oxygen species), we can conclude that the transition to the intermediate QW state increases the stress requirements for the full transition to the HRS. The decrease of the reset current is fully determined by the increase of CF resistance associated to the transition from LRS to intermediate QW state. The increase of the voltage required to fully reset the CF to the HRS in those cycles that suffer the transition to the QW state needs to be accounted in the design of the reset operation to avoid reset failures related to this issue. Notice that this works has demonstrated that the transitions to the QW state occur under any kind of reset methodology. It is true that the probability of these transitions to the QW state are strongly suppressed at the high stress voltages required for fast pulse RRAM operation. However, these should anyhow be considered to increase the reset yield to high percentiles.

## 3. Conclusions

The existence of a QW state has been demonstrated for the resistive switching CF in Pt/$HfO_2$/Pt devices. No clear evidence of this intermediate QW state is found in Pt/Ti/$HfO_2$/Pt operated under unipolar or bipolar conditions. This might be due to the much lower resistances of the HRS achieved in these structures, likely related to the asymmetric shape of the CF. Different methods have been used for the reset including RVS, CVS and SVS. In all cases, experiments support the three-state RS phenomenon. Three states are identified for the CF: (1) the LRS, which corresponds to a wide CF with metallic properties; (2) a partial reset state in which the CF behaves as a QW; and (3) the HRS, in which a physical gap has been opened in the CF. The probability of full reset (transition from LRS to HRS) has been reported to increase with the applied voltage but in all the reported experiments a significant fraction of the CFs remains in the QW state. It has also been demonstrated that the transitions from the LRS to the QW state increases the voltage required for the full reset of the CF. Thus, this issue needs to be taken into account when designing reset operation algorithms.

## Acknowledgments

This work was supported by the Spanish Ministry of Economy and Competitively under contract TEC2012-32305 (partially funded by the FEDER program of the EU), the DURSI of the Generalitat de Catalunya under contract 2009SGR783, the Ministry of Science and Technology of China under Grant 2010CB934200 and 2011CBA00602 and the National Natural Science Foundation of China under Grant 61221004 and 61274091. Jordi Suñé also acknowledges the ICREA Academia award. Devices and data have been obtained in the frame of internal CEA-LETI research programs.

## References

[1] Waser R, Dittmann R, Staikov G, Szot K. Redox-based resistive switching memories – nanoionic mechanisms, prospects, and challenges. Adv Mater 2009;21:2632.

[2] Ielmini D, Bruchhaus R, Waser R. Thermochemical resistive switching: materials, mechanisms, and scaling projections. Phase Trans 2011;84: 570–602.

[3] Kim KM, Jeong DS, Hwang ChS. Nanofilamentary resistive switching in binary oxide system; a review on the present status and outlook. Nanotechnology 2011;22:254007.

[4] Lin KL, Hou TH, Shieh J, Lin JH, Chou CT, Lee YJ. Electrode dependence of filament formation in $HfO_2$ resistive-switching memory. J Appl Phys 2011;109: 084104.

[5] Wang Y, Liu Q, Long S, Wang W, Wang Q, Zhang M, et al. Investigation of resistive switching in Cu-doped $HfO_2$ thin film for multilevel non-volatile memory applications. Nanotechnology 2010;21(4):45202.

[6] Lee HY, Chen YS, Chen PS, Gu PY, Hsu YY, Wang SM, Liu WH, Tsai CH, Sheu SS, Chiang PC, Lin WP, Lin CH, Chen WS, Chen FT, Lien CH, Tsai M-J. Evidence and solution of over-RESET problem for HfO*x* based resistive memory with sub-ns switching speed and high endurance. In: IEDM Tech. Dig.; 2010, p. 460–63.

[7] Cagli C, Buckley J, Jousseaume V, Salaun A, Grampeix H, Nodin JF, Feldis H, Persico A, Lorenzi P, Massari L, Rao R, Irrera F, Cabout T, Aussenac F, Carabasse C, Coue M, Perniola L, Blaise P, Zheng F, Yu Y, Ghibaudo G, Deleruyelle D, Bocquet M, Müller C, Padovani A, Pirrotta O, Vandelli L, Larcher L, Reimbold G, Salvo B de. Experimental and theoretical study of electrode effects in HfO2 based RRAM. In: IEDM Tech. Dig.; 2011, p.658–60.

[8] Long S, Lian X, Cagli C, Cartoixà X, Rurali R, Miranda E, et al. Quantum-size effects in hafnium-oxide resistive switching. Appl Phys Lett 2013;102:183505.

[9] Miranda E, Suñé J. Analytic modeling of leakage current through multiple breakdown paths in $SiO_2$ films. In: Proc. of the 39th IEEE Int. Rel. Phys. Symp; 2001, p. 367–79.

[10] Miranda E, Walczyk C, Wenger C, Schroeder T. Model for the resistive switching effect in $HfO_2$ MIM structures based on the transmission properties of narrow constrictions. IEEE Elect Dev Lett 2010;31:609–11.

[11] Degraeve R et al. Generic learning of TDDB applied to RRAM for improved understanding of conduction and switching mechanism through multiple filaments. Technical Digest of the IEEE International Electron Devices Meeting 2010:632–5.

[12] Lian X, Long S, Cagli C, Buckley J, Miranda E, Liu M, et al. Quantum point contact medel of filamentary conduction in resistive switching memories. Ultimate Integ Silicon(ULIS) 2012:101–4.

[13] Jameson JR, Gilbert N, Koushan F, Saenz J, Wang J, Hollmer S, et al. Quantized conductance in Ag/GeS2/W conductive-bridge memory cells. IEEE Elect Dev Lett 2012;33:257.

[14] Zhu X, Su W, Liu Y, Hu B, Pan L, Lu W, et al. Observation of conductance quantization in oxide-based resistive switching memory. Adv Mater 2012;2: 3941.

[15] Tappertzhofen S, Valov I, Waser R. Quantum conductance and switching kinetics of AgI-based microcrossbar cells. Nanotechnology 2012;23:145703.

[16] Long S, Gagli C, Cartoixà X, Rurali R, Miranda E, Jiménez D, Buckley J, Liu M, Suñé J. Conductance quantization in resistive switching in Frontiers in electronic materials. In: Nature Conference. Wiley-VCH; 2012, p. 257.

ARTICLE IN PRESS



[17] Cartoixà X, Rurali R, Suñé J. Transport properties of oxygen vacancy filaments in metal/crystalline or amorphous $HfO_2$/metal structures. Phys Rev B 2012;86: 165445.

[18] Gilmer DC, Bersuker G, Koveshnikov S, Jo M, Kalantarian A, Butcher B, et al. Asymmetry, vacancy engineering and mechanism for bipolar RRAM. In: Proc. of the 12th International MemoryWorkshop 2012:1–4.

[19] Ielmini D, Cagli C, Nardi F. Physical models of size-dependent nanofilament formation and rupture in NiO resistive switching memories. Nanotechnology 2011;22:254022.

[20] Long S, Lian X, Cagli C, Perniola L, Miranda E, Liu M, Suñé J. A model for the set statistics of RRAM inspired in the percolation model of oxide breakdown. IEEE Elect Dev Lett 2013;8(34):999–1001.

Please cite this article in press as: Lian X et al. Three-state resistive switching in $HfO_2$-based RRAM. Solid State Electron (2014), http://dx.doi.org/10.1016/j.sse.2014.04.016

# Multi-scale Quantum Point Contact model for filamentary conduction in RRAM devices

X. Lian [a], X. Cartoixà[a], E. Miranda[a], L. Perniola[b], R. Rurali[c], S. Long[d], M. Liu[d] and J. Suñé[a]

[a]Departament d'Enginyeria Electrònica, Universitat Autònoma de Barcelona, 08193-Bellaterra, Spain;

[b]CEA-LETI, MINATEC, Grenoble, France;

[c]Institut de Ciència de Materials de Barcelona (ICMAB-CSIC), Campus de Bellaterra, 08193-Bellaterra, Spain;

[d]Lab of nanofabrication and Novel Device Integration, Institute of Microelectronics, Chinese Academy of Sciences, Beijing, 100029, China.

**Abstract**

We depart from first-principle simulations of electron transport along paths of oxygen vacancies in $HfO_2$ to reformulate the Quantum Point Contact (QPC) model in terms of a bundle of such vacancy paths. By doing this, the number of model parameters is reduced and a much clearer link between the microscopic structure of the conductive filament (CF) and its electrical properties can be provided. The new multi-scale QPC model is applied to two different $HfO_2$-based devices operated in the unipolar and bipolar resistive switching (RS) modes. Extraction of the QPC model parameters from a statistically significant number of CFs allows revealing significant structural differences in the CF of these two types of devices and RS modes.

**Keywords:** Quantum Point Contact model, conductive filament, RRAM devices, resistive switching

## 1. Introduction

Resistive switching (RS) in metal-insulator-metal (MIM) or metal-insulator-semiconductor (MOS) devices is often based on the creation and partial destruction of a conductive filament (CF) of nanoscale dimensions[1-10]. Therefore, understanding the conduction properties of the CF in the Low-Resistance State (LRS) and the High-Resistance State (HRS) [11-17] and linking these properties to the shape and nature of the CF is of great importance to improve the understanding of RS and to boost Resistive Random Access Memories (RRAM) applications.

Many different conduction models have been proposed for the HRS including trap-assisted tunneling[18], Poole–Frenkel conduction[19], thermally activated hopping[20], space-charge limited current[21], and the Quantum Point Contact model (QPC) [22, 23], among others. Although the results might somehow depend on the considered oxide material, in the case of $HfO_2$ there are strong experimental evidences supporting the importance of tunneling in the HRS[18]. On the other hand, the experimental evidence of a CF behaving as a Quantum Wire (QW) in the LRS has been reported in a variety of RRAM devices, including $HfO_2$-based structures[24-29]. The single model which provides a smooth transition from tunneling in the HRS to Ohmic conduction in the LRS and which naturally explains conductance quantization effect is the QPC model. This model is based on the idea that the CF can be modeled as a QW, and it has been successfully applied to model the conduction properties in RRAM both in the HRS and the LRS[30-32].

The QPC model will be reformulated by coupling it to the results of first-principle simulations of oxygen vacancy paths. In this way, the number of model parameters is reduced and a much clearer link between the microscopic structure of the CF and its electrical properties can be provided. The multi-scale QPC model will be applied to two different $HfO_2$-based RRAM devices, $Pt/HfO_2/Pt$ and $Pt/Ti/HfO_2/Pt$ operated in the unipolar and bipolar RS modes.

## 2. The theoretical basis

### 2.1 First-principle simulation of $HfO_2$

Ab-initio calculations of the transport properties of metal/$HfO_2$/metal structures with paths of oxygen vacancies in hafnium oxide (Fig. 1(a)) have demonstrated the appearance of extended bands in the gap of $HfO_2$ (Fig. 1(b)) [27]. Using a Green's function formalism coupled with a density functional theory code, the conductance of vacancy filaments of different width was calculated[33-36], showing that even the narrowest filament (one vacancy path) can sustain a conductive channel, with conductance of the order of $G_0$[37]. On the other hand, as shown in Fig. 1(c), each time that a vacancy is removed from the single-vacancy filament, the conductance is reduced by a factor of ~10. Taking into account that the separation between vacancies is ~0.26 nm, the re-oxidation of a vacancy introduces a spatial gap in the filament which acts as a tunneling potential barrier of about this thickness. As a consequence, the conductance of the vacancy path (i.e. its barrier transmission coefficient) exponentially decreases with the gap thickness, $G = G_0 exp(-t_{gap}/t_0)$ with $t_0 = 0.12\ nm$, as shown in the Fig. 1(d).

Given these ab-initio results, the concept of CF narrowing is only meaningful when there are $N > 1$ vacancy paths. Further narrowing of the CF is not possible and the description of CF states with $G \ll G_0$ requires the existence of a spatial gap in the CF, i.e. at least one vacancy re-oxidized, which poses a potential barrier to electron transmission. Thus, the HRS will be described as a tunneling process through the CF gap, a process which is fully equivalent to that considered in Ref. 18.

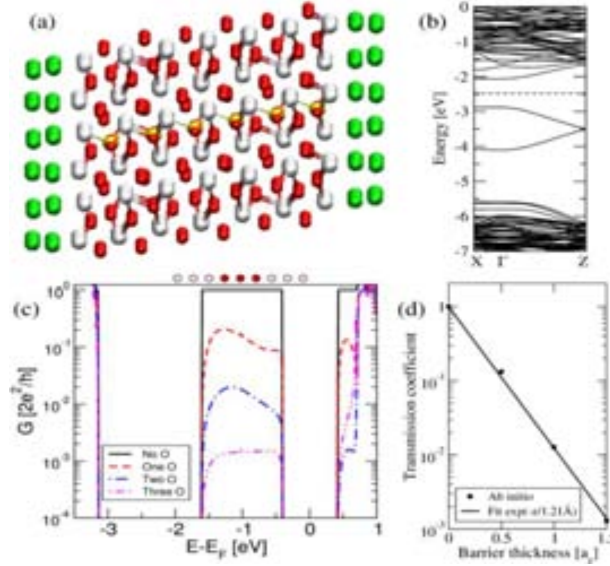

**Fig. 1** (a) Schematic representation of a single vacancy path (yellow balls) in monoclinic $HfO_2$, with green/red/white balls indicating metal/oxygen/hafnium atoms, respectively. (b) Band structure for the configuration of Fig.1 (a), without the metallic contacts, showing that the vacancy path introduces an extended band in the $HfO_2$. (c) Conductance associated to the extended band in the gap. When the vacancy filament is complete, conductance is $G_0$ and it is strongly suppressed when 1, 2, or 3 vacancies are removed (substituted by an oxygen atom). (d) The transmission coefficient as a function of the barrier thickness ($a_z$ is 0.52 nm, thus the separation between vacancies is ~0.26 nm) is reduced by a factor of ~10 when each vacancy is removed from the CF. Fitting line corresponds to $T = \exp(-t_{gap}/t_0)$ with $t_0 = 0.12\ nm$.

### 2.2 The multi-scale QPC model coupled to ab-initio results

The QPC model is based on the Landauer transmission approach to conduction along narrow microscopic constrictions and it assumes that the CF is a quasi-one dimensional system of electron states[38]. The area of the most constrictive section of the CF determines the energy of the subbands available for transport along the CF. If the CF is wide, the position of this first subband is below the electrode Fermi level and the conduction is essentially linear with a conductance of the order of $G_0 = 2e^2/h$ or larger. On the contrary, if the CF is narrow, the energy of the first subband might be above the electrode Fermi level and this would introduce a potential barrier which, depending on its height and thickness, might result in a CF conductance several orders of magnitude below $G_0$ and strongly non-linear I-V. This basic modeling framework has been assumed by different groups with some small different details. Miranda[30] has considered a bundle of $N$ of conducting single-subband CFs in the LRS and a single channel with a parabolic barrier in the HRS. Degraeve[31] described the filament as a saddle potential energy surface and extracted the model parameters from many reset I-V curves, thus providing evidence that the dominant microscopic evolution of the CF during reset consists in the progressive narrowing of the constriction. However, in this paper, we will keep the structure of Miranda's formulation of the QPC model.

According to the Landauer's approach, the current flowing through a CF with $N$ vacancy paths can be calculated as[39]:

$$I(V) = \frac{2e}{h} N \int_{-\infty}^{\infty} T(E)\{ f(E - \beta eV) - f(E + (1-\beta)eV)\}\ dE \quad (1)$$

where $E$ is the energy, $T(E)$ is the transmission probability, $f$ is the Fermi-Dirac distribution function, $e$ and $h$ are the electron charge and the Planck constant, and $V$ is the applied voltage which is assumed to drop at the cathode and anode interfaces with the QPC in a fraction of $\beta$ and (1- $\beta$ ), respectively (see Fig. 2).

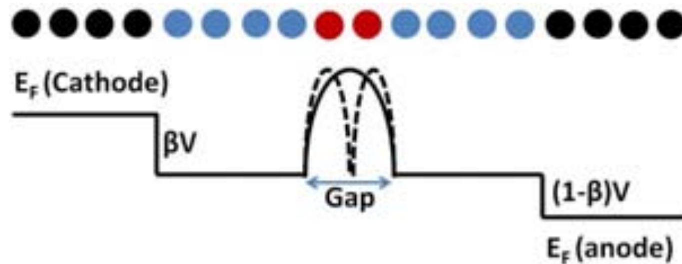


**Fig. 2** Schematic representation of a single vacancy path with two re-oxidized vacancies and the associated voltage profile under bias.

Assuming an inverted parabolic potential barrier allows to obtain an analytical expression for the tunneling probability[40-42], $T(E) = \{1 + exp[-\alpha(E - \Phi)]\}^{-1}$, where $\Phi$ is the barrier height and $\alpha = t_B\pi^2h^{-1}\sqrt{2m^*/\Phi}$ is related to the inverse of potential barrier curvature, $m^*$is the effective electron mass and $t_B$ is the barrier thickness at the equilibrium Fermi energy, assumed to be equal to $t_{gap}$. Inserting the transmission coefficient into Eq (1):

$$I = \frac{2e}{h} N \left\{ eV + \frac{1}{\alpha} Ln \left[ \frac{1+exp\{\alpha[\Phi-\beta eV]\}}{1+exp\{\alpha[\Phi+(1-\beta)eV]\}} \right] \right\} \tag{2}$$

This equation can be applicable to both the HRS and the LRS depending on the values of $\alpha$ and $\Phi$, which describe the potential barrier. If there is a gap with a potential barrier, this equation is found to converge to $I \approx NG_0\exp(-\alpha\Phi)V$ at low voltages so that the equivalent transmission probability is $T = \exp(-\alpha\Phi)$. Linking this to the thickness dependence obtained from the ab-initio results $T = \exp(-t_{\text{gap}}/t_0)$, we can obtain that $t_{gap} = t_0\alpha\Phi$ and $\Phi = 2\hbar^2/m^*\pi^2 t_0^2$. Assuming that $m^* \sim m_0$ (our ab-initio calculations give $m^* = 1.08\, m_0$ at the bottom of the one-vacancy electron band) results in a barrier height $\Phi \sim 1.16$ eV, which is a perfectly consistent value, given the large gap of $HfO_2$. In any case, other values of $m^*$ down to ~0.5 $m_0$ would give reasonable values of $\Phi$ below 2.5 eV and will not significantly affect the quality of the fit of the experimental I-V characteristics nor the extracted information about the microscopic structure of the CF. Finally, let us comment that in the limit that there is no spatial gap, Eq. (2) converges to $I = NG_0V$, a linear I-V which is consistent with what is usually observed in the LRS. When the CF is relatively narrow (small $N$), this equation explains the experimentally reported conductance quantization effects. For large values of $N$, the model approaches the classical Ohmic regime, where quantization becomes less evident because of the large values of CF conductance.

After reformulating the QPC model by coupling it to the results of ab-initio simulations of oxygen vacancy paths, only three free fitting parameters remain: the number of vacancy paths *N* (i.e. the lateral size of the CF) with the constraint $N \geq 1$, the average $t_{\text{gap}}$ in these paths (for simplicity all the paths are assumed to be identical) and the average value of the asymmetry parameter $\beta$, with the constraint $0 < \beta \leq 1$. However, in order to simplify the fitting process, we will usually assume a fixed value of $\beta$ and extract only *N* and $t_{\text{gap}}$ from the experimental data using Least-square-estimation (LSE) method.

In the following sections, experimental results are fit to the new multi-scale QPC model and the statistics of model parameters is reported. Fixing $\Phi = 1.16$ eV and $\beta = 0.5$ (symmetry) or $\beta = 1$ (asymmetry), we use Eq. (2) to fit the experimental I-V curves in HRS and LRS for $HfO_2$-based RRAM devices to get the values of *N* and α ($t_{\text{gap}}$). Finally, some indirect information about the microscopic structure of the CF will be discussed using the extracted QPC parameters and their evolution during set and reset transitions.

## 3. Results and discussion

Cycling experiments consisting of 1250 consecutive set/reset operations have been performed using the ramp voltage sweep (RVS) method in two different $HfO_2$-based RRAM structures, as shown in our recent paper[29]. In particular, we will study RS in $Pt/HfO_2/Pt$ operated in the unipolar mode (same polarity for set and reset) and $Pt/Ti/HfO_2/Pt$ structures operated under unipolar and bipolar switching modes. The considered structures are 2.5 $\mu m^2$ MIM capacitors fabricated in a mesa structure on top of a tungsten plug. The insulator is a 10-nm-thick $HfO_2$ layer deposited by atomic layer deposition (ALD) at 350 °C on top of the Pt bottom electrode (BE), followed by Pt (or Pt/Ti) top electrode (TE) deposition and patterning. BE and TE were deposited by physical vapor deposition (PVD). Electrical stress and measurements have been performed at the wafer level with a Keithley 4200SCS Semiconductor Characterization System. To initiate the RS behavior, an electroforming process is required to generate the CF. In all the cases, electroforming has been achieved by application of a voltage ramp with a current compliance of 1 mA (imposed by the measuring apparatus) so as to avoid the occurrence of hard breakdown, which would cause the device failure and impede any ulterior observation of RS. This compliance limit is also kept during each set cycle. During the reset voltage ramp, the current is allowed to flow without external limit.

### 3.1 Nonpolar $Pt/HfO_2/Pt$ devices

The $Pt/HfO_2/Pt$ devices are symmetric structures which show nonpolar RS, this means that $Pt/HfO_2/Pt$ devices can be set or reset by any combination of voltage bias (positive/positive; negative/ negative, positive/negative and vice versa). In all these operating modes, the RS phenomenology is very similar but the results considered in this paper correspond to unipolar RS mode, i.e. a positive bias voltage ramp is applied both for set and for reset. After each reset cycle and after each set cycle, the new QPC model parameters are extracted by the least-square fitting of I-V curves so as to get statistical information about the CF in the HRS and in the LRS. Notice that we focus on cycle-to-cycle variations of the CF and not on sample-to-sample variations. The CF conductance at low voltage is calculated by $R_{CF} = I/V$ at $V = 0.1\, V$ and a histogram of its distribution is shown in Fig. 3(a). In the LRS, the CF conductance peak is located at $\sim 100G_0$, while after reset two peaks of CF conductance are found: one narrow peak located between $G_0$ and $5G_0$ and a wide peak spanning from $10^{-5}G_0$ to $10^{-1}G_0$. In the LRS, the I-V curves are roughly linear with a small deviation from linearity at high currents, probably due to temperature dependent conductivity[43]. The QPC model can also be applied to the LRS ($I \approx N\beta G_0V$ in this limit) although the CF conductance is so large that the CF behaves essentially as a classical metallic wire. In this limit, the extracted number of conducting channels can be interpreted as being proportional to the area of the CF constriction.

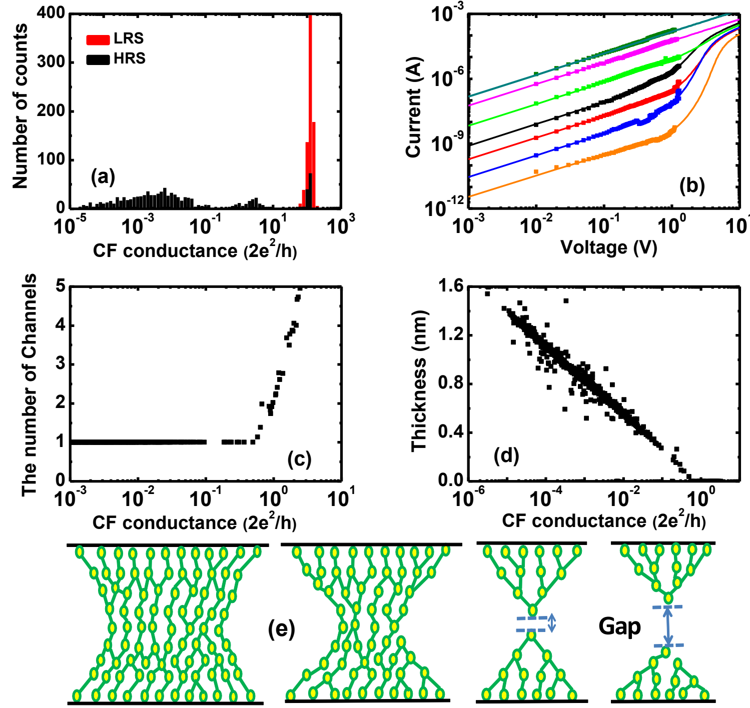


**Fig. 3** Nonpolar switching in Pt/$HfO_2$ /Pt structures. **(a)** Histogram of conductance @0.1V after set (red) and reset (black) cycles for 1250 successive set/reset cycles. **(b)** Examples of fitting of the I-V characteristics in the HRS. The CF conductance ranges from $G = 3.9e^{-5}G_0$ to $G{\sim}2G_0$. Extracted QPC model parameters**:** **(c)** number of conducting channels, i.e. number of single vacancy paths ($N$) versus CF conductance; and **(d)** thickness of the gap ($t_{\text{gap}}$) versus CF conductance. **(e)** Schematic representation of the CF structure evolution from the LRS to the HRS.

The analysis of the properties of the CF in the HRS for Pt/$HfO_2$/Pt structures provides enough useful information. As shown in Fig. 3(a) and Fig. 3(b), the HRS includes values of CF conductance spanning from slightly above $G_0$ down to$10^{-5}G_0$. A perfect I-V fitting is obtained in more than 5 orders of magnitude of conductance. When the CF conductance is of the order of $G_0$ or higher, the I-V is found to be linear, consistent with the idea that one or several oxygen vacancy paths connect the two electrodes through extended quasi-one dimensional electron subbands. For less conducting CFs, the I-V is found to be non-linear as the bias voltage increases. In general, the non-linearity increases with decreasing CF conductance and this corresponds to the tunneling regime. Fig. 3(c) and Fig. 3(d) show the extracted QPC model parameters which are only $N$ and $t_{\text{gap}}$ because $\beta = 0.5$ has been assumed for this structure and switching mode. This choice improves the quality of the I-V fitting and it is consistent with the symmetry of this RRAM structure. As shown in Fig. 3(c), for CF conductance below $G_0$, the best fit is obtained for $N = 1$, while for $G > G_0$ the number of conducting channels perfectly correlates with the CF conductance. On the other hand, Fig. 3(d) shows that there is no potential barrier for $G > G_0$ (i.e. $t_{\text{gap}} = 0$), and the thickness of the gap shows a perfect exponential correlation with the CF conductance below $G_0$, as expected for tunneling through a potential barrier. Thus, we conclude that below $G_0$, the CF has a very narrow constriction (likely one single oxygen vacancy path wide) with a spatial gap that ranges from 0 to 1.4 nm. This thickness range indicates that the gap can be estimated to be of up to ~6 re-oxidized vacancies in the least conductive CFs. Given that the CF conductance in the LRS is of the order of $10^2G_0$, the conductance ratio of LRS to HRS can be as large as $10^7$. This large change is achieved by combining the narrowing of the CF from ~267 vacancy paths (in the LRS) to one single path followed by the opening of a gap. Although the change of conductance is very large, it is concluded that the gap thickness (<1.4 nm) is only a small portion of the total CF length (10 nm). The long CF stumps that remain after each reset cycle explain why the spatial location of the CF likely remains the same along the very large number of set/reset cycles. This is because the probability of generating new CFs in different locations is much less favorable than the CF rejuvenation during the successive set cycles. According to the previous results, the evolution of the geometry of the CF from the LRS to the HRS is schematically depicted in Fig. 3(e). Starting from a very wide CF in the LRS, the first stage of the reset process consists in the reduction of the width of the CF in its most constrictive part to a limit in which only one or few oxygen vacancy paths connect the electrodes. This stage is followed by the opening of a gap, i.e. re-oxidation of one or several vacancies in all the paths. Once a gap is opened, the finding of $N = 1$ for $G < G_0$ means that the most conductive path controls the HRS I-V. In this regime (HRS), the thickness of the gap of the most conductive single vacancy path determines the CF conductance. In Fig. 3(e) we have assumed that the gap is in the center of the CF because the reset of these structures is likely due to thermal-enhanced dissolution and the center is likely the point of maximum temperature[44].

### 3.2 Bipolar Pt/Ti/$HfO_2$/Pt devices

In section 3.2 and section 3.3, the conductive properties of the CF in Pt/Ti/$HfO_2$/Pt devices will be analyzed. The structures include a thin Ti layer between the top Pt electrode and the $HfO_2$ layer. The Ti film is believed to act as an oxygen extraction layer and to introduce a high density of oxygen vacancies in the $HfO_2$. The vacancy profile is thought to

be rather asymmetric with a much higher concentration near the top interface. As a consequence, when a CF is created during forming, its shape is expected to be highly asymmetric, with the narrowest constriction near the bottom interface. In fact, due to this asymmetry, these structures only show reliable RS operation when negative bias is applied to the top electrode for reset. In other words, in agreement with previous works, RS is only possible by re-oxidation of the tip of the CF, i.e. when the bottom electrode is the reset anode[45]. Thus, these devices can be operated under two different RS modes: unipolar (negative set/negative reset) and bipolar (positive set/negative reset), provided that reset is achieved under negative polarity. Therefore, the properties of the CF in Pt/Ti/$HfO_2$/Pt devices, both under bipolar and unipolar RS operating are analyzed in the following sections.

Fig. 4(a) shows the histograms of CF conductance in the LRS and the HRS. In the case of Pt/$HfO_2$/Pt structures, the I-V in the LRS is essentially linear with a high voltage sub-linear behavior likely related to temperature-dependent conductivity. However, in this bipolar switching experiment, the CF conductance in the LRS is smaller ($\sim 30G_0$) although the compliance current during forming and set was kept at the same value (1mA). In the HRS, the CF conductance is found to be in the range between $5e^{-2}G_0$ and $2G_0$, i.e. the bipolar reset is much less effective than the unipolar one in the Pt/$HfO_2$/Pt structures, and hence, the resistance ratio of the HRS and the LRS is much degraded, as usually found for bipolar RS. Other significant differences are that, as shown in Fig. 4(b), all the I-V curves after reset are significantly nonlinear in spite of the CF conductance being close or above to $G_0$. On the other hand, the non-linearity is roughly independent of the CF conductance (the curves appear as almost parallel in the log-log plot). The fitting of the I-V curves to the QPC model is excellent, but the linear fit is not possible when $G > G_0$ nor it is possible to assume $N = 1$ for $G < G_0$, as explicitly shown in Fig. 4(c). In this particular case, the extraction of the QPC parameters ($N$ and $t_{gap}$) was done under the assumption that $\beta = 1$. This value gives the best fitting results and is consistent with the strong asymmetry of the CF shape in structures which contain an oxygen extraction layer. Fig. 4(d) show that the average gap thickness per conducting mode is found to converge to zero for $G/N \sim G_0$, as required by the QPC model.

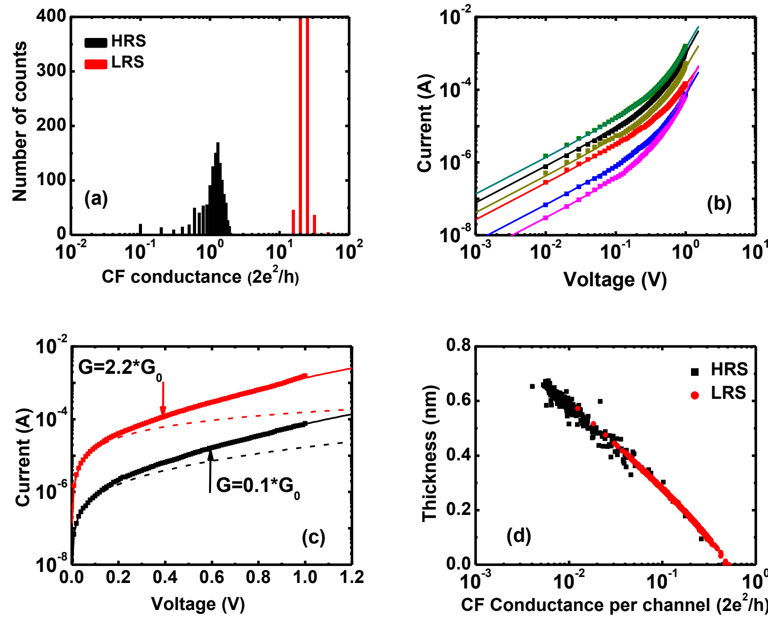


**Fig. 4** Application of the QPC model to Pt/Ti/$HfO_2$/Pt structures operated under bipolar RS conditions**. (a)** Distribution of CF conductance measured @0.1V in the LRS (red) and HRS (black) during bipolar cycling experiment. **(b)** Fitting of I(V) to the QPC model in the HRS. **(c)** Demonstration that fitting with N=1 (dashed black line) is not possible for low conductance CFs ($0.1G_0$) in the HRS nor it is possible to fit the I-V assuming linear conduction for $G>G_0$ (red dashed line) in the LRS. **(d)** Statistics of extracted QPC model parameters extracted from the fitting of 1250 I-V curves after the reset RVS in bipolar RS modes: gap thickness versus conductance per channel.

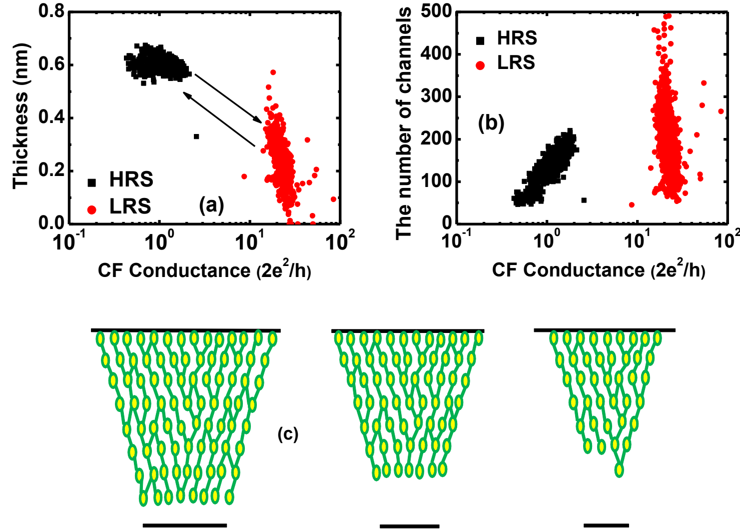


**Fig. 5** Statistics of extracted QPC model parameters extracted from the fitting of 1250 I-V curves after the reset RVS in bipolar RS modes. **(a)** Thickness of the gap versus CF conductance in the HRS and the LRS. **(b)** The number of conducting channels versus CF conductance both in the HRS and the LRS. **(c)** Schematic representation of CF structure in bipolar experiments.

Fig. 5(a) shows the extracted gap thickness versus CF conductance in the HRS and the LRS. We can see the average gap thickness is 0.59nm in the HRS and 0.25nm in the LRS; this is to say, there are about two or three re-oxidized vacancies in the HRS and one re-oxidized vacancy in the LRS. The number of CF paths versus conductance is shown in Fig. 5(b), which is different from what was found in the case of Pt/$HfO_2$/Pt structures. Many conduction paths are found to be active in the HRS but they show a gap with an average thickness corresponding to two or three vacancies. The average number of channels in the HRS and LRS is 134 and 192, respectively. According to the results of our analysis of properties by means of the reformulated QPC model, we can describe the evolution of the CF from the LRS to the HRS as shown in Fig. 5(c). Due to the asymmetry of the Pt/Ti/$HfO_2$/Pt structure, the CF is deduced to be conical with the tip contacting the bottom electrode being the active region during switching. In the LRS, the CF area is rather large (though smaller than in Pt/$HfO_2$/Pt structures) and there is one re-oxidized vacancy gap. In the HRS, and after a stabilization period of about 100 initial cycles, there is an average gap with the thickness of two or three vacancies and the CF conductance is modulated mainly by the area of the active CF tip.

### 3.3 Unipolar Pt/Ti/$HfO_2$/Pt devices

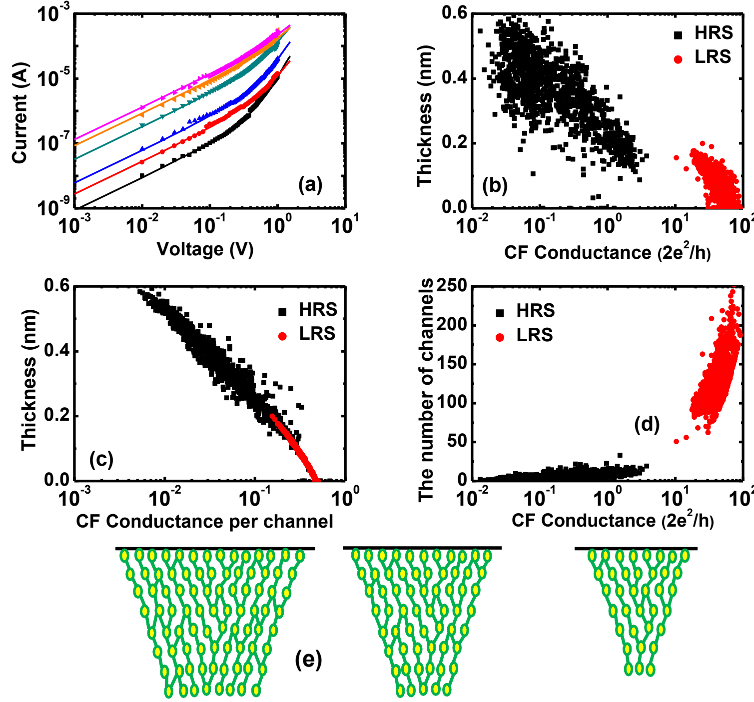


**Fig. 6** Application of the QPC model to Pt/Ti/$HfO_2$/Pt structures operated under unipolar RS conditions**. (a)** Fitting of I-V to the QPC model in the HRS. Statistics of extracted QPC model parameters extracted from the fitting of 1250 I-V curves after the reset RVS in

unipolar RS modes: **(b)** thickness of the gap versus CF conductance; and **(c)** gap thickness versus conductance per channel. **(d)** The number of conducting channels versus CF conductance. **(e)** The evolution of CF structure in unipolar experiments.

The experimental results of Pt/Ti/$HfO_2$/Pt devices in unipolar RS mode are different from bipolar RS mode, although the extraction of the QPC parameters ($N$ and $t_{\mathrm{gap}}$) was done under the assumption that $\beta = 1$ and $\Phi = 1.16$ eV. The CF conductance in the LRS (~$30G_0$) is similar to bipolar RS mode while in the HRS, the CF conductance is smaller than bipolar RS mode, which is found to be in the range between $10^{-2}G_0$ and $4G_0$, that is to say, the unipolar RS mode is more effective than bipolar RS mode for Pt/Ti/$HfO_2$/Pt devices, but it is much less effective than Pt /$HfO_2$/Pt devices. Fig. 6(a) shows the excellent I-V fitting in the HRS using LSE method. When the CF conductance is of the order of $G_0$ or higher, the I-V tends to be linear, consistent with the idea that one or several oxygen vacancy paths connect the two electrodes through extended quasi-one dimensional electron subbands. Fig. 6(b) to Fig. 6(d) shows the extracted QPC parameters versus CF conductance. The average gap thickness is about 0.09nm in the LRS and 0.356nm in the HRS and the average gap thickness per conducting mode is found to converge to zero for $G/N \sim G_0$, as required by the QPC model. The average number of paths is about 130 in the LRS and 5 in the HRS. Therefore, the number of conductance channels decreases and a gap is opened that is about two re-oxidized vacancies from the LRS to the HRS. Finally, Fig. 6(e) schematically shows the evolution of the microscopic structure of the CF in Pt/Ti/$HfO_2$/Pt devices when the evolution from the LRS to the HRS during unipolar RS mode. In the LRS, there are many conductive filaments and very small thickness gap between two electrodes. Then the CF is narrowing and opening about two re-oxidized vacancies gap in the HRS.

## 4. Conclusions

The QPC model has been applied to a thorough statistical study of resistance switching in RRAM devices. The fitting of I-V characteristic is excellent in both HRS and the LRS for two different structures in three RS modes. After reformulating the QPC model for CF conduction by coupling it to the results of ab-initio simulations of oxygen vacancy paths, we can obtain indirect information about the microscopic structure of the CF in both Pt/$HfO_2$/Pt and Pt/Ti/$HfO_2$/Pt devices. For Pt/$HfO_2$/Pt devices, the CF is symmetric with the most constrictive part likely located in the center of the CF. Starting from a very wide CF in the LRS, the width of the CF in its narrowest part reduces to a limit where only one or few oxygen vacancy paths connect the electrodes. This stage is followed by the opening of a gap that the thickness of the most conductive single vacancy path determines the CF conductance in the HRS. For Pt/Ti/$HfO_2$/Pt devices, the CF is strongly asymmetric, with the narrowest constrictive part near the bottom interface. The CF is deduced to be conical with the tip contacting the bottom electrode being the active region during switching. The Ti film is believed to act as an oxygen extraction layer and to introduce a high density of oxygen vacancies in the $HfO_2$. In the LRS, the CF area is rather large and there is one re-oxidized vacancy gap for bipolar RS mode, then the gap increases to two or three vacancies and the CF is narrower than the LRS. For unipolar RS mode, the number of paths in the HRS is much less than bipolar RS mode, this is to say, the unipolar RS mode is more effective than bipolar RS mode. The obtained results have revealed significant differences in the properties of the CF in these two types of devices. This is consistent with the expected differences in the concentration profile of oxygen vacancies due to the presence/absence of an oxygen extraction layer.

## Acknowledgments

This work was supported by the Spanish Ministry of Economy and Competitively under contract TEC2012-32305, FIS2012-37549-C05-05, and CSD2007-00041 (partially funded by the FEDER program of the EU), the DURSI of the Generalitat de Catalunya under contract 2009SGR783, and the National Natural Science Foundation of China under Grant 61322408, 61221004 and 61274091. Jordi Suñé also acknowledges the ICREA Academia award. Devices and data have been obtained in the frame of internal CEA-LETI research programs.

## Reference

1. R. Waser and M. Aono, Nat. Mater., 2007, **6**, 833.
2. A. Sawa, Materials Today, 2008, **11**, 28.
3. R. Waser, R. Dittmann, G. Staikov, and K. Szot, Adv. Mater. 2009, **21**, 2632.
4. D. Ielmini, R. Bruchhaus and R. Waser, Phase Transitions, 2011, **84**, 570.
5. J. J. Yang, D. B. Strukov, D. R. Stewart, Nat. Nanotechnol. 2013, **8**, 13.
6. D. S. Jeong, R. Thomas, R. S. Katiyar, J. F. Scott, H. Kohlstedt, A. Petraru, C. S. Hwang, Rep. Prog. Phys. 2012, **75**, 076502.
7. K. M. Kim, D. S. Jeong, and C. S. Hwang, Nanotechnology, 2011, **22**, 254002.
8. H.-S. P. Wong, H.-Y. Lee, S. Yu, Y.-S. Chen, Y. Wu, P.-S. Chen, B. Lee, F. T. Chen, M.-J. Tsai, Proc. IEEE, 2012, **100**, 1951.
9. S. C. Chae, J. S. Lee, S. Kim, S. B. Lee, S. H. Chang, C. Liu, B. Kahng, H. Shin, D.-W. Kim, C. U. Jung, S. Seo, M.-J. Lee, and T. W. Noh, Adv. Mater., 2008, **20**, 1154.
10. Y. C. Yang, P. Gao, S. Gaba, T. Chang, X. Pan, W. Lu, Nat. Commun. 2012, **3**, 732.
11. C. Cagli, F. Nardi, and D. Ielmini, IEEE Trans. Electron Devices, 2009, **56**, 1712.
12. S. Long, Q. Liu, H. Lv, Y. Li, Y. Wang, S. Zhang, W. Lian, K. Zhang, M. Waong, H. Xie, and M. Liu, Appl. Phys. A, 2011, **102**, 915.
13. W. Guan, M. Liu, S. Long, Q. Liu, and W. Wang, Appl. Phys. Lett., 2008, **93**, 223506.
14. S. Yu and H.-S. P. Wong, IEEE Trans. Electron Devices, 2011, **58**, 1352.
15. S. Lavizzari, D. Ielmini and A. L. Lacaita, IEEE Trans. Electron Devices. 2010, **57**, 3257.
16. J. S. Lee, S. B. Lee, S. H. Chang, L. G. Gao, B. S. Kang, M.-J. Lee, C. J. Kim, T. W. Noh, and B. Kahng, Phys. Rev. Lett., 2010, **105**, 205701.
17. H. D. Lee, B. Magyari-Köpe, and Y. Nishi, Phys. Rev. B,2010, **81**, 193202.
18. S. Yu, X. Guan, and H.-S. P. Wong, Appl. Phys. Lett, 2011, **99**, 063507.
19. D. Ielmini, F. Nardi and C. Cagli, Nanotechnology, 2011, **22**, 254022.
20. D. Ielmini, IEEE Trans. Electron Devices, 2011, **58**, 4309.
21. H. Y. Lee, P.-S. Chen, T.-Y. Wu, Y. S. Chen, F. Chen, C.-C. Wang, P.-J. Tzeng, C. H. Lin, M.-J. Tsai, and C. Lien, IEEE Electron Device Lett, 2009, **30**, 703.

22. J. Suñé, E. Miranda, M. Nafria and X. Aymerich, Techn. Dig. of the IEEE Int. Electron Devices Meeting, 1998, **191**.
23. J. Suñé and E. Miranda, Techn. Dig. of the IEEE Int. Electron Devices Meeting, 2000, **533**.
24. J. R. Jameson, N. Gilbert, F. Koushan, J. Saenz, J. Wang, S. Hollmer, M. Kozicki, and N. Derhacobian, IEEE Elect. Dev. Lett, 2012, **33**, 257.
25. X. Zhu, W. Su, Y. Liu, B. Hu, L. Pan, W. Lu, J. Zhang, and R.-W. Li, Adv. Mater, 2012, **24**, 3941.
26. S. Tappertzhofen, I. Valov and R. Waser, Nanotechnology, 2012, **23**, 145703.
27. S. Long, X. Lian, C. Cagli, X. Cartoixà, R. Rurali, E. Miranda, D. Jiménez, L. Perniola, M. Liu and J. Suñé, Appl. Phys. Lett, 2013, **102**, 183505.
28. X. Lian, E. Miranda, S. Long, L. Perniola, M. Liu and J. Suñé, ULIS, 2013, 161-163.
29. X. Lian, E. Miranda, S. Long, L. Perniola, M. Liu and J. Suñé, Solid-State Electronics, has been accepted,10.1016/j.sse.2014.04.016.
30. E. Miranda, C. Walczyk, C. Wenger, and T. Schroeder, IEEE Electron Device Lett, 2010, **31**, 609.
31. R. Degraeve, Ph. Roussel, L. Goux, D. Wouters, J. Kittl, L. Altimine, M. Jurczak and G. Groseneken, Techn. Dig. of the IEEE Int. Electron Devices Meeting, 2010, 632.
32. E. Miranda, S. Kano, C. Dou, K. Kakushima, J. Suñé, and H. Iwai, Appl. Phys. Lett, 2012,**101**, 012910.
33. J. M. Soler, E. Artacho, J. D. Gale, A. García, J. Junquera, P. Ordejón, and D. Sánchez-Portal, J. Phys.:Condens. Matter, 2002, **14**, 2745.
34. X. Zhao and D. Vanderbilt, Phys. Rev. B, 2002, **65**, 233106.
35. H. J. Monkhorst and J. D. Pack, Phys. Rev. B, 1976, **13**, 5188.
36. S.-G. Park, B. Magyari-Köpe, and Y. Nishi, Phys. Rev. B, 2010, **82**, 115109.
37. X. Cartoixà, R. Rurali, and J. Suñé, Phys. Rev. B, 2012, **86**, 165445.
38. X. Lian, S. Long, C. Cagli, J. Buckley, E. Miranda, M. Liu, J. Suñé, ULIS 2012, 101-104.
39. S. Datta, in Electronic transport in mesoscopic systems, Cambridge University Press, 1997.
40. M. Büttiker, Phys. Rev. B, 1990, **41**, 7906.
41. E. N. Bogachek, A. G. Scherbakov, and U. Landman, Phys. Rev. B, 1997, **56**, 1065.
42. E. Miranda and J. Suñé, Annual Proceedings-Reliability Physics (Symposium), 2001, 367-379.
43. U. Russo, D. Ielmini, C. Cagli, A. L. Lacaita, S. Spiga, C. Wiemer, M. Perego, M. Fanciulli, in IEDM Tech. Dig. 2007, **775**.
44. U. Russo, D. Ielmini, C. Cagli and A.L. Lacaita, IEEE Trans. Electron Devices, 2009, **56**, 193.
45. D. C. Gilmer, G. Bersuker, S. Koveshnikov, M. Jo, A. Kalantarian, B. Butcher, R. Geer, Y. Nishi, P. D. Kirsch and R. Jammy, Proc. of IEEE International Memory Workshop, 2012, 978.